Spectral Ultrasound Characterization of Tissues and Tissue Engineered Constructs

by

Madhu Sudhan Reddy Gudur

A dissertation submitted in partial fulfillment
of the requirements for the degree of
Doctor of Philosophy
(Biomedical Engineering)
in the University of Michigan
2013

Doctoral Committee:

Associate Professor Cheri X. Deng, Chair
Professor J. Brian Fowlkes
Associate Professor Jan P. Stegemann
Assistant Professor Zhen Xu

To my parents and my brother

for their encouragement, love and support

Acknowledgements

I would like to express my gratitude to my advisor, Dr. Cheri X. Deng for her continual and patient guidance that helped me learn, improve and contribute as an effective researcher throughout my Ph.D. program. Her excitement and curiosity towards the research are some of the quintessential qualities that I admire about her and that made my research motivating and productive. Keeping patience, being rationale and practical are the utmost characteristics that I have inculcated during my Ph.D. and for that I am grateful for Dr. Cheri Deng. I would like to thank Dr. Jan P. Stegemann also for his guidance and support in all of the collaboration projects. I am extremely privileged to have him as a mentor.

I would like to thank my dissertation committee members, Dr. Brian Fowlkes and Dr. Zhen Xu, whose insights, ideas and suggestions on my projects during my qualifying exam improved the organization and solidness of my research towards thesis.

I would like to express my deepest appreciation to Dr.Stegemann's Lab members: Dr. Ram Rao, Alexis Peterson and David Caldwell for all the support, advice and continuous dedication in all of the collaboration projects towards my thesis.

Special thanks go to all of my labmates Ziqi Wu, Yi-sing Hsiao, Dr. Di Chen and Yu Fang for their friendship with which the entire Ph.D. life has become more fun. I would cherish these four years for my entire life. I greatly appreciate the group's willingness to help out each other, in projects and in personal life. Furthermore, I would also like to acknowledge with much

appreciation the crucial role of Dr. Ronald Kumon and Dr. Yun Zhou for their immense efforts, support and guidance in my projects.

I would like to thank some of my close friends Dr. Jeevan Maddala, AVVS Praneeth Kumar, Sriya Das, Manjunath and Om Koted for their dear friendship and fun times throughout the years.

I cannot thank enough for all the handwork that my parents, Daan Reddy Gudur & Lakshmi Gudur, put in to give me and my brother the best education that they can. Being illiterate, they knew the importance of education for social and professional life. Even with that, they never pressurized me instead they showed passion and interest in my education which is one of the key factor for all the success I had. I am grateful to be their son. My brother, Balawanth Reddy Gudur, has always been there to support me, even during the difficult times. He always considered my success and failures as his own, the kind of interest that makes me glad to be his brother. It was always lovely and refreshing to skype with my 2 year old fun niece, Avanthika Reddy.

Table of Contents

List of Figures

List of Tables

Abstract

Even though ultrasound imaging is widely used in clinical diagnosis and image-guided interventions, the field is far behind other areas of clinical quantitative image analysis, such as MRI, CT and X-ray mammography. In this thesis, non-destructive and non-invasive ultrasound characterization techniques were developed to study the tissue micro-structural details using high frequency spectral ultrasound imaging (SUSI). The techniques were explored in *in-vitro* conditions of acellular and cellular tissue engineered constructs and then on *ex-vivo* tissues for their characterization. SUSI was used to assess the amount of hydroxyl-apatite (HA) mineral, differentiate HA mineral types and study their distribution in acellular tissue engineered constructs. The process of mineral deposition from surrounding mineralizing media onto simple collagen constructs was also studied and characterized with SUSI. 3D morphological changes of the constructs with MC3t3 cells was monitored and characterized for the developmental changes such as net cell proliferation/apoptosis and cell differentiation process through mineral production by the early osteoblastic MC3t3-cell constructs *in-situ*. A novel method was introduced using SUSI to estimate the amount of mineral secreted by the differentiated osteoblast cells in a non-destructive method. Then, SUSI was investigated in *ex-vivo* cardiac tissues to monitor and characterize the cellular changes during high-intensity focused ultrasound ablation with high-frame-rate and high-resolution ultrasound imaging. The mechanistic hypotheses behind the improvement in lesion detection were investigated and best identification methods to assess lesion formation and transient gas body activities were proposed to provide a method for

visualizing spatiotemporal evolution of lesion and gas–body activity and for predicting macroscopic cavity formation upon its implementation as a real-time monitoring technique with feedback control system for HIFU treatment of atrial fibrillation to improve the ablation process. Even though the results from the developed techniques show great promise in *in-vitro* and *ex-vivo* settings, additional work needs to be carried out to demonstrate the applicability of the techniques in *in-vivo*.

CHAPTER 1

Introduction

Cells, extracellular matrix and growth factors are combined to generate living tissues for plausible implants in tissue engineering. Usually, these tissue constructs will be developed in lab before administering into the target site, for example at bone fracture sites for faster healing in orthopedic applications. To ensure their quality throughout the development time, quantitative methods needs to be used to assess the construct state. Traditional methods use histological or biochemical assays which are destructive, time consuming, expensive, most of the times can analyze only 2D sections and cannot monitor the tissue development due to its destructive nature. So, there is a growing demand for non-destructive assessment methods, which can characterize physical and microstructural properties quantitatively with the ability to perform temporal monitoring, particularly to translate tissue engineering methods into clinic.

Some of the non-destructive methods in practice include Magnetic Resonance Imaging (MRI), Computed Tomography (CT), microscopic imaging and ultrasound. Each of these methods have their advantages and disadvantages over other methods. MRI is non-toxic, can assess bone mineral density but has low resolution and takes relatively long time for imaging. CT has good resolution, can assess bone mineral density but may be toxic and also takes long time for imging. Microscopy has high resolution but requires sophisticated procedures to acquire data and process them. With microscopy imaging, mainly cell nuclei can be monitored and it is hard to implement the technique in *in-vivo*. Ultrasound is fast (can be implemented in real-time), cheap and non-toxic. Its resolution depends on the imaging frequency and hence can be adapted as per the desired application. With high resolution at high imaging frequencies, ultrasound can characterize physical and microstructural properties of the tissue. This assessment technique will be helpful in non-destructive characterization and monitoring of the tissue samples in lab and for *in-vivo* applications in small animals. Due to the shallow imaging regions at higher frequencies, this technique might be limited to fewer specific applications in humans.

This dissertation addresses practical, non-destructive and non-invasive characterization techniques to study the tissue structure using high frequency spectral ultrasound imaging. The research is primarily categorized into two sections: developing practical technique to estimate tissue scatterer properties and implementing the techniques to identify specific cellular changes. Even though the results from the developed techniques show great promise in *in-vitro* settings, additional works needs to be carried out to demonstrate the applicability of the techniques in *in-vivo*.

1.1 Characterization Techniques

Even though ultrasound imaging is so widely used in clinical diagnosis and image-guided interventions, the field is far behind other areas of clinical quantitative image analysis, such as MRI, CT and X-ray mammography. Successful ultrasound characterization methods should utilize geometric, temporal, intensity, and imaging physics principles. The choice of which constraints to use is in part application specific, but many constraints hold for generic ultrasound characterization methods.

Characterization of tissues for its structure can be made with B-mode “image” data or radiofrequency (RF) data. With access to the raw ultrasound backscattered information in RF data and availability of high sampling rate of the ultrasound signals, characterization techniques with RF data are usually more accurate, reliable and robust compared to B-mode image data. Characterization with B-mode images is usually referred as image segmentation techniques whereas with RF data as quantitative ultrasound (QUS) characterization techniques.

Most basic and fastest QUS characterization techniques are usually in the time/space domain of the ultrasound signal. Simplest technique being thresholding the envelope of the RF backscattered signal in applications where high contrast in the tissue segment of interest compared to the other regions is observed. Since most of the applications doesn’t show high contrast, more detailed characterization techniques were used. Measurements of ultrasonic attenuation have been helpful in identifying diffuse liver disease and benign conditions in the breast [1, 2]. Attenuation estimation methods can be classified as either time or frequency-domain approaches [3-5]. Video or B-mode signal analysis methods were developed by Knipp *et al.* [6] to estimate attenuation directly from B-mode images.

Acoustic radiation force impulse (ARFI) imaging is a radiation force-based imaging method that provides information about the local mechanical properties of tissue [7-9]. ARFI imaging uses short-duration acoustic radiation forces to generate localized displacements in tissue, and these displacements are tracked using ultrasonic correlation-based methods. The tissue response to these forces can be monitored both spatially and temporally. Displacement magnitude is inversely proportional to local tissue stiffness. In this method, a single transducer on a diagnostic ultrasound (US) system can be used to both apply localized radiation forces within tissue for short time periods and to track the resulting tissue displacements. The use of a single transducer guarantees both alignment and ease of clinical implementation, as well as facilitating real-time implementation. ARFI imaging has many potential clinical applications, including detecting and characterizing a wide variety of soft tissue lesions, and identifying and characterizing atherosclerosis, plaque and thromboses.

Backscattered ultrasound signals can be modeled as the sum of the contributions from individual scatterers within the range of the pulse echo (the resolution cell). Thus, the statistical distribution of the backscattered ultrasound signal is related to the number of scatterers per resolution cell and their arrangement within the resolution cell. Analysis of this statistical distribution may be used for tissue characterization. Rayleigh, Rician, K, and Nakagami distributions all have been used for tissue characterization [10-12]. For example, Shankar *et al.* [13, 14] demonstrated the usefulness of the *K* and Nakagami distributions for classifying benign and malignant breast tumors. The statistical distribution of the backscattered signal from myocardial tissue also has been characterized by several investigators [15, 16]. Clifford *et al.* [15] tested five statistical models (K, Rician, Rayleigh, Nakagami, and lognormal distributions) for description of normal myocardial tissue.

Some ultrasonic tissue characterization techniques generally consider frequency dependent information of backscatter echoes to quantify tissue structural properties, such as the size, acoustic impedance, number density of scattering particles, etc. This approach has been successfully used for the characterization of the eye [17, 18], liver [19], kidney [20], prostate [21], breast tissues [22] and also to monitor cell apoptosis in order to evaluate the efficacy of cancer therapies [23].

1.2 Spectral Ultrasound Imaging

Conventional B-mode ultrasound imaging is based purely on gray scale values and is able to provide spatial and temporal information about sample morphology. However it provides little direct information about sample composition. A key drawback of purely gray scale analysis is that the image signal is dependent on a variety of factors including ultrasound transducer response and image post-processing. The results are therefore operator- and system-dependent, and it is difficult to compare data taken on different imaging systems or at different times in an objective and meaningful fashion. In contrast, spectral ultrasound imaging (SUSI) utilizes unprocessed, raw backscattered radiofrequency (RF) signals.

Studies carried out mostly over the last few years used high-frequency (10 to 60 MHz) ultrasound to investigate backscattering properties of cell aggregates, which were used as simplified models of tumors [23, 24]. In this regime, wavelengths (25 to 150 μ m) approach the size (10 to 20 μ m) of the cells or nuclei and exhibit much more sensitivity to cell structure and changes in cell structure during cell death compared with the lower interrogating frequency range (<10 MHz) available with conventional ultrasound imaging systems [23]. This observation suggests that the high-frequency ultrasound backscattering technique can be used to detect cell apoptosis and also to monitor efficacy of cancer treatments [25].

Kolios *et al.* [24] used an ultrasound spectral analysis method to analyze measured ultrasound signals from cell ensembles treated with chemotherapeutics and also from aggregates of healthy cells. They found that ultrasound backscatter intensity and spectral slope increased because of treatment and that was interpreted as a consequence of the decrease in effective scatterer size. Similarly, Vlad *et al.* [23] experimentally investigated how backscattering properties for several cell lines vary with time after radiotherapy, and consequently examined the potential of this technique to differentiate various types of cell death. Tunis *et al.* [26] studied the envelope statistics of ultrasound backscatter signals from cisplatin-treated aggregated acute myeloid leukemia (AML) cells and evaluated the applicability of various statistical distribution functions to model the envelope histograms. They reported that shape parameters of the generalized gamma distribution function were sensitive to the structural changes within cells induced by the drug. Oelze *et al*. [22] also used high-frequency ultrasound to differentiate and characterize rat mammary fibroadenomas and 4T1 mouse carcinomas. They generated quantitative ultrasound (QUS) images based on the estimated scatterer properties (scatterer diameter, acoustic concentration). These properties were obtained by analyzing backscatter signals in the spectral domain and by employing a Gaussian form factor model [20]. They showed that QUS images are capable of distinguishing two types of tumors. In another investigation [10], the same group examined carcinoma and sarcoma in mouse models using QUS. It was observed that the estimated parameters extracted from the frequency band 10 to 25 MHz cannot distinguish between the two kinds of tumors, but those of 16 to 25 MHz can clearly show some differences.

Spectral parameters have also proven to be effective for identifying changes in tissue state for prostate, breast and other cancer tissues [22, 27] as well as intravascular plaque [28-30]. Thus, SUSI can be used as an effective tool to characterize several tissues for their composition and structure including assessment of tissue engineered constructs.

1.3 Ultrasound in Tissue Engineering

Ultrasound imaging has shown promise for rapid and nondestructive imaging in tissue engineering. In particular, ultrasound has been used to characterize the evolution of tissue components and corresponding changes in tissue properties in a variety of systems. For example, attenuation of gray scale (B-mode) ultrasound signals over time has been shown to correlate with matrix deposition and differentiation of adipose stem cells on synthetic scaffolds [31]. Similarly, gray scale signals have been used to assess collagen production by myofibroblasts in 3D fibrin matrices over time [32]. Kreitz et al. tracked collagen deposition by myofibroblasts in fibrin tissue constructs over an 18 day culture period.[33] Their quantitative analysis of observed gray scale values were correlated to ECM deposition as measured by hydroxyproline content. Acoustic parameters have also been correlated to the mechanical properties and cartilage matrix evolution by chondrocytes in polyethylene glycol hydrogels [34] and have been used characterize the mechanical properties of agarose hydrogels as they develop over time [35]. Ultrasound has also been used as a non-destructive method to quantify the actual number of cells in BMSC/β-TCP composites by grayscale equivalent parameter [36]. Not many studies have been done in assessing tissue engineered construct for cell size, concentration and construct composition. SUSI may therefore have utility in more fully characterizing the composition of engineered tissues.

1.4 Atrial Fibrillation

Atrial fibrillation is the most common cardiac arrhythmia and its current clinical treatment procedures can use real-time monitoring techniques to improve the efficiency of the treatment. One of the able treatments is high intensity focused ultrasound (HIFU) [37] and its monitoring during the treatment is not well established. A section of the current study aims to establish methods to monitor HIFU ablation process in real-time in *ex-vivo* cardiac tissues to determine the lesion extent and gas-body activities. The formation and extent of HIFU-induced tissue necrosis, or thermal lesion, is determined by the spatiotemporal distribution of temperature-increase induced by HIFU exposure [38, 39].To achieve better control of the ablation process, robust and effective imaging methods are needed for real-time monitoring of tissue changes such as lesion formation during HIFU application. Magnetic resonance imaging (MRI) has been valuable in guiding and monitoring HIFU ablations [40-42] in real-time with spatial and temporal control on temperature rise in the tissue induced by HIFU. While magnetic resonance imaging (MRI) [40] and x-ray computed tomography (CT) [43] have been used as effective image guidance during ablation, monitoring with diagnostic ultrasound imaging has the advantage of relatively lower cost, higher portability, and high spatiotemporal resolution.

A variety of ultrasound imaging techniques beyond conventional grayscale B-mode imaging has been developed to detect tissue changes. For example, ultrasound tracking of echo shifts [44-46] or changes in ultrasound backscatter [47, 48] have been used to monitor temperature changes during HIFU ablation. Ultrasound elastography has been used to evaluate tissue necrosis [8, 9, 49, 50] as thermal lesions exhibit increased stiffness, but lesion characterization via elastographic imaging is subject to degradation in the presence of gas bodies [51].

HIFU ablation induced changes in attenuation [52-54] and ultrasound backscatter [53-55] were used to detect changes in tissue state. Integrated backscatter changes to monitor HIFU lesion formation have been studied in *ex vivo* bovine liver at an imaging frequency of 7.5 MHz [53, 54]. Tadpole-shaped lesions showed an increase in differential attenuation of up to 3.5 dB/MHz/cm and increase in accumulated differential integrated backscatter (IBS) of up to 25–30 dB, although more precise definition of the lesion was obtained with the differential IBS image.

Echo decorrelation has been proposed as a means to identify lesion formation in radiofrequency (RF) ablation, with the potential benefits of reduced sensitivity to acoustic shadowing and tissue motion as compared to other methods [56]. Mapping and characterization of RF ablated lesions in *ex vivo* liver tissue with temporal maximum decorrelation showed good performance when compared to temporal maximum IBS using backscattered RF data from B-mode ultrasound imaging [56, 57].

Spectral parameters of the backscattered RF ultrasound data, which are related to tissue properties like effective acoustic scatterer size and concentration [58], have also been shown to change as a result of HIFU exposure. Lesions induced by HIFU in *ex vivo* chicken breast and rabbit liver showed increased midband fit of 6 to 8 dB compared to surrounding non-ablated tissue [58, 59]. These increases are likely due to the increased backscatter from gas bodies induced by HIFU exposure in the focal region and changes in effective scatterer size due to coagulative necrosis. Spectral parameters have also been computed to characterize lesions induced by RF ablation in *ex vivo* bovine liver [60].

Although a variety of methods have been proposed to improve ultrasound imaging of HIFU ablation and lesion formation, ultrasound imaging has not yet been established as a robust and consistent technique.

1.5 Organization of Thesis

A detailed theory and analysis of spectral ultrasound with methods to estimate scatterer size and concentration are presented in Chapter 2. The theory was verified with experiments on polybead phantoms to validate the polybead diameter and concentration estimation using spectral ultrasound imaging (SUSI).

SUSI is then used to assess the amount of mineral content in acellular tissue engineered constructs in Chapter 3. Spectral parameters in differentiating and characterizing different mineral types seeded in collagen construct were investigated. The process of mineral deposition from surrounding fluid medium onto simple collagen constructs was studied and the amount of mineral deposition was characterized with SUSI.

Chapter 4 focuses on providing high resolution ultrasound as an imaging modality in the field of tissue engineering to monitor the 3D morphological changes of the constructs online and to characterize the development changes which include net cell proliferation/apoptosis and cell differentiation process through mineral production estimation of the early osteoblastic MC3t3- cell constructs *in-situ* in a non-destructive method.

The ability of high-frame-rate and high-resolution imaging to monitor lesion formation and gas-body activity during high-intensity focused ultrasound (HIFU) was examined in Chapter 5. The mechanistic hypotheses behind the improvement in lesion detection were investigated and a best identification method to assess lesion formation was proposed. Transient gas-body activity was identified and tracked. These assessments provide a method for visualizing spatiotemporal evolution of lesion and gas–body activity and for predicting macroscopic cavity formation and can be implemented as real-time monitoring with feedback control system for HIFU treatment of atrial fibrillation to improve the ablation process.

1.6 References

[1] G. Berger, P. Laugier, J. C. Thalabard, and J. Perrin, "Global breast attenuation:control group and benign breast diseases," *Ultrason Imaging*, vol. 12, pp. 47-57, Jan 1990.

[2] B. J. Oosterveld, J. M. Thijssen, P. C. Hartman, R. L. Romijn, and G. J. Rosenbusch, "Ultrasound attenuation and texture analysis of diffuse liver disease: methods and preliminary results," *Phys Med Biol,* vol. 36, pp. 1039-64, Aug 1991.

[3] E. Walach, A. Shmulewitz, Y. Itzchak, and Z. Heyman, "Local tissue attenuation images based on pulsed-echo ultrasound scans," *IEEE Trans Biomed Eng,* vol. 36, pp. 211-21, Feb 1989.

[4] M. Fink, F. Hottier, and J. F. Cardoso, "Ultrasonic signal processing for in vivo attenuation measurement: short time Fourier analysis," *Ultrason Imaging,* vol. 5, pp. 117-35, Apr 1983.

[5] H. Kim, J. A. Zagzebski, and T. Varghese, "Estimation of ultrasound attenuation from broadband echo-signals using bandpass filtering," *IEEE Trans Ultrason Ferroelectr Freq Control,* vol. 55, pp. 1153-9, May 2008.

[6] B. S. Knipp, J. A. Zagzebski, T. A. Wilson, F. Dong, and E. L. Madsen, "Attenuation and backscatter estimation using video signal analysis applied to B-mode images," *Ultrason Imaging,* vol. 19, pp. 221-33, Jul 1997.

[7] K. R. Nightingale, M. L. Palmeri, R. W. Nightingale, and G. E. Trahey, "On the feasibility of remote palpation using acoustic radiation force," *J Acoust Soc Am,* vol. 110, pp. 625-34, Jul 2001.

[8] B. J. Fahey, K. R. Nightingale, S. A. McAleavey, M. L. Palmeri, P. D. Wolf, and G. E. Trahey, "Acoustic radiation force impulse imaging of myocardial radiofrequency ablation: Initial in vivo results," *IEEE Trans. Ultrason. Ferroelectr. Freq. Control,* vol. 52, pp. 631-641, Apr 2005.

[9] S. A. Eyerly, S. J. Hsu, S. H. Agashe, G. E. Trahey, Y. Li, and P. D. Wolf, "An in vitro assessment of acoustic radiation force impulse imaging for visualizing cardiac radiofrequency ablation lesions," *J. Cardiovasc. Electrophysiol.,* vol. 21, pp. 557-563, May 2010.

[10] P. M. Shankar, J. M. Reid, H. Ortega, C. W. Piccoli, and B. B. Goldberg, "Use of non-Rayleigh statistics for the identification of tumors in ultrasonic B-scans of the breast," *IEEE Trans Med Imaging,* vol. 12, pp. 687-92, 1993.

[11] L. Weng, J. M. Reid, P. M. Shankar, and K. Soetanto, "Ultrasound speckle analysis based on the K distribution," *J Acoust Soc Am,* vol. 89, pp. 2992-5, Jun 1991.

[12] R. F. Wagner, M. F. Insana, and D. G. Brown, "Statistical properties of radio-frequency and envelope-detected signals with applications to medical ultrasound," *J Opt Soc Am A,* vol. 4, pp. 910-22, May 1987.

[13] P. M. Shankar, V. A. Dumane, J. M. Reid, V. Genis, F. Forsberg, C. W. Piccoli, *et al.*, "Use of the K-distribution for classification of breast masses," *Ultrasound Med Biol,* vol. 26, pp. 1503-10, Nov 2000.

[14] P. M. Shankar, V. A. Dumane, J. M. Reid, V. Genis, F. Forsberg, C. W. Piccoli, *et al.*, "Classification of ultrasonic B-mode images of breast masses using Nakagami distribution," *IEEE Trans Ultrason Ferroelectr Freq Control,* vol. 48, pp. 569-80, Mar 2001.

[15] L. Clifford, P. Fitzgerald, and D. James, "Non-Rayleigh 1st-Order Statistics of Ultrasonic Backscatter from Normal Myocardium," *Ultrasound in Medicine and Biology,* vol. 19, pp. 487-495, 1993.

[16] R. F. Wagner, S. W. Smith, J. M. Sandrik, and H. Lopez, "Statistics of Speckle in Ultrasound B-Scans," *Ieee Transactions on Sonics and Ultrasonics,* vol. 30, pp. 156-163, 1983.

[17] F. L. Lizzi, M. Greenebaum, E. J. Feleppa, M. Elbaum, and D. J. Coleman, "Theoretical Framework for Spectrum Analysis in Ultrasonic Tissue Characterization," *Journal of the Acoustical Society of America,* vol. 73, pp. 1366-1373, 1983.

[18] E. J. Feleppa, F. L. Lizzi, D. J. Coleman, and M. M. Yaremko, "Diagnostic Spectrum Analysis in Ophthalmology - a Physical Perspective," *Ultrasound in Medicine and Biology,* vol. 12, pp. 623-631, Aug 1986.

[19] F. L. Lizzi, M. Ostromogilsky, E. J. Feleppa, M. C. Rorke, and M. M. Yaremko, "Relationship of ultrasonic spectral parameters to features of tissue microstructure," *IEEE Trans. Ultrason. Ferroelectr. Freq. Control,* vol. 34, pp. 319-329, May 1987.

[20] M. F. Insana, R. F. Wagner, D. G. Brown, and T. J. Hall, "Describing Small-Scale Structure in Random-Media Using Pulse-Echo Ultrasound," *Journal of the Acoustical Society of America,* vol. 87, pp. 179-192, Jan 1990.

[21] E. J. Feleppa, T. Liu, A. Kalisz, M. C. Shao, N. Fleshner, V. Reuter, *et al.*, "Ultrasonic spectral-parameter imaging of the prostate," *International Journal of Imaging Systems and Technology,* vol. 8, pp. 11-25, 1997.

[22] M. L. Oelze, W. D. O'Brien, J. P. Blue, and J. F. Zachary, "Differentiation and characterization of rat mammary fibroadenomas and 4T1 mouse carcinomas using quantitative ultrasound imaging," *Ieee Transactions on Medical Imaging,* vol. 23, pp. 764-771, Jun 2004.

[23] R. M. Vlad, N. M. Alajez, A. Giles, M. C. Kolios, and G. J. Czarnota, "Quantitative Ultrasound Characterization of Cancer Radiotherapy Effects in Vitro," *International Journal of Radiation Oncology Biology Physics,* vol. 72, pp. 1236-1243, Nov 15 2008.

[24] M. C. Kolios, G. J. Czarnota, M. Lee, J. W. Hunt, and M. D. Sherar, "Ultrasonic spectral parameter characterization of apoptosis," *Ultrasound in Medicine and Biology,* vol. 28, pp. 589-597, May 2002.

[25] G. J. Czarnota, M. C. Kolios, J. Abraham, M. Portnoy, F. P. Ottensmeyer, J. W. Hunt, *et al.*, "Ultrasound imaging of apoptosis: high-resolution non-invasive monitoring of programmed cell death in vitro, in situ and in vivo," *British Journal of Cancer,* vol. 81, pp. 520-527, Oct 1999.

[26] A. S. Tunis, G. J. Czarnota, A. Giles, M. D. Sherar, J. W. Hunt, and M. C. Kolios, "Monitoring structural changes in cells with high-frequency ultrasound signal statistics," *Ultrasound in Medicine and Biology,* vol. 31, pp. 1041-1049, Aug 2005.

[27] S. Crouzet, F. J. Murat, G. Pasticier, P. Cassier, J. Y. Chapelon, and A. Gelet, "High intensity focused ultrasound (HIFU) for prostate cancer: Current clinical status, outcomes and future perspectives," *Int. J. of Hyperthermia,* vol. 26, pp. 796-803, 2010.

[28] A. Nair, B. D. Kuban, E. M. Tuzcu, P. Schoenhagen, S. E. Nissen, and D. G. Vince, "Coronary plaque classification with intravascular ultrasound radiofrequency data analysis," *Circulation,* vol. 106, pp. 2200-2206, Oct 22 2002.

[29] K. Nasu, E. Tsuchikane, O. Katoh, D. G. Vince, R. Virmani, J. F. Surmely, *et al.*, "Accuracy of in vivo coronary plaque morphology assessment - A validation study of in vivo virtual histology compared with in vitro histopathology," *Journal of the American College of Cardiology,* vol. 47, pp. 2405-2412, Jun 20 2006.

[30] J. Qian, A. Maehara, G. S. Mintz, M. P. Margolis, A. Lerman, J. Rogers, *et al.*, "Impact of Gender and Age on In Vivo Virtual Histology-Intravascular Ultrasound Imaging Plaque Characterization (from the global Virtual Histology Intravascular Ultrasound [VH-IVUS] Registry)," *American Journal of Cardiology,* vol. 103, pp. 1210-1214, May 1 2009.

[31] B. Z. Fite, M. Decaris, Y. H. Sun, Y. Sun, A. Lam, C. K. L. Ho, *et al.*, "Noninvasive multimodal evaluation of bioengineered cartilage constructs combining time-resolved fluorescence and ultrasound imaging," *Tissue Engineering Part C-Methods,* vol. 17, pp. 495-504, Apr 2011.

[32] S. Kreitz, G. Dohmen, S. Hasken, T. Schmitz-Rode, P. Mela, and S. Jockenhoevel, "Nondestructive method to evaluate the collagen content of fibrin-based tissue engineered structures via ultrasound," *Tissue Engineering Part C-Methods,* vol. 17, pp. 1021-1026, Oct 2011.

[33] S. Kreitz, G. Dohmen, S. Hasken, T. Schmitz-Rode, P. Mela, and S. Jockenhoevel, "Non-Destructive Method to Evaluate the Collagen Content of Fibrin-Based Tissue Engineered Structures via Ultrasound," *Tissue Engineering Part C: Methods,* p. 110610223126034, 2011.

[34] M. A. Rice, K. R. Waters, and K. S. Anseth, "Ultrasound monitoring of cartilaginous matrix evolution in degradable PEG hydrogels," *Acta Biomaterialia,* vol. 5, pp. 152-161, Jan 2009.

[35] J. M. Walker, A. M. Myers, M. D. Schluchter, V. M. Goldberg, A. I. Caplan, J. A. Berilla, *et al.*, "Nondestructive evaluation of hydrogel mechanical properties using ultrasound," *Annals of Biomedical Engineering,* vol. 39, pp. 2521-2530, Oct 2011.

[36] K. Oe, M. Miwa, K. Nagamune, Y. Sakai, S. Y. Lee, T. Niikura, *et al.*, "Nondestructive evaluation of cell numbers in bone marrow stromal cell/beta-tricalcium phosphate composites using ultrasound," *Tissue Engineering Part C-Methods,* vol. 16, pp. 347-353, Jun 2010.

[37] M. A. Groh, O. A. Binns, H. G. Burton, 3rd, S. W. Ely, and A. M. Johnson, "Ultrasonic cardiac ablation for atrial fibrillation during concomitant cardiac surgery: long-term clinical outcomes," *Ann. Thoracic Surg.,* vol. 84, pp. 1978-83, Dec 2007.

[38] C. Damianou and K. Hynynen, "The effect of various physical parameters on the size and shape of necrosed tissue volume during ultrasound surgery," *J. Acoust. Soc. Am.,* vol. 95, pp. 1641-9, Mar 1994.

[39] S. J. Graham, L. Chen, M. Leitch, R. D. Peters, M. J. Bronskill, F. S. Foster, *et al.*, "Quantifying tissue damage due to focused ultrasound heating observed by MRI," *Magn. Reson. Med.,* vol. 41, pp. 321-328, Feb 1999.

[40] K. Hynynen, A. Darkazanli, E. Unger, and J. F. Schenck, "MRI-guided noninvasive ultrasound surgery," *Med. Phys.,* vol. 20, pp. 107-115, Jan-Feb 1993.

[41] A. B. Holbrook, J. M. Santos, E. Kaye, V. Rieke, and K. B. Pauly, "Real-Time MR Thermometry for Monitoring HIFU Ablations of the Liver," *Magnetic Resonance in Medicine,* vol. 63, pp. 365-373, Feb 2010.

[42] C. Mougenot, B. Quesson, B. D. de Senneville, P. L. de Oliveira, S. Sprinkhuizen, J. Palussiere, *et al.*, "Three-Dimensional Spatial and Temporal Temperature Control With MR Thermometry-Guided Focused Ultrasound (MRgHIFU)," *Magnetic Resonance in Medicine,* vol. 61, pp. 603-614, Mar 2009.

[43] R. Yang, K. K. Kopecky, F. J. Rescorla, C. A. Galliani, E. X. Wu, and J. L. Grosfeld, "Sonographic and computed tomography characteristics of liver ablation lesions induced by high-intensity focussed ultrasound," *Investigative Radiol.,* vol. 28, pp. 796-801, Sep 1993.

[44] D. Liu and E. S. Ebbini, "Real-time 2-D temperature imaging using ultrasound," *IEEE Trans. Biomed. Eng.,* vol. 57, pp. 12-6, Jan 2010.

[45] N. R. Miller, J. C. Bamber, and P. M. Meaney, "Fundamental limitations of noninvasive temperature imaging by means of ultrasound echo strain estimation," *Ultrasound in Medicine and Biology,* vol. 28, pp. 1319-1333, Oct 2002.

[46] C. Simon, P. Vanbaren, and E. S. Ebbini, "Two-dimensional temperature estimation using diagnostic ultrasound," *IEEE Trans. Ultrason. Ferroelectr. Freq. Control,* vol. 45, pp. 1088-99, 1998.

[47] R. M. Arthur, D. Basu, Y. Z. Guo, J. W. Trobaugh, and E. G. Moros, "3-D in vitro estimation of temperature using the change in backscattered ultrasonic energy," *IEEE Trans. Ultrason. Ferroelectr. Freq. Control,* vol. 57, pp. 1724-1733, Aug 2010.

[48] W. L. Straube and R. M. Arthur, "Theoretical estimation of the temperature-dependence of backscattered ultrasonic power for noninvasive thermometry," *Ultrasound Med. Biol.,* vol. 20, pp. 915-922, 1994.

[49] F. L. Lizzi, R. Muratore, C. X. Deng, J. A. Ketterling, S. K. Alam, S. Mikaelian*, et al.*, "Radiation-force technique to monitor lesions during ultrasonic therapy," *Ultrasound Med. Biol.,* vol. 29, pp. 1593-605, Nov 2003.

[50] C. Maleke and E. E. Konofagou, "Harmonic motion imaging for focused ultrasound (HMIFU): a fully integrated technique for sonication and monitoring of thermal ablation in tissues," *Phys. Med. Biol.,* vol. 53, pp. 1773-1793, Mar 2008.

[51] T. Varghese, U. Techavipoo, J. A. Zagzebski, and F. T. Lee, "Impact of gas bubbles generated during interstitial ablation on elastographic depiction of in vitro thermal lesions," *J. Ultrasound Med.,* vol. 23, pp. 535-544, Apr 2004.

[52] M. Ribault, J. Y. Chapelon, D. Cathignol, and A. Gelet, "Differential attenuation imaging for the characterization of high intensity focused ultrasound lesions," *Ultrason. Imaging,* vol. 20, pp. 160-177, Jul 1998.

[53] H. Zhong, M. X. Wan, Y. F. Jiang, and S. P. Wang, "Monitoring imaging of lesions induced by high intensity focused ultrasound based on differential ultrasonic attenuation and integrated backscatter estimation," *Ultrasound Med. Biol.*, vol. 33, pp. 82-94, Jan 2007.

[54] S. Y. Zhang, M. X. Wan, H. Zhong, C. Xu, Z. H. Liao, H. Q. Liu, *et al.*, "Dynamic changes of integrated backscatter, attenuation coefficient and bubble activities during high-intensity focused ultrasound (HIFU) treatment," *Ultrasound Med. Biol.*, vol. 35, pp. 1828-1844, 2009.

[55] A. Anand and P. J. Kaczkowski, "Monitoring formation of high intensity focused ultrasound (HIFU) induced lesions using backscattered ultrasound," *Acoust. Res. Lett. Online*, vol. 5, pp. 88-94, 2004.

[56] T. D. Mast, D. P. Pucke, S. E. Subramanian, W. J. Bowus, S. M. Rudich, and J. F. Buell, "Ultrasound monitoring of in vitro radio frequency ablation by echo decorrelation imaging," *J. Ultrasound Med.*, vol. 27, pp. 1685-1697, Dec 2008.

[57] T. D. Mast and S. Subramanian, "Analytic and numerical modeling of ultrasonic B-scan and echo decorrelation imaging," *Proc. Meetings Acoust.*, vol. 9, p. 020003, 2010.

[58] F. L. Lizzi, M. Astor, T. Liu, C. Deng, D. J. Coleman, and R. H. Silverman, "Ultrasonic spectrum analysis for tissue assays and therapy evaluation," *Int. J. Imag. Sys. Tech.*, vol. 8, pp. 3-10, 1997.

[59] R. H. Silverman, R. Muratore, J. A. Ketterling, J. Mamou, D. J. Coleman, and E. J. Feleppa, "Improved visualization of high-intensity focused ultrasound lesions," *Ultrasound Med. Biol.*, vol. 32, pp. 1743-1751, Nov 2006.

[60] S. Siebers, M. Schwabe, U. Scheipers, C. Welp, J. Werner, and H. Ermert, "Evaluation of ultrasonic texture and spectral parameters for coagulated tissue characterization," in *2004 IEEE Int. Ultrason. Symp. Proc.*, 2004, pp. 1804-1807.

CHAPTER 2

Spectral Ultrasound Imaging

High-frequency ultrasound research is attracting considerable interest because its short wavelengths (e.g., 50 µm at 30 MHz) and small focal-zone beam diameters provide fine-resolution images. Quantitative ultrasound (QUS) imaging is being investigated by several research groups and many tissue parameters have been estimated. This chapter focuses on one such QUS method that incorporate spectrum analysis of high frequency ultrasound, radio-frequency (RF) echo signals.

2.1 Introduction

Spectral analysis of ultrasound RF signals is derived from the theoretical framework of ultrasound scattering established by Lizzi et al. [1] for biologic tissues and subsequently expanded by him and others (Oelze et al. [2]; Insana et al. [3]; Mamou et al. [4]; Oelze and Zachary [5]). Frequency-dependent information derived from RF backscattered signals [2, 3, 6] was used to quantitatively assess tissue microstructural properties and relate them to histologic properties. Some fundamental high-frequency QUS studies already have been conducted on microspheres and suspended cells [7] and cells in pellets to try to quantify apoptosis [8]. Microspheres and single-cell experiments showed agreement between experimentally- and theoretically-derived backscatter coefficients. In particular, backscatter reflection coefficient resonances predicted by theory were observed experimentally. The results of the apoptosis study also suggested that spectral slope and mid-band fit changed as a function of time in cells treated with an apoptosis-inducing drug.

Our group successfully used spectrum-analysis methods at 6 MHz to show distinct differences between normal and diseased pancreas and lymph nodes. More recently, interest has grown in applying QUS methods using high frequency ultrasound because higher frequencies can evaluate the tissue with finer resolution than lower frequencies. An empirical criterion states that QUS methods are most sensitive to structures for which $kD \approx 2$ [3], where k is the wave number and D is a typical size or dimension of the scattering structures. For example, operating at 55 MHz, i.e., $k = 0.23\ \mu m^{-1}$, leads to $D = 8.7\ \mu m$ in tissue. Hence, higher frequencies allow correlating QUS estimates with tissue microstructure on a finer scale [4, 5, 9, 10]. Therefore, our hypothesis is that QUS estimates at 55 MHz ultrasound imaging may resolve the tissue structure to finer details and may let study tissue changes via HIFU ablation or tissue development process in a great detail.

2.2 Methods

2.2.1 Phantom Preparation

Agar phantoms with Polybead® microspheres (Polysciences, Inc.) of different bead diameters at various concentrations were used in this study. Polybeads were added to the 2% agar solution at 45^0 C and thoroughly mixed to disperse the polybeads uniformly throughout the phantom. Four polybead diameters, 6, 10, 16 and 25 µm that are of interest were chosen. For each polybead size, phantoms with four different concentrations of polybeads were made. Each phantom was approximately 2000 mm^3 in size.

2.2.2 Ultrasound Imaging and Data Acquisition

Figure 2.1 shows a schematic diagram of the imaging setup that includes a 90 mm diameter Petri dish filled with distilled water at room temperature. Phantoms were placed on top of an agar gel pad, which reduces the reflection from the bottom of the dish. Ultrasound imaging was performed with a Vevo 770 (VisualSonics Inc., Toronto, Canada) using an RMV 708 imaging probe with a nominal 55 MHz center frequency, 20-75 MHz bandwidth (−6 dB), 4.5 mm focal distance, and 1.5 mm depth of focus (−6 dB). 3D backscattered RF data from the phantom were collected at either 100% or 50% scanner power and 420 MS/s by performing multiple B-mode scans using an automatic 3D translational controller. The interval between adjacent A-lines and B-mode scans were 31 μm and 64 μm, respectively. After each RF acquisition of a construct, a reference RF acquisition of the setup without the construct was collected, for phantom attenuation estimation.

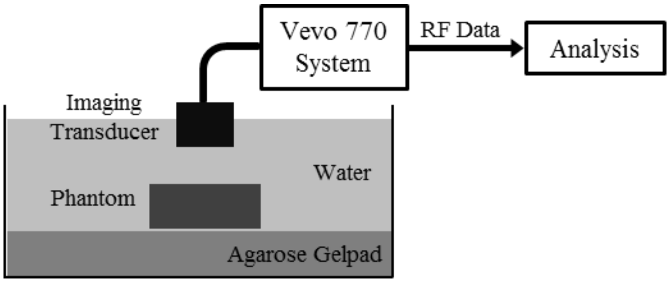

Figure 2.1 Schematic of experimental setup used for spectral ultrasound imaging of phantom.

2.2.3 Analysis

Theoretical frameworks that relate ultrasound spectral parameters to scatterer properties were developed by Lizzi and Insana [1, 3]. These frameworks make several critical assumptions, some of the key assumptions being (1) randomly but statistically uniformly distributed scatterers in space, (2) effective diameters of the scatterers are much smaller than -3 dB beamwidth (3) weak scattering, (4) weakly focused transducer, (5) scattering is isotropic and to occur at or beyond the focal region of the transducer. With these assumptions, the spectra (in dB) from small isotropic scatterers will have the form,

$$S'(f) = \left(\tfrac{10}{\ln 10}\right)\left[\ln E + n\ln(f) - 52.8 f^2 a^2 + \ln\left(a^{2(n-1)} C Q^2\right)\right] \tag{2.1}$$

where f is in MHz, a is in mm, C is the # concentration of the scatterers in #/mm^3, Q is the relative acoustic impedance and n and E are evaluated as follows for different types of scatterers:

$$\text{Isotropic: } E = 0.64\left[\left(\frac{2\pi}{c}\right)^4 \frac{\pi a_t^2 L}{3R^2}\right]; \quad n = 4 \tag{2.2}$$

$$\text{Cylindrical: } E = 0.23\left[\left(\frac{2\pi}{c}\right)^3 \frac{\pi a_t L}{3R}\right]; \quad n = 3 \tag{2.3}$$

$$\text{Planar: } E = 4.85\left[\left(\frac{2\pi}{c}\right)^2 L\right]; \quad n = 2 \tag{2.4}$$

Linear regression analysis is applied to the spectra to estimate the spectral parameters. The expressions for slope (m) and mid-band fit (M) are:

$$m = \int_{f_1}^{f_2} S'(f)(f - f_c)\,df \Big/ \int_{f_1}^{f_2} (f - f_c)^2\,df \tag{2.5}$$

$$M = \int_{f_1}^{f_2} S'(f)\,df \,/\, (f_2 - f_1) \tag{2.6}$$

where f_1 and f_2 are the minimum and maximum frequencies in the bandwidth and f_c is the center frequency. After algebraic simplification,

$$m = g_1(f_1, f_2)n - g_2(f_1, f_2)a^2 \tag{2.7}$$

$$M = \left(\tfrac{10}{\ln 10}\right)\left[\ln E + \ln\left(a^{2(n-1)} C Q^2\right)\right] + g_3(f_1, f_2)n + g_4(f_1, f_2)a^2 \tag{2.8}$$

$$where\ \ g_1(f_1, f_2) = 3\left(\frac{10}{\ln 10}\right)\left[\left(f_2^2 - f_1^2\right) - 2 f_1 f_2 \ln\left(\frac{f_2}{f_1}\right)\right] \Big/ \left(f_2 - f_1\right)^3 \tag{2.9}$$

$$g_2(f_1, f_2) = \left(\frac{10}{\ln 10}\right)\left[\frac{1}{1.17^2}\left(\frac{2\pi}{c}\right)^2\right]\left(f_1 + f_2\right) \tag{2.10}$$

$$g_3(f_1, f_2) = \left(\frac{10}{\ln 10}\right)\left[\left(\frac{f_2 \ln f_2 - f_1 \ln f_1}{f_2 - f_1}\right) - 1\right] \tag{2.11}$$

$$g_4(f_1, f_2) = -\left(\frac{10}{\ln 10}\right)\left[\frac{1}{1.17^2}\left(\frac{2\pi}{c}\right)^2\right]\left(f_1^2 + f_2^2 + f_1 f_2\right) \tag{2.12}$$

The spectral intercept can be evaluated by using the expression, $I = M - mf_M$, where f_M is the mid-band fit frequency in MHz.

2.2.3.1 Scatterer Size

The spectral parameters were corrected for the attenuation (α, dB/(cm-MHz)) of the tissue construct as $m=m+2\alpha z$ and $M=M+2\alpha z f_M$ where z is the ultrasound propagation distance in the tissue construct until the spectral cell. The scatterer radius can be calculated using:

$$a = \sqrt{\frac{g_1(f_1, f_2)n - m}{g_2(f_1, f_2)}} \tag{2.13}$$

2.2.3.2 Scatterer Concentration

With known value of Q, Eq. (2.8) can be rearranged to solve for C,

$$C = \frac{e^{0.23\left(MBF - g_3 n - g_4 a^2\right)}}{E a^{2(n-1)} Q^2} \tag{2.14}$$

Relative acoustic impedance, Q, of MC3T3 cells is estimated from various known # concentration, C, of the cells and is then used in the cell differentiation study to estimate C.

2.3 Results and Discussion

2.3.1 Analytical Results

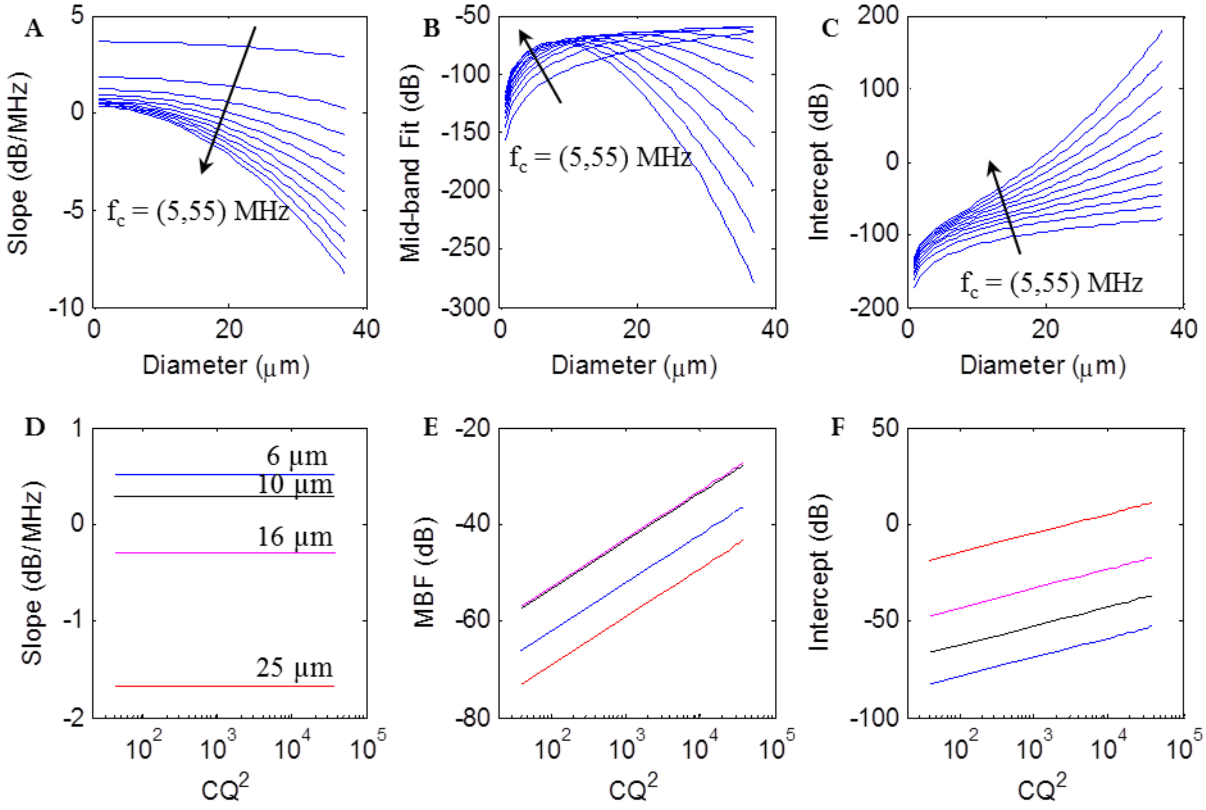

Figure 2.2 Analytical predictions of linear regression spectral parameters (A) Slope, (B) Mid-band Fit and (C) Intercept with diameter at different central frequencies. (D-F) are the corresponding parameter variations with acoustic concentration on a log scale at 6, 10, 16 and 25 μm scatterer diameters.

The relation between the spectral parameters and the tissue properties are shown in Eqs (2.13) and (2.14). For a given ultrasound imaging system, the slope depends only on the scatterer radius, *a*. For very small *a*, only the first term is significant in Eq. (2.7). As *a* increases, the slope decreases in proportion to a^2 for all scatterer types. Representative behavior of slope dependence on scatterer radius is shown in Figure 2.2A for isotropic scatterers at different transducer center frequencies with 100% fractional bandwidth. As the center frequency increases, the spectral slope varies more significantly with scatterer radius, hence a better contrast is obtained with high center frequency of the transducer in characterizing scatterers of different sizes. The independent behavior of slope with acoustic concentration is seen in Figure 2.2D.

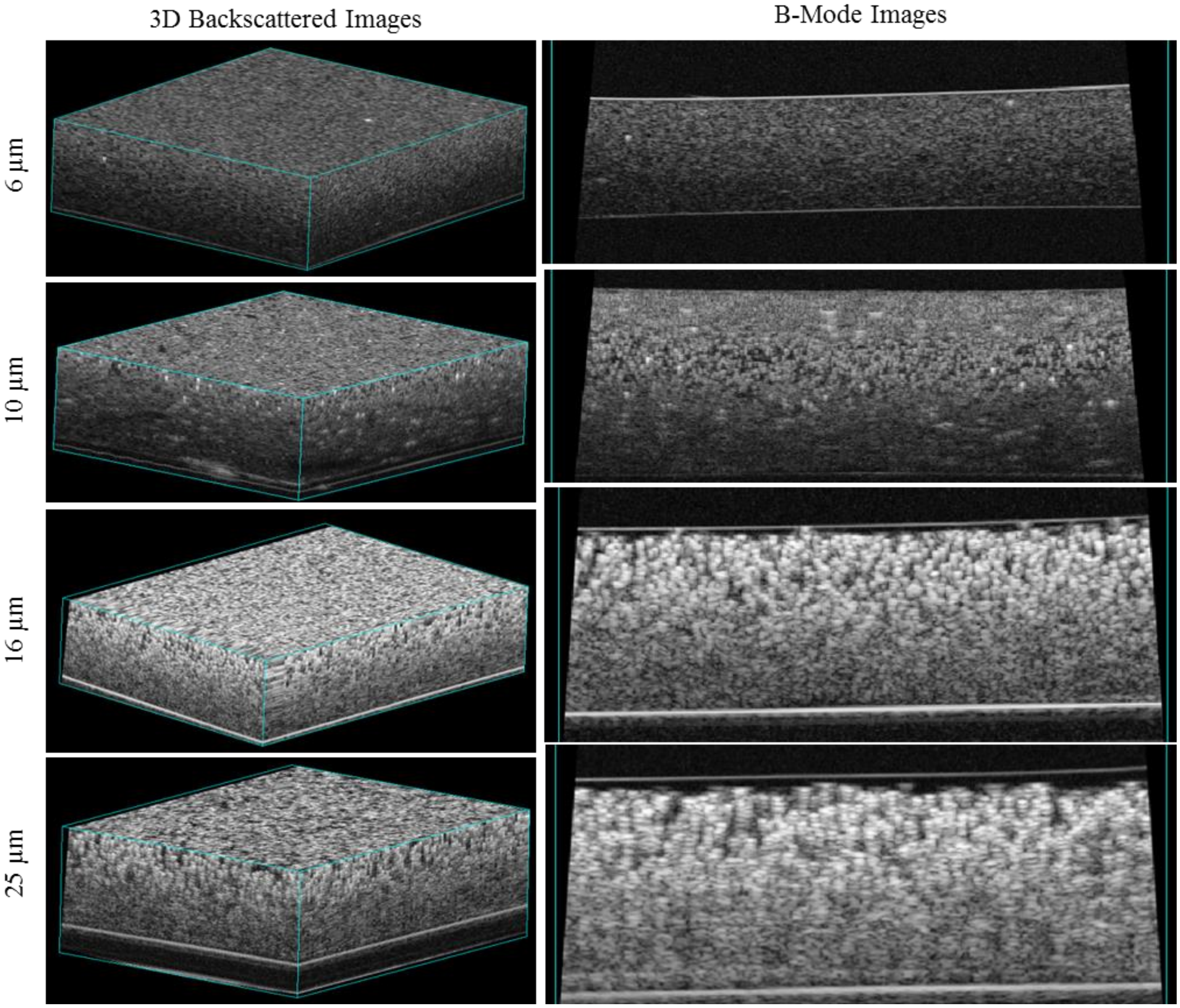

Figure 2.3 3D backscattered images (left panel) and B-mode images (right panel) of the 6, 10, 16 and 25 µm diameter polybead phantoms.

The variation of M with CQ^2 at different scatterer radii are shown in Figure 2.2B for various transducer center frequencies. As the frequency increases, the dependence of M on scatterer diameter becomes convex in nature. From the Eq. (2.8), M varies linearly with $\log(CQ^2)$ for a certain scatterer diameter and can be seen in Figure 2.2E. The intercept increases significantly with scatterer diameter for D > 20 µm for transducers with high center frequencies

(Figure 2.2C). The intercept doesn't show any convex nature with scatterer diameter and increases with increase in diameter due to increased backscattering. Even the intercept varies linearly with log(CQ^2) for a certain scatterer diameter, Figure 2.2F.

2.3.2 Phantom Results

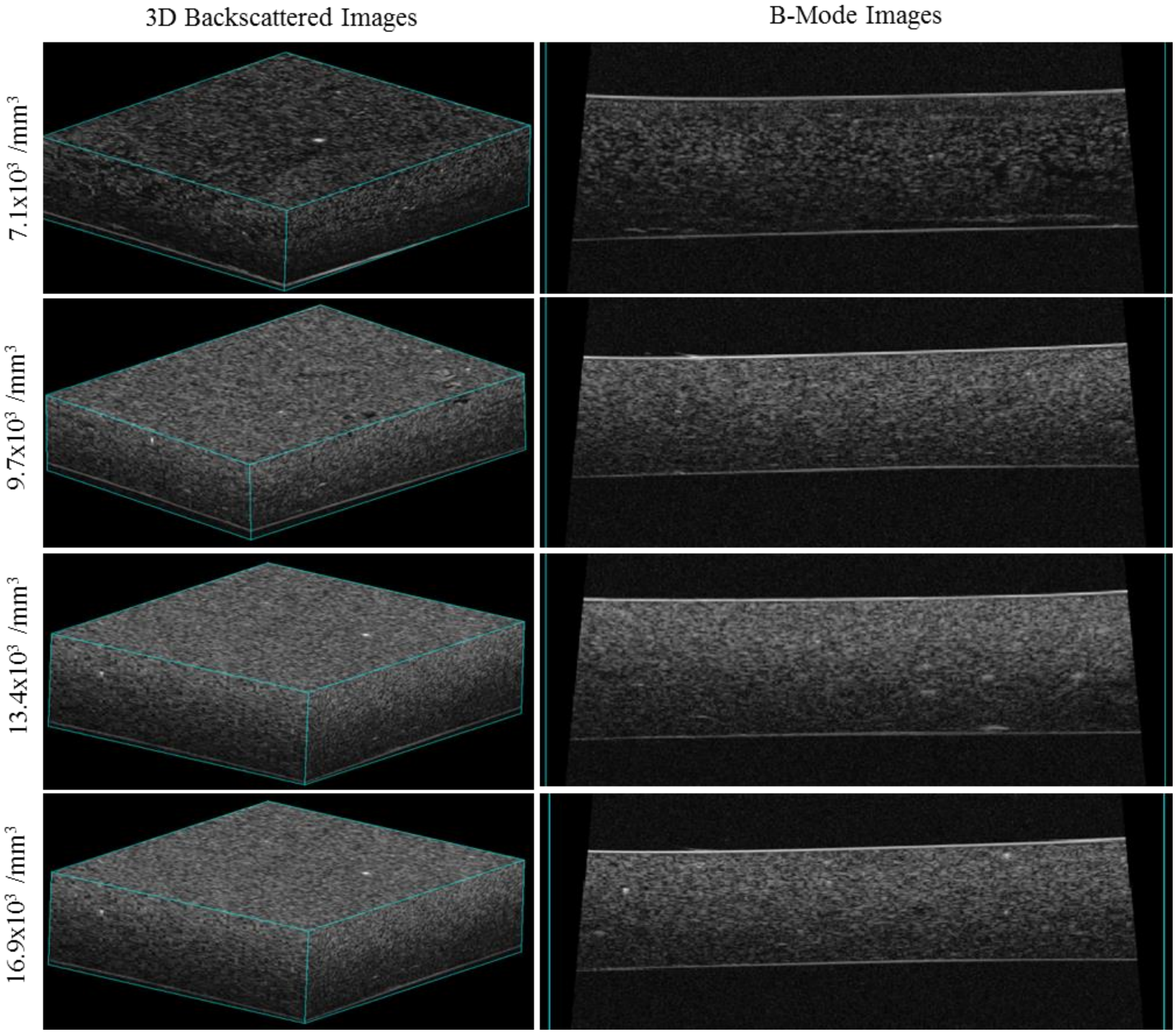

Figure 2.4 3D backscattered images (left panel) and B-mode images (right panel) of the 6 µm diameter polybead phantoms at 7.1, 9.7, 15.4 and 21.9 x10^3 beads/mm^3.

Ultrasound backscattered 3D and B-mode images of 6, 10, 16 and 25 µm diameter polybead phantoms are shown in Figure 2.3. The contrast in the size of the polybeads across these phantom B-mode images is a bit evident along with the increased backscattering strength as the polybead size increases. B-mode images of 6 µm diameter polybead phantoms at 4 different polybead concentrations are shown in Figure 2.4 with an evidently increased backscattering strength with polybead concentration.

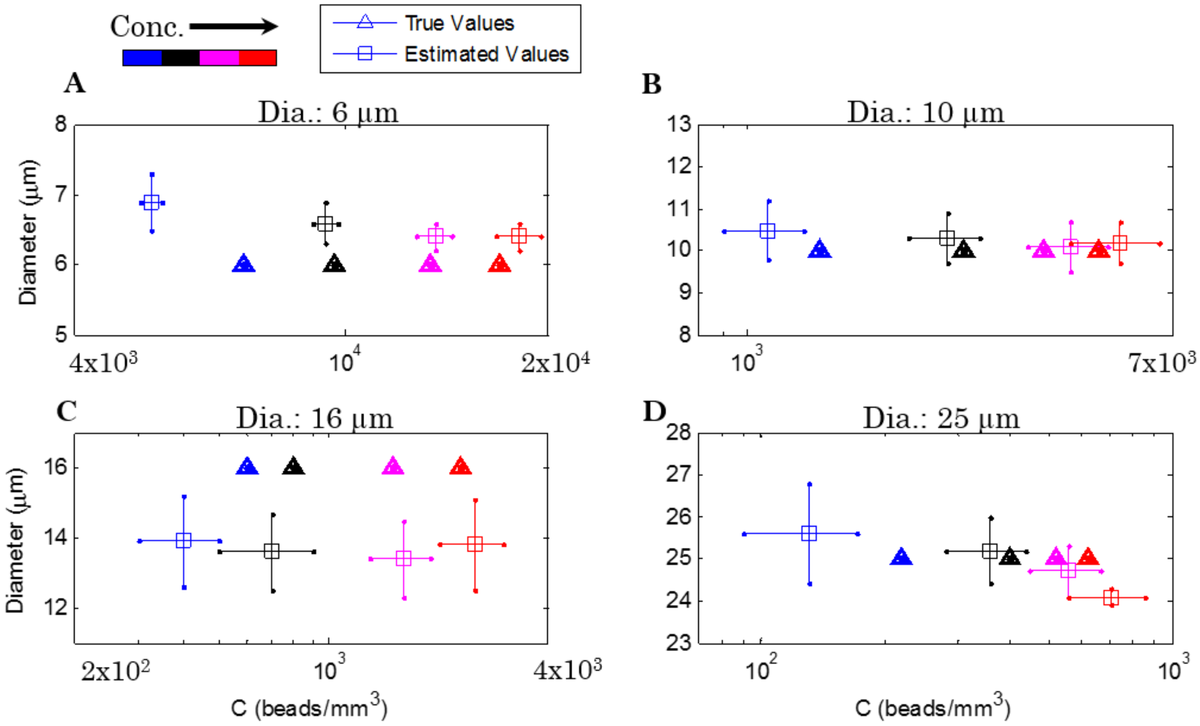

Figure 2.5 Estimated diameter against estimated concentration for (A) 6 µm, (B) 10 µm, (C) 16 µm and (D) 25 µm diameter polybead phantoms at 4 different concentrations. True/Predicted values are indicated by points and the estimated values by errorbars.

With known speed of sound & density of Agar and polybeads, 1480 m/s & 1000 kg/m^3 and 2350 m/s & 1060 kg/m^3 respectively, the relative acoustic impedance of the phantoms was estimated as 0.68. The spectral parameters were estimated and the microstructural properties, size and concentration of the polybeads are shown in Figure 2.5. The concentration of the beads increases from blue to red. The predicted values are represented by points with markers whereas the estimated values by errorbars with markers. The estimated spectral parameters track the theoretically predicted values well. The mean percentage errors in size and concentration estimations were 7% and 14% respectively. Relatively higher percentage error in concentration estimations from the predicted values might be due to any local inhomogeneous spatial distribution of the polybeads and any clustering of the polybeads. For each scatterer size, spectral slope is a horizontal line w.r.t concentration, C, of the beads indicating its non-dependence nature on C. As the size increases, the spectral slope decreases due to its inverse dependence. M and I showed a linear relationship with $\log(C)$, similar to the ones in Figure 2.2E and 2.2F. Again, the intercept values show a constant increase with bead diameter due to increased backscattering strength. The diameter estimation is non-dependent on concentration as expected.

2.4 Conclusion

Spectral parameters obtained from polybead phantom experiments show good agreement with those predicted by the theory. This successful estimation will provide a better means for determining tissue-scatterer properties. These preliminary studies show promise for establishing an extended framework that will be useful for quantitatively assessing tissue architecture to diagnose HIFU ablation process, characterize the mineral content in acellular constructs and to monitor cell differentiation process in MC3t3 constructs, discussed in later chapters.

2.5 References

[1] F. L. Lizzi, M. Ostromogilsky, E. J. Feleppa, M. C. Rorke, and M. M. Yaremko, "Relationship of ultrasonic spectral parameters to features of tissue microstructure," *IEEE Trans. Ultrason. Ferroelectr. Freq. Control*, vol. 34, pp. 319-329, May 1987.

[2] M. L. Oelze and J. F. Zachary, "Characterization of tissue microstructure using ultrasonic backscatter: Theory and technique for optimization using a Gaussian form factor," *Journal of the Acoustical Society of America,* vol. 112, pp. 1202-1211, Sep 2002.

[3] M. F. Insana, R. F. Wagner, D. G. Brown, and T. J. Hall, "Describing Small-Scale Structure in Random-Media Using Pulse-Echo Ultrasound," *Journal of the Acoustical Society of America,* vol. 87, pp. 179-192, Jan 1990.

[4] J. Mamou, M. L. Oelze, W. D. O'Brien, and J. F. Zachary, "Extended three-dimensional impedance map methods for identifying ultrasonic scattering sites," *Journal of the Acoustical Society of America,* vol. 123, pp. 1195-1208, Feb 2008.

[5] M. L. Oelze and J. F. Zachary, "Examination of cancer in mouse models using high-frequency quantitative ultrasound," *Ultrasound in Medicine and Biology,* vol. 32, pp. 1639-1648, Nov 2006.

[6] S. Dasgupta, E. J. Feleppa, J. Mamou, and M. J. Rondeau, "Validating the Theory Relating Ultrasonic Spectral-parameter Values to Scatterer Properties," *2006 Ieee Ultrasonics Symposium, Vols 1-5, Proceedings,* pp. 633-636, 2006.

[7] R. E. Baddour, M. D. Sherar, J. W. Hunt, G. J. Czarnota, and M. C. Kolios, "High-frequency ultrasound scattering from microspheres and single cells," *Journal of the Acoustical Society of America,* vol. 117, pp. 934-943, Feb 2005.

[8] M. C. Kolios, G. J. Czarnota, M. Lee, J. W. Hunt, and M. D. Sherar, "Ultrasonic spectral parameter characterization of apoptosis," *Ultrasound in Medicine and Biology,* vol. 28, pp. 589-597, May 2002.

[9] M. L. Oelze and W. D. O'Brien, "Application of three scattering models to characterization of solid tumors in mice," *Ultrasonic Imaging,* vol. 28, pp. 83-96, Apr 2006.

[10] J. Mamou, M. L. Oelze, W. D. O'Brien, and J. F. Zachary, "Identifying ultrasonic scattering sites from three-dimensional impedance maps," *Journal of the Acoustical Society of America,* vol. 117, pp. 413-423, Jan 2005.

CHAPTER 3

Characterization of Acellular Constructs

The objective is to correlate the amount of mineral present in the constructs with ultrasound parameters. The spectrum of the ultrasound backscattered signals contains the information about physical and acoustic properties of the scatterer (mineral) and is exploited to determine the size and concentration of the mineral in the construct. First, acellular collagen hydrogels were prepared and imaged using ultrasound to observe its scattering properties. Then, hydroxyl-apatite (HA) mineral was added to the collagen hydrogel during the preparation process. Three different types of HA minerals varying in their mineral size were chosen to observe their distribution and scattering properties under ultrasound. Sonication, a process of mixing and fragmentation of clusters into smaller particles, was applied on the HA mineral before it is added to the construct to improve the distribution of HA mineral in the construct. Once the type of HA mineral that is distributed uniformly within the construct and the effect of sonication in improving the distribution are determined using the ultrasound, constructs were made with that chosen HA type at three different densities to characterize its amount using ultrasound parameters. Next, the process of mineral deposition from surrounding fluid medium onto simple collagen constructs was studied. When a collagen construct is placed in a medium containing minerals, the mineral present in the fluid medium will start depositing on the construct due to the concentration difference of the mineral. The rate of mineral deposition on the construct depends on the concentration of the minerals in the medium and whether the minerals are in supersaturated state or in dissolved state at a certain temperature. With PBS, 2.5x SBF and 5x SBF as media, the changes in morphology, the amount of calcium deposited on the construct was studied over time and the later was compared with spectral mid-band fit parameter for correlation. The results from this study are published in "Tissue Engineering Part C: Methods", volume 18, issue 12, 2012 with the title, "Non-invasive, Quantitative, Spatiotemporal Characterization of Mineralization in Three-Dimensional Collagen Hydrogels using High-Resolution Spectral Ultrasound Imaging" [1].

3.1 Materials and Methods

The tissue constructs were manufactured in Cell-Matrix Interactions & Tissue Engineering (CMITE) lab, Department of Biomedical Engineering.

3.1.1 3D Collagen Hydrogel Fabrication

Collagen type I (MP Biomedicals, Solon OH) was dissolved at 4.0 mg/ml in cold 0.02 N acetic acid overnight. Constructs were created [2] by mixing 10% fetal bovine serum, 10% 1x Dulbecco's modified Eagle's medium (DMEM), 20% 5x DMEM, 10% 0.1 N NaOH and 50% solubilized collagen (obtained solubilizing 4 mg/ml collagen type I in 0.02 N acetic acid overnight) at 4°C for a final collagen concentration of 2 mg/ml. The mixture (500 µl) was then injected into a 24 well plate and allowed to gel at 37°C for 45 mins.

3.1.2 Addition of Hydroxyapatite to 3D Hydrogels

Composite collagen-hydroxyapatite (HA) hydrogels were fabricated by adding particulate HA directly to the gel mixture. Three types of hydroxyapatite, reagent-grade (HA-R; Sigma), micro- (HA-M; Plasma Biotal Ltd.), and nano- (HA-N; Sigma), were incorporated within collagen gels. The average size diameter of the HA sources were 590 µm, 5 µm, and less than 200 nm, for HA-R, HA-M, and HA-N, respectively. HA solution stock of 200 mg/ml HA in 1x DMEM was prepared and autoclaved at 120°C for 20 minutes to maintain sterility. A 10 mg/ml collagen-HA hydrogel was fabricated by adding 5% HA-stock, 5% 1x DMEM, 10% FBS, 20% 5x DMEM, 10% 0.1 N NaOH, and 50% collagen and gelation was initiated as described earlier. Other concentrations of composite collagen-HA hydrogels were created by adding or diluting the stock HA by the appropriate factors to fabricate tissue constructs with 5 mg/ml and 20 mg/ml HA. For dispersion studies, stock HA and 1x DMEM (10% of final gel) were mixed at 4°C and placed in a water-bath sonicator for 1 hour to disrupt particle aggregates. The HA-DMEM mixture was then added immediately to the collagen pre-gel mixture and gelation was initiated as previously described.

3.1.3 Mineralization in Simulated Body Fluid

Prepared simulated body fluid (SBF) [3] had final ion concentrations of 141 mM NaCl, 4 mM KCl, 2.5 mM $CaCl_2$-H_2O, 1 mM $MgCl_2$, 4.2 mM $NaHCO_3$, 0.8 mM $MgSO_4$, and 1 mM KH_2PO_4 . Solutions of 2.5x and 5x SBF were prepared by increasing the concentrations of each reagent by the necessary factor. Collagen hydrogels were fabricated as described previously and incubated at 37°C in either PBS, 2.5x SBF, or 5x SBF. Samples were imaged at days 3, 7, 10, 14, and 21. Calcium deposited on collagen hydrogels after incubation in PBS, 2.5x SBF, and 5x SBF was quantified experimentally at days 3, 7, 10, 14, and 21 using an orthocresolphthalein complex-one (OCPC) method [4].

3.1.4 Ultrasound Imaging and Data Acquisition

Figure 3.1 [1] shows a schematic diagram of the imaging setup that includes a 90 mm diameter Petri dish filled with PBS at room temperature. Collagen constructs were placed on top of an agar gel pad, which reduces the reflection from the bottom of the dish. Ultrasound imaging was performed with a Vevo 770 (VisualSonics Inc., Toronto, Canada) using an RMV 708 imaging probe with a nominal 55 MHz center frequency, 20-75 MHz bandwidth (−6 dB), 4.5 mm focal distance, and 1.5 mm depth of focus (−6 dB). 3D backscattered RF data from the tissue construct were collected at either 100% or 10% scanner power and 420 MS/s by performing multiple B-mode scans using an automatic 3D translational controller. The interval between adjacent A-lines and B-mode scans were 31 μm and 64 μm, respectively. After each RF acquisition of a construct, a reference RF acquisition of the setup without the construct was collected.

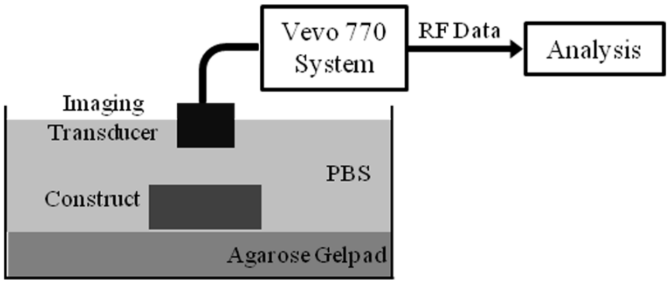

Figure 3.1 Schematic of experimental setup used for spectral ultrasound imaging of tissue construct.

3.1.5 Data Analysis

With known speed of sound in the surrounding fluid medium (C_f), the thickness of the construct can be found using $Thickness = C_f\left[\left(t_{bottom} - t_{top}\right) + \left(t_{pad}^{ref} - t_{pad}^{construct}\right)\right]$, where t_{top} is the time of arrival of the ultrasound pulse at the construct's top surface, t_{bottom} at the bottom surface,

$t_{pad}^{construct}$ at the bottom reflector with construct and t_{pad}^{ref} at the bottom reflector without the construct. The speed of sound in the construct can then be evaluated using $C_{construct} = \frac{Thickness}{\left(t_{bottom} - t_{top}\right)}$.

GS and spectral parameters were calculated on the 3D RF data of the construct. The density of analysis parameters were calculated as $X\ Density = \frac{\int_V X\ dV}{V}$, where X is either GS or spectral parameters evaluated in volume V of the tissue construct. In case of signal saturation, the time windows in which the signal is saturated are discarded in the analysis process. The ultrasound backscattering from collagen construct alone (without mineral) was very poor and its mean *GS* value in 0.1 μs time window is very close to that of backscattering from fluid medium. A threshold *GS* value based on collagen construct for determining the mineral lacking regions in the construct was obtained. Any analysis in this region would be uninformative due to poor scattering and hence are discarded from the analysis process.

3.1.6 Statistical Analysis

Analysis was carried out on a 0.5 mm x 5.0 mm x thickness (~2 mm) volume of each construct and the data are presented as mean ± standard deviation. Statistical comparisons between any two parameters were made using Student’s t-test for paired samples and the differences were considered significant at a level of $p<0.05$.

3.2 Results

3.2.1 Virtual Histology

The setup used in this study allowed rapid and noninvasive 3D imaging of collagen constructs while still in incubating culture medium. Image acquisition was completed in a few seconds at a frame rate of 45 Hz, and saving of the raw RF data required 2-3 minutes. In the present study, construct boundaries were determined manually based on GS thresholding, though this process could be automated and accelerated in the future. Overall, analysis of each construct using SUSI required about 5-10 minutes.

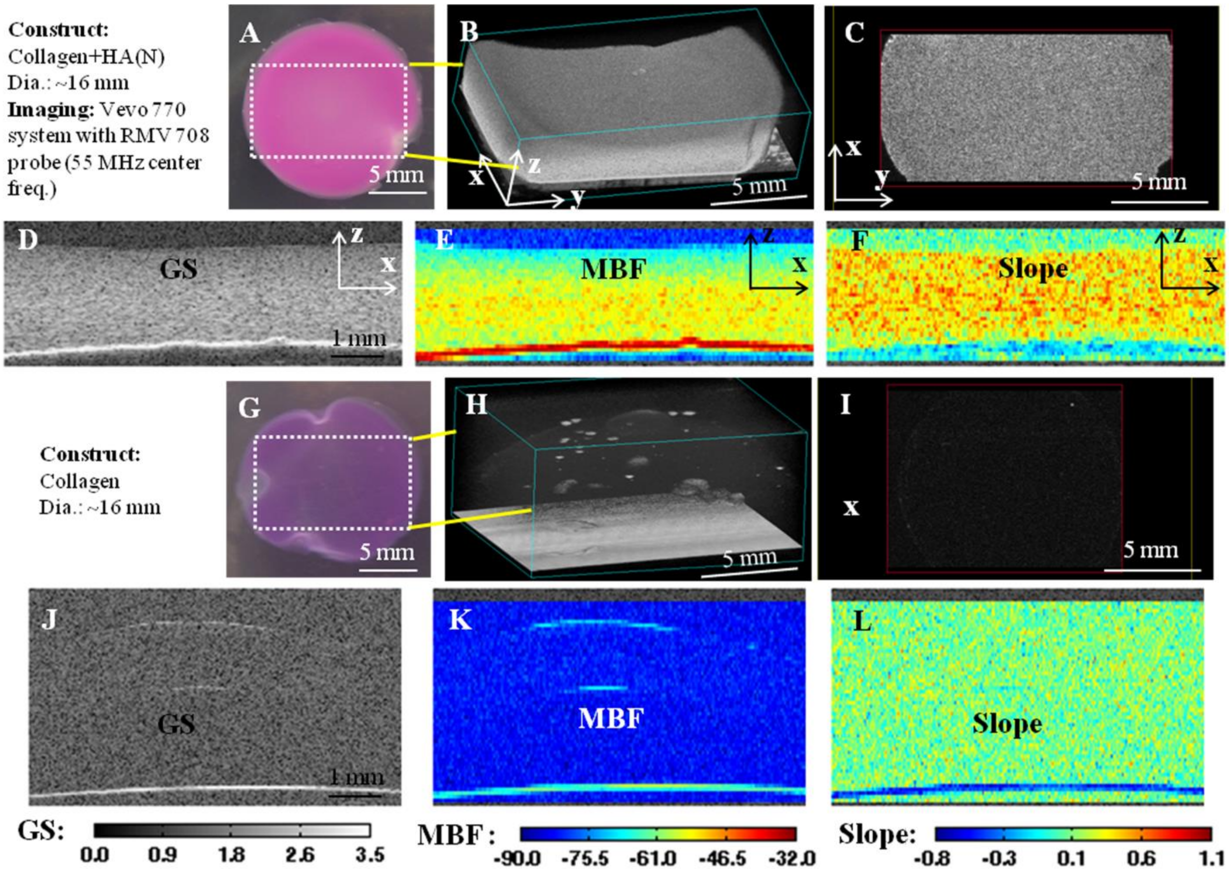

Figure 3.2 Virtual histology of 3D collagen constructs. Panels A-F show a collagen construct with added HA-N mineral, and panels G-L show corresponding images of a pure collagen control construct. (A, G) Color images of the top view of constructs. (B, H) 3D ultrasound rendered image of the section represented by white dotted box in A and G. (C, I) Ultrasound C-scans of a transverse xy-plane. (D, J) Grayscale (GS), (E, K) mid-band fit (MBF) and (F, L) slope images of one section in the xz-plane.

Figure 3.2 [1] shows a representative example of ultrasound imaging and analysis output from a collagen hydrogel containing HA-N mineral (Fig 2A-2F), as well as a “control” construct of pure collagen (Fig 3.2G-3.2L). The photographs of the construct (Fig. 2A, 2G) show a top view (xy-plane) and the region that was imaged is indicated by the dotted rectangle. The 3D volume-rendered ultrasound images (Fig. 3.2B, 3.2H) show the overall dimension and morphology of the construct. This digital reconstruction can be rotated and/or sectioned to provide any desired viewing prospective. Figure 3.2C is an image in the xy-plane at a defined depth (known as a C-scan) of the 3D of the HA-N construct, and shows homogeneous speckles indicative of uniform spatial distribution of mineral in the construct. Similarly, a GS image in an xz-plane of the HA-N construct (Fig. 3.2D) shows a mainly homogeneous distribution of mineral in the lateral (x) and depth (z) directions, as well as evidence of mineral settling at the bottom of the construct. The corresponding MBF image of the calibrated RF power spectrum (Fig. 3.2E), which is related to scatterer radius and concentration in the construct, shows an increasing concentration of scatterer toward the bottom of the HA-N construct. In contrast, the slope parameter (Fig. 3.2F), which varies inversely with scatterer radius, is relatively homogeneous in the bulk of the HA-N construct but decreases near the bottom of the construct, indicating settling of larger particles or cluster formation by the mineral. The corresponding rendered and RF spectrum images for the control construct (Fig 3.2H-3.2L) show very little signal, demonstrating that SUSI can discriminate between mineral-containing and pure collagen materials.

3.2.2 HA mineral sources and effect of sonication

Three different types of HA mineral sources of same concentration (10 mg/ml) were added in the collagen hydrogels to characterize the type of HA mineral source using ultrasound imaging. Sonication of the mineral during the construct manufacturing process was performed to observe its effect on distribution of the mineral in the construct. Each column of Fig. 3.3 [1] shows parametric images (3D rendered, GS and spectral parameters) for each type of HA source (R, M and N). The bottom half images of the figure contrasts the effect of sonication with unsonicated constructs in the top half images. The left half of Fig. 3.3B$_i$ and 3.3E$_i$ (i = 1, 2 and 3) shows GS and right half shows MBF. Similarly, left half of Fig. 3.3C$_i$ and 3.3F$_i$ shows GS and right half shows slope. In spectral analysis and graphic representation, pixels with very low scattering (locations of mineral lacking collagen) and saturated RF data were not analyzed and represented. Higher backscattering at the bottom layer of the construct is due to the settling of HA mineral and is high in HA-R compared to HA-M and HA-N due to its larger particle size and weight. Being smaller in size, HA-N is distributed more uniformly throughout the construct compared to HA-M and HA-R.

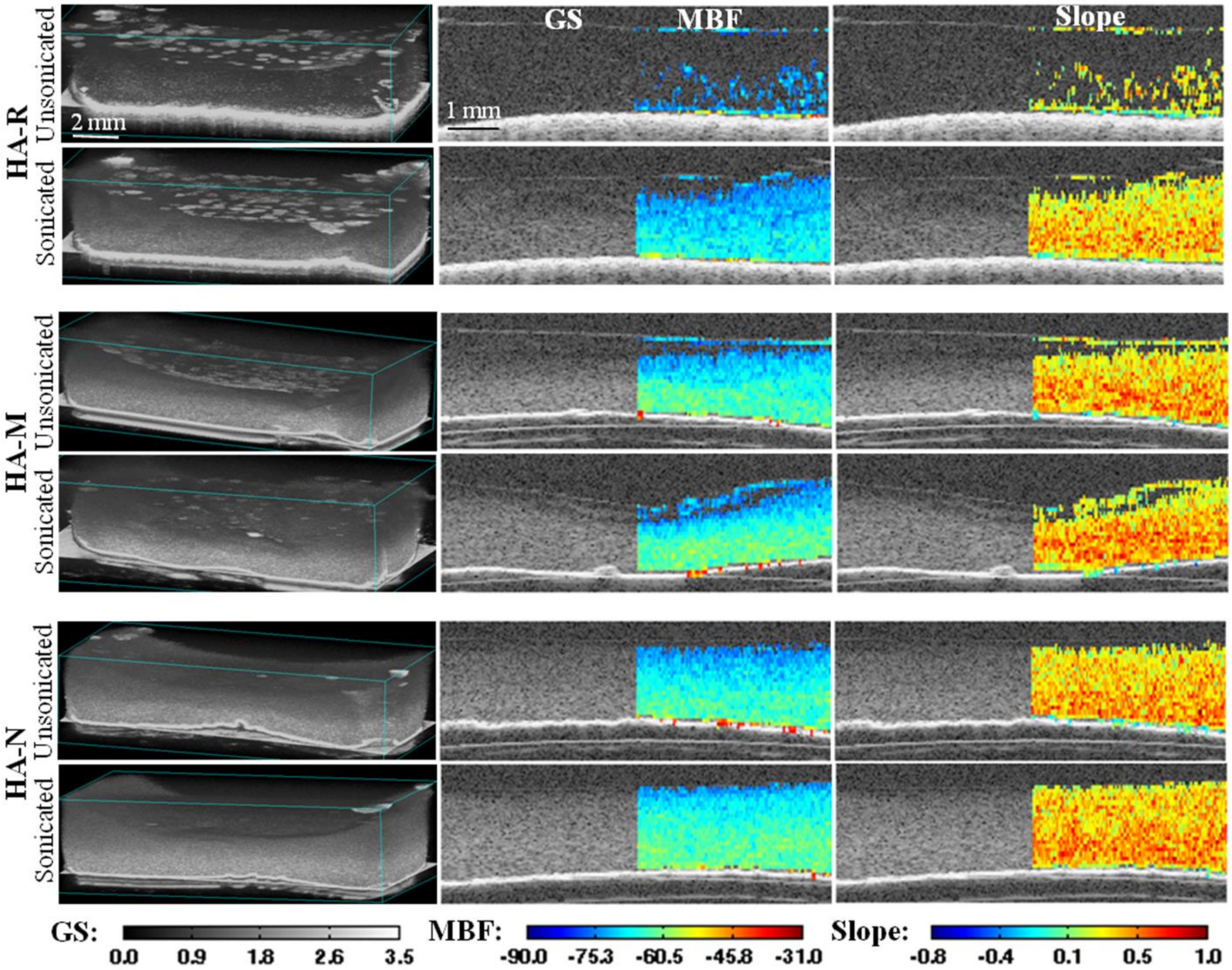

Figure 3.3 Parametric images (A_i through F_i) of collagen constructs with 3 different HA sources: R (i = 1), M (i = 2) and N (i = 3). (A_i) 3D rendered image of the construct. (B_i) Left half shows GS image and right half shows MBF image in one frame at mineral spotted locations excluding the saturated RF data at the bottom mineral layer. Similarly, right half of (C_i) shows spectral slope image. Constructs with sonication of HA sources during manufacturing are shown at the bottom half (D_i through F_i).

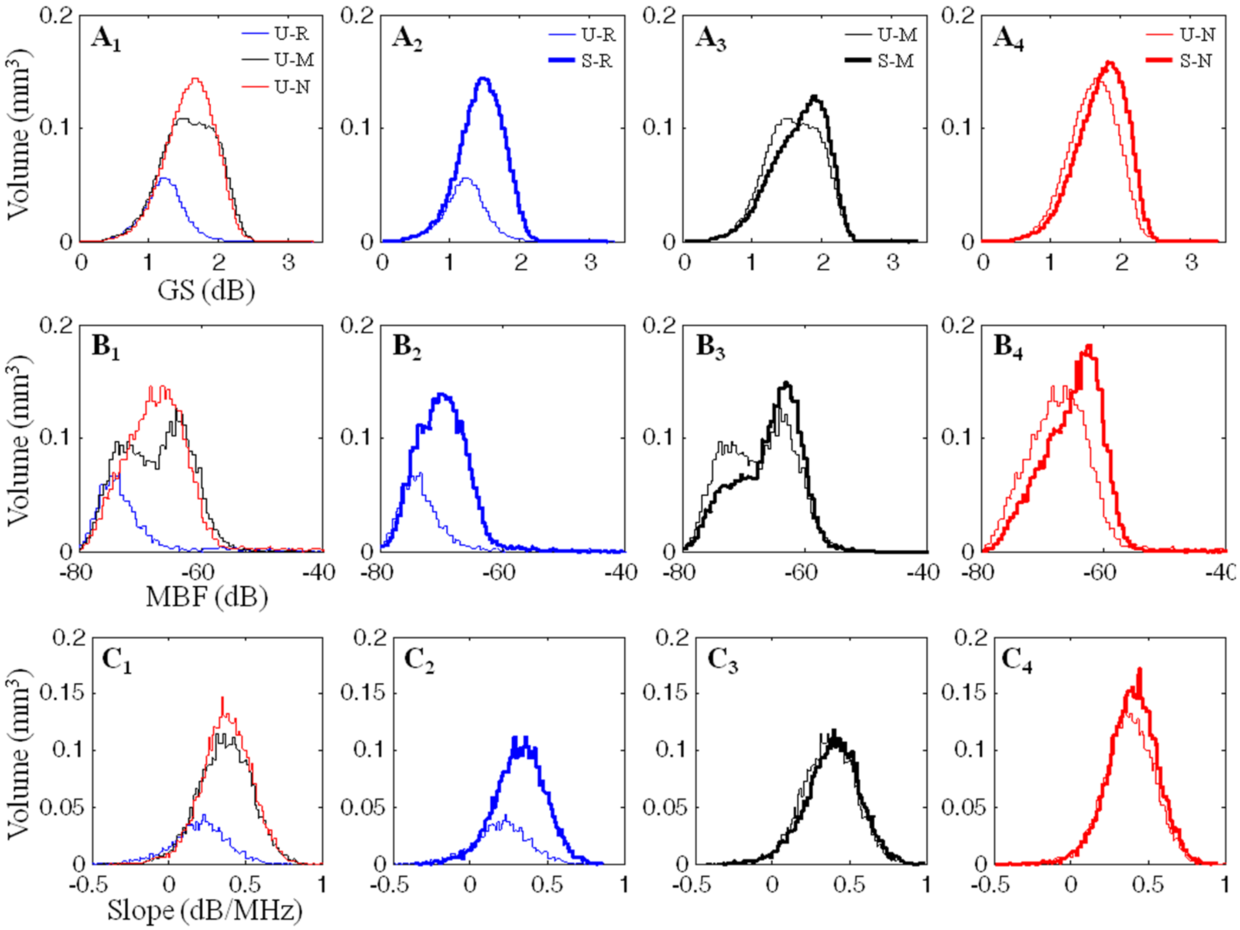

Figure 3.4 Histogram distributions of volume occupied by the mineral spotted with GS/MBF/Slope parameters: (A_1) Comparison of Grayscale (GS) distributions of unsonicated HA-R (blue), M (black) and N (red) constructs. $A_{i=2,3,4}$ shows comparison between distributions of sonicated (thick) and unsonicated (thin) constructs for HA type R, M and N respectively. Similar comparisons using mid-band fit (MBF) and spectral slope parameters are shown in $B_{i=1,2,3,4}$ and $C_{i=1,2,3,4}$ respectively.

Sonication process during construct manufacturing increased the distribution of HA mineral, particularly in HA-R (Fig. 3.3E_1 vs. 3.3B_1). GS, MBF and slope parameters were calculated on construct volume of 0.5 mm x 5 mm x thickness (~2 mm) for each HA type and process (unsonicated vs. sonicated). The histograms were constructed against the volume occupied by the mineral at parameter values. Higher area under the curve of the histogram and higher mean of the distribution in Fig. 3.4A_1 and 3.4B_1 (unsonicated HA-R, M and N) is a correspondence of homogeneous distribution of the mineral in the construct. Lower mean of slope for HA-R in Fig.

3.4C_1 correlated to its large particle size. The mean of slope for HA-M and N are very close, possibly due to the limit of the employed ultrasound probe unable to determine the small particle size of HA-N (mean dia. ~200 nm). Effect of sonication was compared against unsonicated constructs in 2nd to 4th columns for each HA source. Sonication improved the distribution of HA-R quite significantly and small improvement was observed in HA-M and N also.

Table 3.1 Mean and standard deviation of ultrasound parameters correspondence of HA mineral. (n=4 for each sample type)

Process	Parameter	HA mineral type		
		R (μ ± σ)	M (μ ± σ)	N (μ ± σ)
Unsonicated	GS (dB)	1.24 ± 0.33	1.45 ± 0.32	1.59 ± 0.39
	MBF (dB)	-72.2 ± 6.1	-69.8 ± 4.2	-67.4 ± 5.5
	Slope (dB/MHz)	0.20 ± 0.18	0.33 ± 0.16	0.37 ± 0.17
Sonicated	GS (dB)	1.68 ± 0.38	1.61 ± 0.37	1.73 ± 0.36
	MBF (dB)	-66.0 ± 5.1	-67.1 ± 5.6	-65.0 ± 4.9
	Slope (dB/MHz)	0.39 ± 0.17	0.38 ± 0.16	0.40 ± 0.16

3.2.3 Characterization of HA mineral density

HA-N mineral distributed more uniformly compared to HA-R and M and was chosen to characterize its concentration (or density) in the construct. Constructs with HA-N of 3 different concentrations (5, 10 and 20 mg/ml, *n* = 4 for each) were manufactured and imaged. Figure 3.5 [1] shows 3D renderings as well as GS, MBF and slope data for these constructs. The intensity of both the GS and MBF signals reflect the increasing HA content, while the slope values remain essentially unchanged. These data reflect that while the amount of HA in the constructs increased, the size of the HA particles remained the same. Figure 3.6 [1] shows correlations

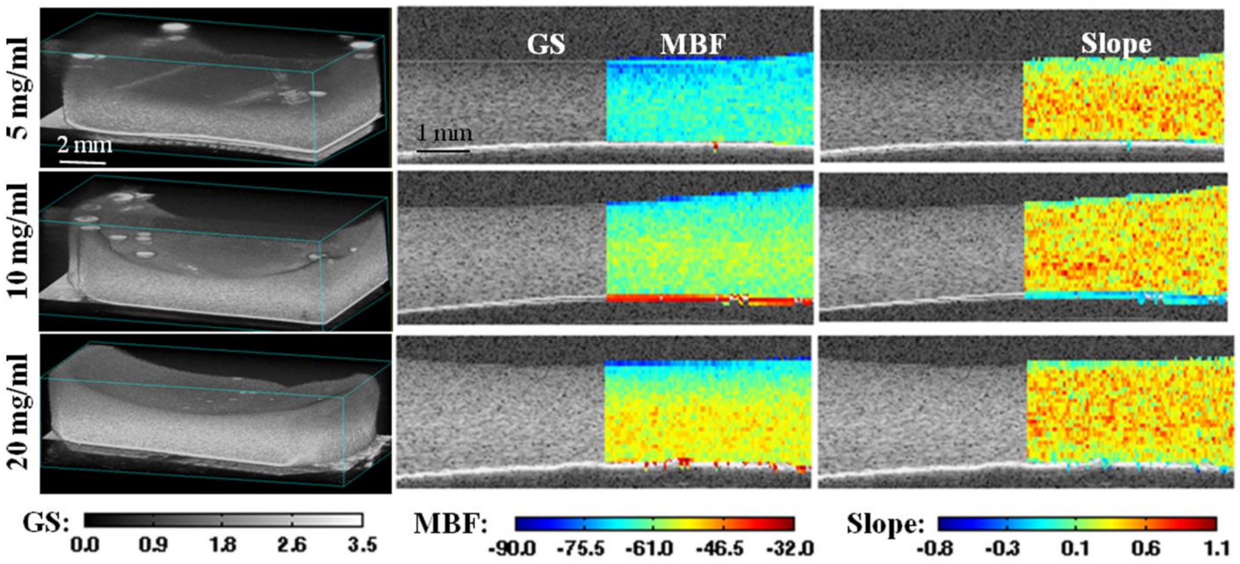

Figure 3.5 Ultrasound imaging of collagen-HA constructs made with three different concentrations of HA-N with sonication. First column shows 3D rendered images, second column shows GS and superimposed MBF, third column shows GS and superimposed slope. Rows show the HA-N concentration used to make the constructs.

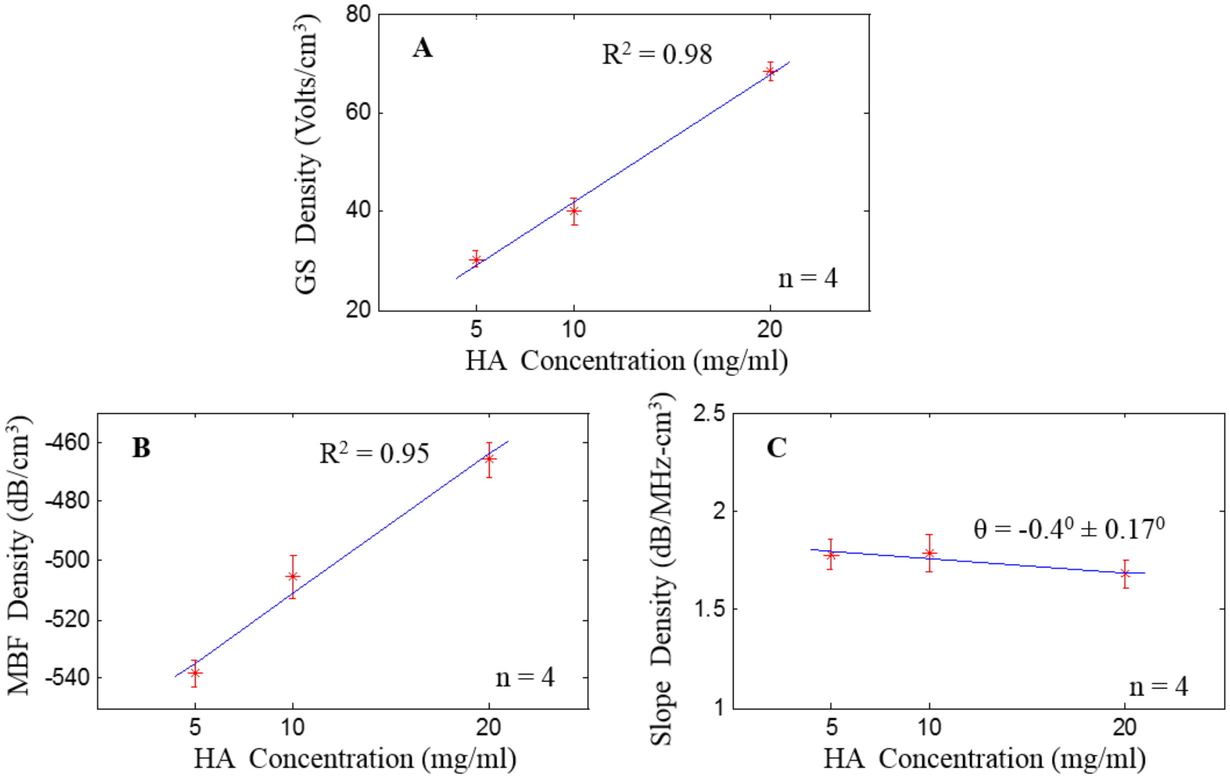

Figure 3.6 Correlation of sonicated HA-N mineral density with (A) GS density and (B) MBF density (C) Slope density. Nearly flat correlation for slope density is a correspondence of very close mineral sizes.

between the density of the GS, MBF, and slope parameters and the amount of HA added to the constructs. These data show a strong linear correlation (R^2 value of 0.98 and 0.95 respectively) between HA content and both the GS and MBF parameters. In contrast, the slope parameter was minimally affected by the concentration of HA, as would be expected when the particle size remains constant. The linear regression has a slight negative slope (-0.4°), possibly due to aggregation of mineral particles at higher concentration.

3.2.4 Development of collagen constructs in mineralizing media

The amount of deposition of calcium mineral from the fluid medium on to the collagen hydrogel over 3 weeks of time period, as an alternative to incorporating a mineral phase at the time of construct fabrication. Three fluid media, PBS (control), 2.5x SBF, 5x SBF were chosen to monitor and contrast the mineral deposition on the constructs and the resulting spectral ultrasound data at day 21 are shown in Figure 3.7 [1]. The medium was maintained at 37^0 C and at this temperature, the minerals in PBS will be in dissolved state whereas minerals in 2.5x SBF

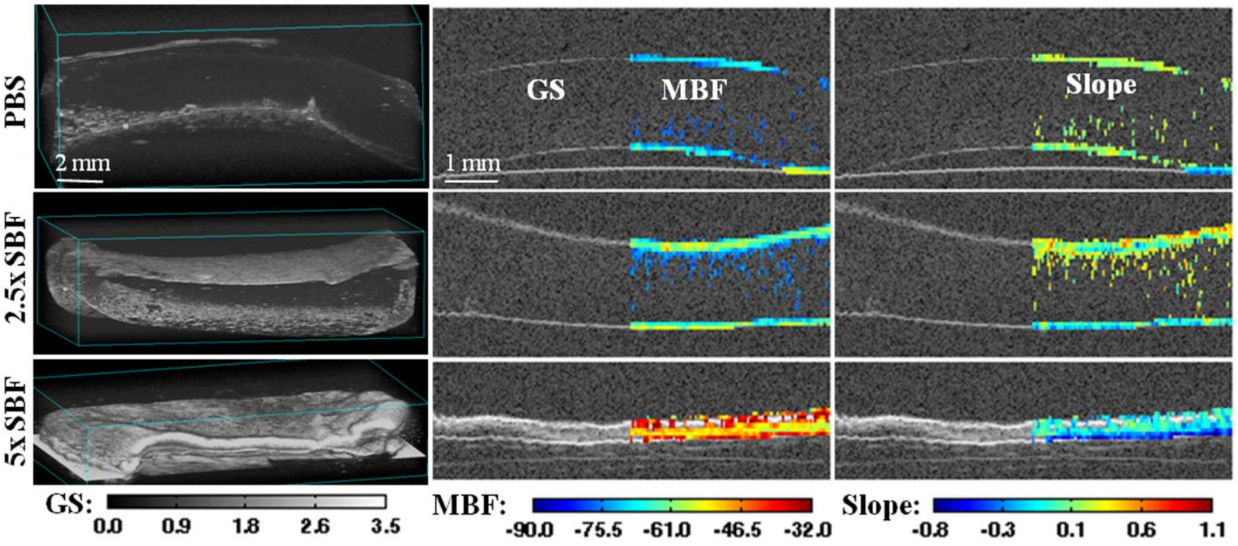

Figure 3.7 Collagen constructs exposed to mineralizing solution imaged at day 21 of incubation. First column shows 3D rendered images, second column shows GS and superimposed MBF, third column shows GS and superimposed slope. Rows show the incubation solution used.

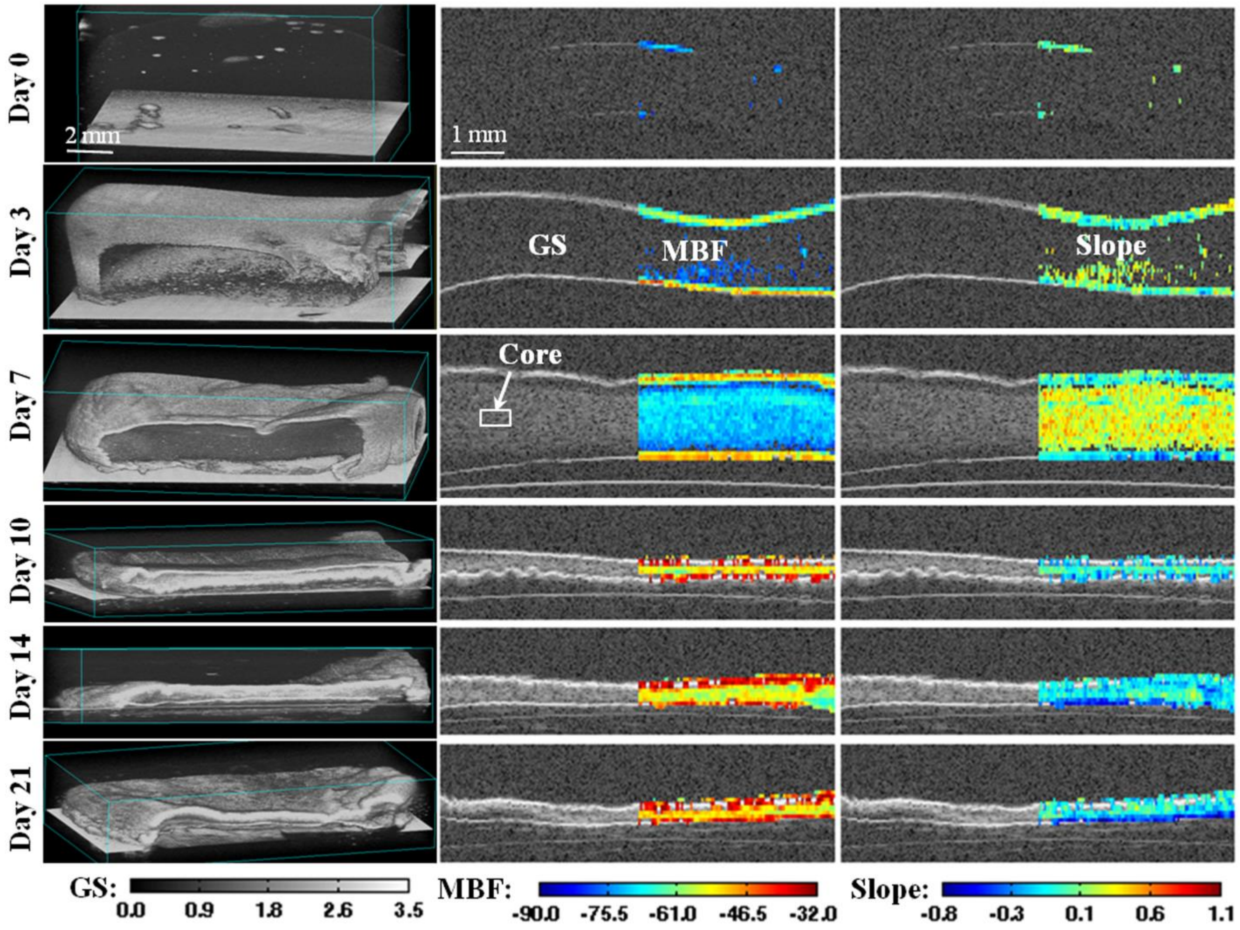

Figure 3.8 $A_{i=1to5}$ shows 3D rendered images of the collagen constructs with mineral deposited by day 3, 7, 10, 14 and 21 respectively. The left half of $B_{i=1to5}$ shows GS image and right half shows MBF image in one frame at mineral spotted locations excluding the saturated RF data, if any, at the top or bottom surface of the construct. Similar parametric images are shown in $C_{i=1to5}$ with right half as spectral slope image.

and 5x SBF will be in supersaturated state. Within 4 hours, nearly 50% of the calcium ions reported [5] to come out of the 5x SBF medium and deposit on the construct. The diameter of the spherical precipitates on the construct reported was approximately 12 µm.

Figure 3.8 [1] shows a temporal analysis of mineral deposition, using the 5X SBF constructs as an example because they demonstrated the most robust mineralization. The 3D renderings, GS images and MBF images show the pattern of mineral deposition, which clearly

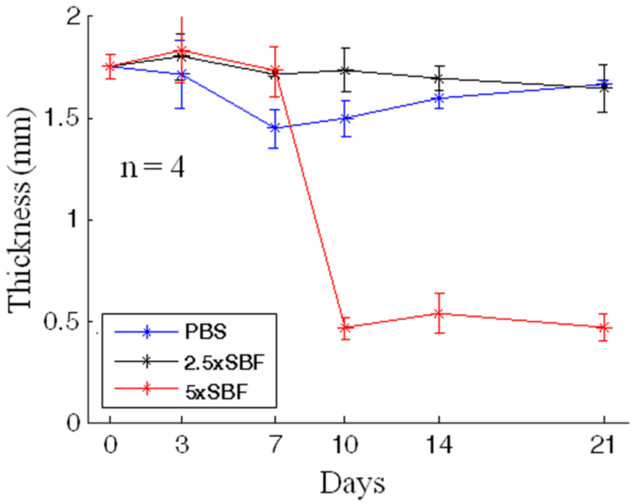

Figure 3.9 Plot of thickness over time of constructs incubated in PBS, 2.5X SBF, or 5X SBF.

was initiated at the construct surface as early as day 3, and then extended progressively into the interior of the construct. Ultrasound imaging also shows the morphology of the construct as a whole, and in particular the marked compaction in the z-direction that occurred between day 7 and day 10. The slope decreased over time, indicating increased particle size, as would be expected for a mineral deposition process.

Thresholding on ultrasound images was used to automatically determine construct thickness, by averaging the values in a 5.0 mm × 0.5 mm section. This method takes into account changes in construct shape, and therefore can provide an accurate measure of the relevant dimensions at any specific location and time. Figure 3.9 [1] shows that constructs in PBS compacted 17.4 ± 6.2 % (n = 4, $p<0.05$) over the first week but recovered over time at days 14 and 21. Constructs in 2.5X SBF did not compact significantly (1.8±2.8 % at day 7 with $p = 0.35$) over 21 days of incubation and had similar thickness as the constructs in PBS at day 21. Constructs in 5X SBF compacted markedly to less than a third of their original thickness (1.75 ± 0.06 mm, n = 4 with $p<0.001$) after day 7, and their dimensions remained relatively constant for

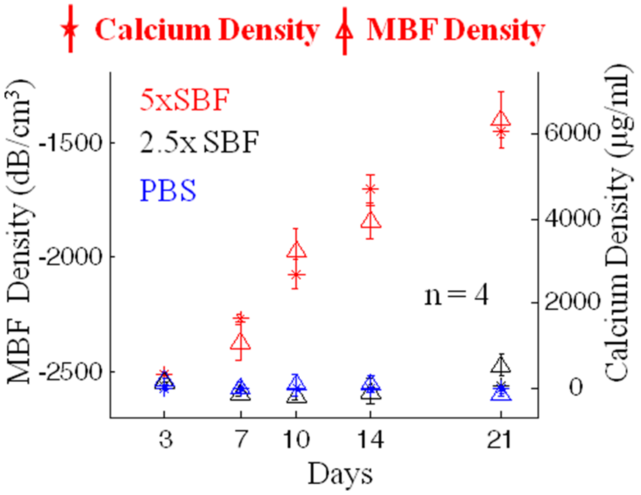

Figure 3.10 Calcium density and calculated MBF density over time in constructs incubated in PBS, 2.5X SBF, and 5X SBF.

the remainder of the incubation period.

The density of the MBF signal over a 0.5 mm x 5.0 mm x thickness volume of each construct determined was compared with the extent of mineral deposition as measured by calcium content using the OCPC assay. Figure 3.10 [1] shows both MBF density and calcium density in constructs over time. Overall, the MBF density matched the measured calcium concentration very closely in all constructs (R^2>0.95 in all cases). In PBS, there was essentially no exogenous mineral deposition and the calcium concentration remained below 2 µg/mL. In 2.5X SBF the calcium content remained low and statistically unchanged over the first 14 days of incubation, but then climbed to ~35 µg/mL by day 21, with a corresponding increase in MBF density. The 5X SBF constructs were robustly mineralized and the calcium content increased linearly over the incubation period to a final value above 6000 µg/mL at day 21.

3.3 Discussion

Spectral ultrasound imaging rapidly generated objective and quantitative information about the morphology and composition of 3D collagen constructs. Importantly, the imaging method was noninvasive and could be performed while constructs remained bathed in incubating medium. Since the assay was non-destructive, the same samples could be imaged over time to monitor their development. In addition, 3D imaging allowed sub-volume analysis and comparison of different regions of the imaged constructs through simple processing of the digital data. The use of high frequency ultrasound imaging (≈50 MHz) provided a spatial resolution of approximately 25 µm, which is suitable for characterization of engineered tissue constructs. High frequency imaging resulted in a lower penetration depth than other modalities, but still allowed characterization of the 2 mm thick engineered constructs used in this study. We imaged volumes on the order of 0.5 cm^3, but larger volumes can easily be imaged by increasing the lateral scan dimension. Importantly, the wide bandwidth available at higher frequencies is beneficial for spectral analysis because it provides richer information about the composition of the constructs, relative to conventional gray scale imaging. Taken together, these features make ultrasound imaging very attractive for biomaterials and tissue engineering research, and potentially for quality assurance purposes as engineered tissues approach the market.

In this study, we focused on mineral-containing materials because of our interest in developing mineralized orthopaedic tissues [6, 7]. Analysis of 3D collagen gels supplemented with different types of hydroxyapatite showed that spectral ultrasound can characterize the concentration, degree of dispersion, and spatial location of the mineral phase in 3D. In particular, 3D ultrasound imaging showed clearly the ability of sonication to enhance dispersion of the larger HA-R particles as well as the much smaller HA-M and HA-N particles. Mineral distribution was best analyzed using the GS and MBF parameters, since both depend primarily on the concentration of scatterers in the sample. The settling and dispersion effects could be assessed by color-coding the parametric images, and could be further quantitatively characterized using histogram analysis. In addition, the relative concentration of samples supplemented with different levels of HA were characterized using ultrasound imaging results, which correlated well with the initial loading level. Achieving good dispersion of hydroxyapatite particles throughout scaffolds and hydrogels is a well-studied problem in developing biomimetic matrices [8], and assessment of dispersion has been a challenge. Our results show that ultrasound imaging has the ability to both qualitatively and quantitatively characterize dispersion in 3D samples, and can be used to compare treatments designed to enhance dispersion.

In the analysis of HA distribution, the GS and MBF data provided similar information. However a key distinction between these parameters is that MBF is independent of both the imaging system used and the scanning power of the ultrasound probe, whereas the GS data is dependent on these factors. Therefore MBF data generated by different users on different systems is comparable, whereas GS data is not. This is an important advantage, since the ability to generate objective and instrument-independent data makes the method more broadly applicable and appropriate for inter-study comparisons.

The slope parameter is reflective of particle size. In this study, the slope parameter was able to differentiate between HA-R particles (590 µm diameter) and the smaller HA-M (5 µm) and HA-N (<200 nm) particles. However the smaller particle sizes could not be differentiated from each other because of the resolution of the probe used (approximately 25 µm). While the MBF parameter varied with added HA content as the concentration increased, the slope parameter remained relatively constant, as would be expected from adding more particles of the same size. The slope parameter is extracted from the RF spectrum and therefore is also instrument-independent.

Simulated body fluid (SBF) was used as way to exogenously mineralize 3D collagen matrices, to observe and characterize the evolution of a mineral phase in constructs over time. SBF treatment has been developed and validated as a method to deposit a bone-like apatite mineral coating throughout scaffolds and hydrogels [9, 10]. Ultrasound imaging revealed the pattern, degree and temporal progression of mineral deposition. There was a clear dose-dependent effect of SBF concentration on mineral development, which was initiated at the surface of the constructs. In the most concentrated SBF solution (5X), the formation of a mineral "shell" around the construct was followed by a dramatic compaction of the material after a week of incubation. Both the mineralization and the compaction processes were tracked over time using ultrasound imaging, which are not possible using current histological techniques. The spectral parameters were used to quantify the degree of mineral deposition and these results correlated well with corresponding data from a destructive calcium quantification assay. The reason for the marked volume change in highly mineralized constructs is not clear, but may be due to changes in osmotic pressures caused by the mineral shell or the weight of the mineral deposits.

3.4 Conclusions

This study showed that high resolution spectral ultrasound can be used to noninvasively characterize and monitor 3D protein-based constructs that contain a mineral component. The technique provided information about the dimensions and morphology of the construct as a whole, as well as the concentration, distribution, and particle size of the mineral phase. Furthermore, constructs could be imaged over time to monitor development of a mineral phase and characterize the composition of the matrix. Spectral analysis is particularly useful because it generates instrument-independent parameters that can be compared between laboratories, studies, and time points. This and similar techniques can generate metrics that reflect material and sample properties, and therefore may have utility in advancing research and product development in tissue engineering.

3.5 References

[1] M. Gudur, R. R. Rao, Y. S. Hsiao, A. W. Peterson, C. X. Deng, and J. P. Stegemann, "Noninvasive, Quantitative, Spatiotemporal Characterization of Mineralization in Three-Dimensional Collagen Hydrogels Using High-Resolution Spectral Ultrasound Imaging," *Tissue Engineering Part C-Methods*, vol. 18, pp. 935-946, Dec 2012.

[2] C. L. Cummings, D. Gawlitta, R. M. Nerem, and J. P. Stegemann, "Properties of engineered vascular constructs made from collagen, fibrin, and collagen–fibrin mixtures," *Biomaterials*, vol. 25, pp. 3699-3706, 2004.

[3] R. R. Rao, J. He, and J. K. Leach, "Biomineralized composite substrates increase gene expression with nonviral delivery," *Journal of Biomedical Materials Research Part A*, vol. 94, pp. 344-354, 2010.

[4] L. Wang and J. P. Stegemann, "Thermogelling chitosan and collagen composite hydrogels initiated with β-glycerophosphate for bone tissue engineering," *Biomaterials*, vol. 31, pp. 3976-3985, 2010.

[5] I. Hofmann, L. Muller, P. Greil, and F. A. Muller, "Precipitation of carbonated calcium phosphate powders from a highly supersaturated SBF solution," *Bioceramics, Vol 19, Pts 1 and 2*, vol. 330-332, pp. 59-62, 2007.

[6] L. M. Wang and J. P. Stegemann, "Thermogelling chitosan and collagen composite hydrogels initiated with beta-glycerophosphate for bone tissue engineering," *Biomaterials*, vol. 31, pp. 3976-3985, May 2010.

[7] A. W. Lund, J. A. Bush, G. E. Plopper, and J. P. Stegemann, "Osteogenic differentiation of mesenchymal stem cells in defined protein beads," *Journal of Biomedical Materials Research Part B-Applied Biomaterials*, vol. 87B, pp. 213-221, Oct 2008.

[8] M. Supova, "Problem of hydroxyapatite dispersion in polymer matrices: a review," *Journal of Materials Science-Materials in Medicine*, vol. 20, pp. 1201-1213, Jun 2009.

[9] K. Gkioni, S. C. G. Leeuwenburgh, T. E. L. Douglas, A. G. Mikos, and J. A. Jansen, "Mineralization of hydrogels for bone regeneration," *Tissue Engineering Part B-Reviews*, vol. 16, pp. 577-585, Dec 2010.

[10] J. D. Kretlow and A. G. Mikos, "Review: Mineralization of synthetic polymer scaffolds for bone tissue engineering," *Tissue Engineering*, vol. 13, pp. 927-938, May 2007.

CHAPTER 4

Characterization of MC3T3 Differentiation Process

Monitoring the development of tissue engineered products in a non-destructive method to ensure its quality assists the product transition from lab to clinic. In this study, high resolution spectral ultrasound imaging (SUSI) was used to identify the differentiation process of MC3T3 pre-osteoblasts and quantify the calcium mineral deposition in the construct by the differentiated cells.

4.1 Introduction

Improved imaging modalities in the evaluation of tissue engineered construct is necessary to translate the lab product into clinic. Bone tissue engineering approaches combine cells, biomaterials, and growth factors to recreate native bone tissue [Langer R, 1993]. Traditionally, biochemical and histological assays are performed in order to monitor cell function and development in these engineered tissues. However, these techniques require sample processing and are destructive in nature. These analysis modalities can only describe general characteristics of the sample rather than three dimensional (3D) spatial information. Further, these methods do not allow for one individual sample to be tracked as it progresses due to their destructive nature. Non-destructive imaging and characterization modalities, such as high-resolution ultrasound, could aid in the translation of engineered tissues towards clinical use if they could provide spatial and temporal information of constructs as they develop *in vitro*.

Although non-destructive approach based on confocal microscopic imaging to count cell nuclei has been used to provide 3D assessment of cells [1], such techniques require high quality microscopy images, and are time consuming involving sophisticated procedures to acquire the entire spatially registered 3D microscopy images of the construct. Magnetic resonance imaging (MRI) and micro-computed tomography (μ-CT) techniques have been used to estimate bone mineral densities [2, 3]. However, these methods require usage of calibration phantoms and long data acquisition times [4]. Long exposures to X-ray may affect the cell-seeded constructs in terms of the nature, viability, and cellular development of the constructs. Conventional MRI imaging systems do not provide the ability to study the microstructural details of the constructs due to their low resolution. Even with these limitations, non-destructive imaging and characterization modalities are capable of providing both spatial and temporal information of engineered tissue constructs as they develop *in vitro* and could greatly facilitate the translation of these products from lab to clinic.

Ultrasound imaging is a well-known non-invasive and non-destructive method, which may provide a potential means for quantitative evaluation of tissue development both *in vitro* and *in vivo*. It has been reported recently that ultrasound can be used to quantify the number of cells in BMSC/β-TCP composites using a grayscale equivalent parameter [5]. Fite et al. utilized an ultrasound method to monitor the chondrogenic differentiation of equine adipose stem cells in 3D poly(lactide-co-glycolide) scaffolds [6] by correlating signal attenuation measured through gray scale image analysis to extracellular matrix (ECM) deposition, which was considered to be a marker of cell differentiation. Kreitz et al. tracked collagen deposition by myofibroblasts in fibrin tissue constructs over an 18 day culture period [7]. Their quantitative analysis of observed gray scale values were correlated to ECM deposition as measured by hydroxyproline content. Ultrasound has also been used as a tool to measure the mechanical properties of agarose hydrogels as they develop over time [8]. The authors correlated material properties such as elastic modulus with obtained acoustic properties.

Since ultrasound propagation and acoustic scattering in tissue volume depend upon tissue microstructure, composition, and physical properties such as density and compressibility, the backscattered ultrasound signals may be used to extract information of the structure and composition of the tissue under investigation, as well as its mechanical and physical properties. Although tissue properties such as speed of sound, acoustic attenuation and the tissue volume can be calculated directly from the backscattered radiofrequency (RF) data, tissue microstructural details are not apparent from the raw RF signals. Tunis *et al.* [9] studied the envelope statistics of ultrasound backscatter signals from cisplatin-treated aggregated acute myeloid leukemia (AML) cells and evaluated the applicability of various statistical distribution functions to model the envelope histograms. They reported that shape parameters of the generalized gamma distribution function were sensitive to the structural changes within cells induced by the drug.

Quantitative ultrasound imaging methods using spectral analysis of the RF signals have been developed to extract such information for tissue characterization. The power spectrum of the tissue backscattered RF data includes information of tissue microstructure and the spectral regression parameters are used to relate to scatterer properties such as effective sizes, concentrations and acoustic impedances of tissue scatterers [10, 11]. Spectral slope was shown to depend upon the scatterer size whereas mid-band fit (MBF) depend on size, concentration and relative acoustic impedances of scattering elements [10].

The technique of spectral analysis has been used in various applications, including characterization of plaque composition by intravascular ultrasound (IVUS) [12, 13], lesions induced by high intensity focused ultrasound (HIFU) [14, 15] and RF ablation [16]. Spectral parameters have also proven to identify changes in tissue state for prostate, breast, pancreas, lymph nodes, and other cancer tissues [17-23]. Oelze *et al*. [18] also developed method to differentiate and characterize rat mammary fibroadenomas and 4T1 mouse carcinomas by estimating scatterer properties from backscatter RF signals in the spectral domain with a Gaussian form factor model [24].

In particular, the use of high frequency (20 – 60 MHz) ultrasound imaging has provided high spatial resolution than conventional ultrasound imaging (5 – 15 MHz) in diagnostic radiology [19]. Kolios *et al.* have shown spectral analysis technique to analyze the properties of cell ensembles or aggregates, which were used as simplified models of tumors [19, 25], to detect cellular changes with high spatial resolution and sensitivity due to exposure to chemotherapy drug treatments [26]. They found that ultrasound backscatter intensity and spectral slope increased because of treatment and that was interpreted as a consequence of the decrease in effective scatterer size of cell aggregates, Here the higher ultrasound frequency imaging, with corresponding ultrasound wavelengths in the order of 100 μm, permitted sensing of changes in cell nuclei and cell structure.

Thus, to provide non-invasive and quantitative assessment of engineered tissue constructs with high spatial resolution, we have implemented a spectral ultrasound imaging (SUSI) technique to characterize composition and structure characteristics of tissue engineered constructs. Recently we have utilized the spectral MBF and slope parameters to characterize the quantity and spatial distribution of particulate hydroxyapatite in acellular collagen hydrogels [27]. We observed a strong correlation between MBF and mineral concentration and between the slope and particle size. The amount of mineral deposited from the simulated body fluid on the acellular collagen constructs over development period of 3 weeks was also studied using spectral parameters and showed strong correlation with MBF.

The current work extended our initial results using high resolution SUSI to study the osteogenic differentiation of MC3T3 mouse pre-osteoblast cells seeded within collagen hydrogels. MC3T3 cells are a well characterized mineralizing cell type that can be induced towards the osteogenic lineage with the addition of pre-determined chemicals in the culture media [28]. Collagen is a widely used biomaterial due to its ability to support cell attachment and proliferation as well as serve as an osteoconductive and osteoinductive material [29]. Bulk properties such as speed of sound, acoustic attenuation and volume compaction of the constructs were quantified and tracked over time. Microstructural properties such as cell size, cell number, and cell differentiation of the MC3T3 seeded constructs were characterized using spectral ultrasound and are compared to traditional biochemical assays and confocal images. The results from this study are in the process of submission to a journal with the title, “Non-invasive Quantification of In-vitro Osteoblastic Differentiation in 3D Engineered Tissue Constructs using Spectral Ultrasound Imaging”.

4.2 Materials and Methods

The tissue constructs were manufactured in Cell-Matrix Interactions & Tissue Engineering (CMITE) lab, Department of Biomedical Engineering.

4.2.1 Cell Culture

Mouse pre-osteoblast MC3T3-E1 were cultured in α-MEM without ascorbic acid (Life Technologies, Grand Island, NY) supplemented with 10% fetal bovine serum (FBS; Life Technologies) and 1% penicillin and streptomycin (PS: Life Technologies) and used at passage 8. Media was changed every other day.

4.2.2 Collagen Hydrogel Synthesis

Three-dimensional (3D) collagen hydrogels were created as previously described [Gudur MS, 2012]. Collagen type I (MP Biomedicals, Solon, OH) was prepared at 4.0 mg/ml in 0.02 N acetic acid. Collagen hydrogels (2.0 mg/ml final concentration) were formed by mixing 10% Dulbecco's modified Eagle's medium (DMEM; Life Technologies), 10% FBS, 20% 5X-concentrated DMEM, 10% 0.1 N NaOH (Sigma Aldrich, St. Louis, MO), and 50% collagen stock solution. 500 μL of the mixture was then pipetted into a 24-well plate and allowed to gel for 30 mins at 37°C. Cells were encapsulated within the hydrogels at the time of gelation at a concentration of 1.0 x 10^6 cells/ml.

After gelation, hydrogels were placed in a 6-well culture plate containing α-MEM supplemented with 10% FBS and 1% PS. After 24 hours, the media was changed with either a control media or osteogenic media containing 10 μM beta-glycero phosphate (β-GP; Sigma) and 5 μg/ml ascorbic acid (Sigma).

4.2.3 Cell Viability

Cell viability was visualized and quantified as previously described [Rao RR, 2012]. At days 1 and 21, cell-seeded hydrogels were washed 3X in phosphate buffered saline (PBS; Life Technologies) for 5 mins and then incubated in 4 μM calcein-AM (EMD Millipore, Billerica, MA) and 4 μM ethidium homodimer-1 (Sigma) in PBS for 45 mins. Constructs were washed 3X in PBS prior to imaging on a Nikon A1 Confocal Microscope (Nikon Instruments, Melville, NY). Cell viability was quantified using ImageJ software (National Institute of Health, Bethesda, MD).

4.2.4 Fluorescence Staining

At days 1 and 21, cells were stained for their actin cytoskeleton and nuclei. Hydrogels were washed 2X in PBS for 5 mins/wash and then fixed in zinc-buffered formalin (Z-Fix; Battle Creek, MI) for 10 mins at 4°C. Gels were washed another 2X in PBS and then permeabilized using 0.5% Triton-X 100 (Sigma) in PBS for 20 mins at room temperature. Constructs were washed again 2X, and then incubated in a solution containing 165 nM AlexaFluor 488 phalloidin (Life Technologies) and 10 nM fluorescent DAPI (Life Technologies) in 1% bovine serum albumin (BSA; Sigma) in PBS for 45 mins. Hydrogels were washed again prior to imaging.

4.2.5 Biochemical Assays

Cellular DNA content and calcium were quantified as previously described [Rao RR, 2013]. For DNA quantification, hydrogels were collected and degraded overnight in 10 mM Tris-HCl (Sigma) containing 0.6 mg/mL collagenase type I (MP Biomedicals), 0.2% IGEPAL (Sigma), and 2 mM phenylmethanesulfonylfluoride (Sigma). DNA was then measured using the PicoGreen DNA assay (Life Technologies). Calcium secretion from the cells was assays using an ortho-cresolphthalein (OCPC) method on the lysate.

4.2.6 Ultrasound Imaging and Backscattered Signal Acquisition

Figure 4.1 shows a schematic diagram of the imaging setup that includes a 60 mm diameter Petri dish lined with 8% agarose (Lonza) at the bottom to reduce the ultrasound reflection from the bottom of the dish. The dish was then filled with α-MEM at room temperature and the constructs were placed on top of the agarose gel pad. Ultrasound imaging was performed with a Vevo 770 (VisualSonics Inc., Toronto, Canada) using an RMV 708 imaging probe with a nominal 55 MHz center frequency, 20-75 MHz bandwidth (−6 dB), 4.5 mm focal distance, and 1.5 mm depth of focus (−6 dB). For the tissue construct composition estimation, 3D backscattered RF data with ultrasound focus on the tissue construct were collected at 100% scanner power for cell differentiation study and 50% or 100% for cell concentration study at 420 MS/s sampling rate by performing multiple B-mode scans using an automatic 3D translational controller. The interval between adjacent A-lines and B-mode scans were 31 μm and 200 μm, respectively. For estimating the speed of sound and acoustic attenuation of the construct, 2D backscattered RF data with ultrasound focus at the gel pad surface were collected at 20% scanner power along with a reference RF acquisition of the setup without the construct. Apart from the RF data, 3D image data with separation between adjacent A-lines and B-mode scans of 31 μm and 100 μm respectively, was also collected to visualize 3D rendered images and to estimate the volume of the construct.

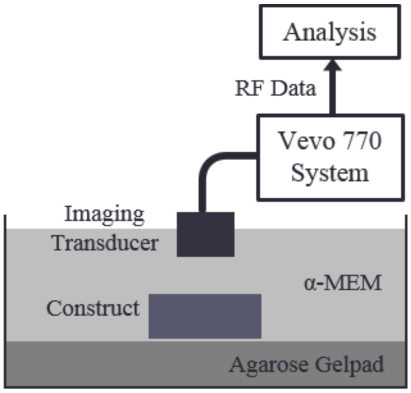

Figure 4.1 Schematic of experimental setup used for spectral ultrasound imaging of tissue construct.

4.2.7 Ultrasound Backscattered Signal Analysis

4.2.7.1 Volume: Volume of the construct was estimated by a semi-automated segmentation procedure on Vevo 770 system, in which an edge detection algorithm detects the contour of the construct in a frame. Subsequent contours in adjacent frames are drawn semi-automatically until the contours in all frames are drawn, thus calculating the volume of the gel within the contoured region.

4.2.7.2 Speed of Sound: Grayscale parameter [27] is computed from 2D RF data. The time of travel of the ultrasound pulse to the construct's top surface $\left(t_{top}\right)$, bottom surface $\left(t_{bottom}\right)$ and to the agar gel pad $\left(t_{pad}^{construct}\right)$ was determined based on grayscale thresholding using an automated algorithm. The time of travel to the agar gel pad without the construct $\left(t_{pad}^{ref}\right)$ was also determined as the reference. Using the known sound speed in the surrounding fluid medium $\left(C_f\right)$, the thickness of the construct (*L*) and speed of sound in the tissue construct $\left(C_{tc}\right)$ was determined as:

$$L = 0.5\, C_f \left[\left(t_{bottom} - t_{top}\right) + \left(t_{pad}^{ref} - t_{pad}^{construct}\right)\right] \tag{4.1}$$

$$C_{tc} = \frac{2L}{t_{bottom} - t_{top}} \tag{4.2}$$

4.2.7.3 Attenuation: Frequency dependent attenuation in dB/cm was calculated as:

$$\alpha(f)_{tc} = \frac{20}{2L} \log_{10} \frac{\left|A(f)\right|}{\left|A_0(f)\right|} \tag{4.3}$$

where $|A(f)|$ and $|A_0(f)|$ are the spectral magnitudes of RF signal at the gel pad surface with and without (reference) the construct respectively. The slope of α against f estimated by a linear fit between 20-55 MHz provides attenuation in dB/(cm-MHz).

4.2.8 SUSI Analysis

4.2.8.1 Scatterer Size and Concentration: By the method described in Chapter 2 on estimating the scatterer size and concentration from the spectral parameters, MC3t3 cell size and cell concentration are estimated at various time points of cell development. To estimate concentration for samples until day 14, when there is no calcium deposition, a relative acoustic impedance, Q, value for MC3t3 cells was used from the Q value obtained from MC3t3 cell concentration study.

4.2.8.2 Cell deposited calcium: MC3T3 differentiation process can be identified by detecting and quantifying the mass of the calcium deposited in the construct by the differentiated MC3T3 cells. On day 21, the presence of deposited calcium around the cell will increase relative acoustic impedance of the net scatterer. With known relative acoustic impedance of the scatterer on day 14 (cell alone) and day 21 (cell and calcium), mass of the calcium can be calculated. The relative acoustic impedance is

$$Q = \frac{\rho c - \rho_0 c_0}{\rho_0 c_0} \tag{4.4}$$

where ρ and ρ_0 are the densities of the scatterer and ECM, c and c_0 are the speed of sound in the scatterer and ECM respectively. Solving for the total mass of calcium (derivation shown in Appendix)

$$M_{cal} = C_{21} V_{14} \frac{\rho_0 c_0}{c_{14}} \left(Q_{21} - Q_{14} \right) \tag{4.5}$$

where V_{14} is the volume of the scatterer on day 14 and is approximately $\frac{4}{3}\pi a^3$

4.2.9 Parametric Images

The spatial distribution of scatterer features of the construct on the GS B-mode images were represented by marking each pixel within the construct with a color that corresponds to the values of the scatterer size and concentration.

4.2.10 Statistical Analysis

Analysis was carried out on a 0.6 mm x 5.0 mm x thickness (~1 mm) volume of each construct and the data are presented as mean ± standard deviation. Statistical comparisons between any two parameters were made using Student's t-test for paired samples and the differences were considered significant at a level of $p<0.05$.

4.3 Results

4.3.1 MC3t3 Relative Acoustic Impedance

To estimate the number concentration, C, of the scatterers from SUSI analysis, their relative acoustic impedance needs to be determined. An experiment with MC3t3 cell constructs at four different known concentrations, 0.5, 1, 2 and 5×10^6 cells/ml on day 0 was carried out to perform SUSI analysis and estimate cell diameter and cell acoustic concentration. The ultrasound B-mode images of these constructs are shown in Figure 4.2A-D. Constructs with known concentration of cells at 2×10^6 cells/ml was used to estimate the relative acoustic impedance of the MC3T3 cells from SUSI analysis. Then the estimated relative acoustic impedance was used to estimate the cell concentration of cells in the other constructs with different cell concentration (0.5, 1 and 5×10^6 cells/ml) at day 0. Using SUSI analysis, the estimated cell diameter was approximately 14 ± 1.5 µm (n = 9) and decreased slightly with increased cell concentration (Figure 4.2E), likely due to compacting of the constructs with higher cell concentration. The relative acoustic impedance of the MC3T3 cell was estimated to be 0.6. A linear fit of the

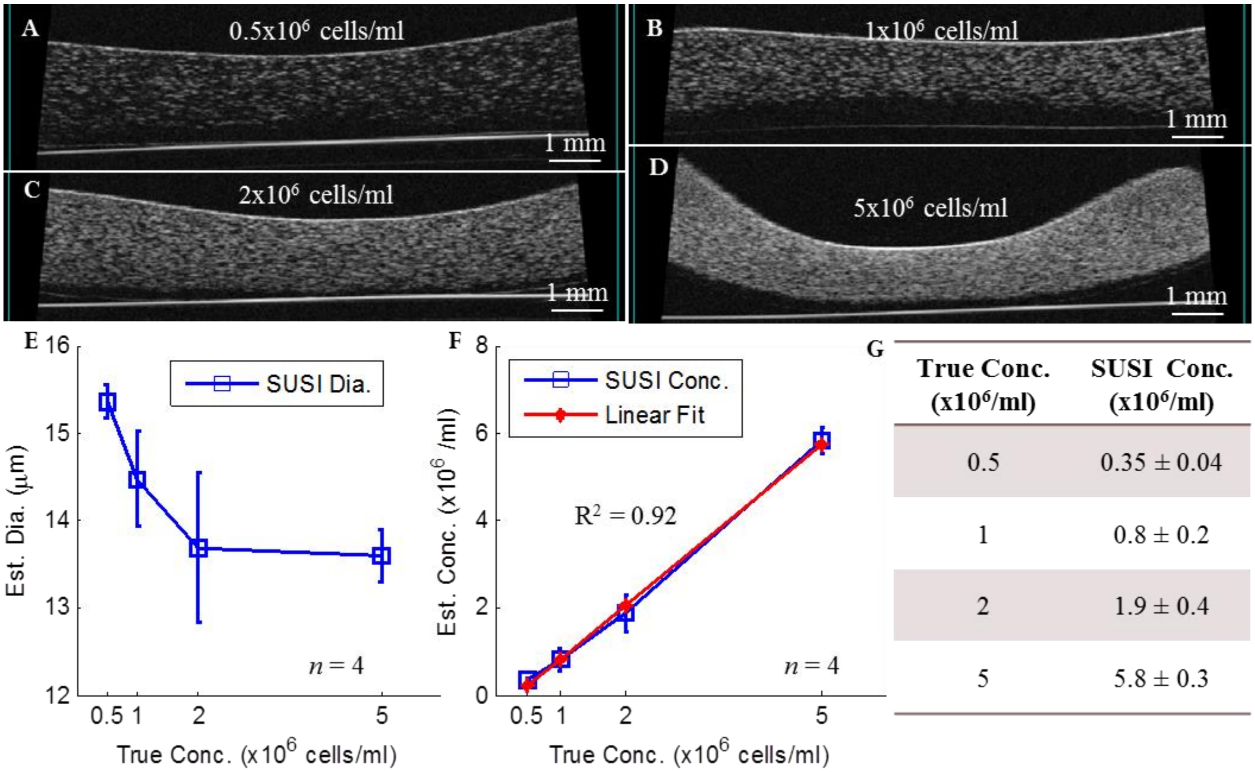

True Conc. (x10⁶/ml)	SUSI Conc. (x10⁶/ml)
0.5	0.35 ± 0.04
1	0.8 ± 0.2
2	1.9 ± 0.4
5	5.8 ± 0.3

Figure 4.2 (A)-(D) Ultrasound B-mode images of MC3t3 cell constructs on Day 0 at 0.5, 1, 2 and 5 x10^6 cells/ml cell concentrations respectively. (E) Cell diameter and (F) Cell concentration estimated from SUSI analysis w.r.t true cell concentration (G) Tabular values of true and estimated cell concentrations.

estimated concentration against the true concentration (R^2 = 0.92) (Figure 4.2F) confirm the ability of SUSI for detecting cell concentration. With the estimated relative acoustic impedance of the MC3t3 constructs, estimation of MC3t3 cell concentration to assess the process of cell proliferation/apoptosis and cell differentiation will be feasible.

4.3.2 Ultrasound Histology

Imaging using the Vevo 770 system at 55 MHz achieved rapid and non-invasive 3D ultrasound imaging of MC3T3 collagen constructs. During ultrasound imaging, the constructs in α–MEM media were outside of the incubator for less than 20 minutes. The 3D rendered ultrasound images and the brighfield images of the constructs in control and osteogenic media at time-points day 1, 7, 14 and 21 are shown in Figure 4.3. It clearly show that the constructs in both control and osteogenic media adopt a symmetrical bowl-like shape from day 1, which could be due to the meniscus formation during preparation of the gels. Compaction of the constructs was evident for both constructs in control and osteogenic medium. In addition, the constructs in osteogenic medium became more echogenic than those in control medium, indicating changes occurring during development in osteogenic medium. The constructs in both control and osteogenic media has drop in volumes over time, which is quantitatively measured and shown in Figure 4.4A. There is no significant difference between the drop in volumes between control and

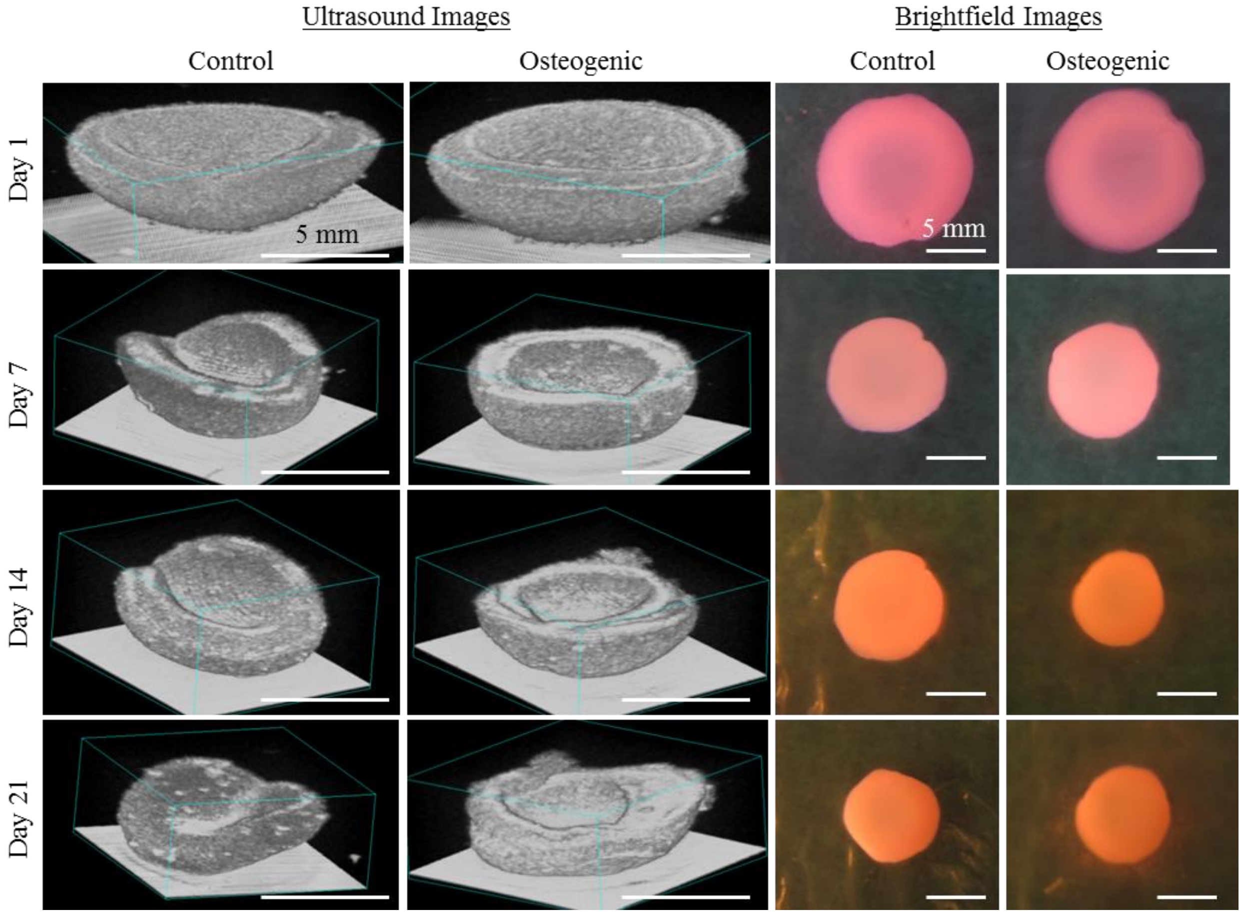

Figure 4.3 3D rendered ultrasound backscattered images of MC3t3 cell constructs in control (1st column) and osteogenic media (2nd column) on day 1, 7, 14 and 21 of the development process. Brightfield images of the same constructs are shown on the 3rd and 4th columns.

osteogenic media at any specific time-point, an indicator of growth media independent process. From day 1, drop in volume on day 7 is statistically significant and the drop is significant there onwards. Acoustic parameters such as speed of sound and acoustic attenuation were also estimated and shown in Figure 4.4B and 4.4C respectively. There is a gradual insignificant increase in speed of sound over development time for constructs in both control and osteogenic media. Attenuation increased almost linearly over development time with increase in attenuation for construct in osteogenic media on day 21 slightly more than for the construct in control media on day 21, the increase being statistically insignificant. Attenuation estimation will be used to compensate for the construct attenuation in estimating the correct spectral parameters. Volume and speed of sound will be used to determine the amount of calcium deposited by the differentiated cell constructs in osteogenic media.

4.3.3 Cell Viability

Cell viability in the constructs with and without ultrasound imaging was compared to assess possible effects of ultrasound imaging As shown in Figure 4.5, viability was greater than 90% at day 1 in all of the samples and greater than 70% in all samples at day 21, and there were no statistical differences between the samples with and without ultrasound imaging at either time point, indicating that exposure to ultrasound imaging did not affect cell viability.

4.3.4 Changes in Volume, Sound Speed and Acoustic Attenuation

As shown in Figure 4.5A, a significant decrease in construct volume between days 1 and 7 was observed before the construct volume remained constant between days 7 through 21. No significant difference in the volumes was detected between control and osteogenic media at any of the time-points. There was a slight increase in the speed of sound over development time for

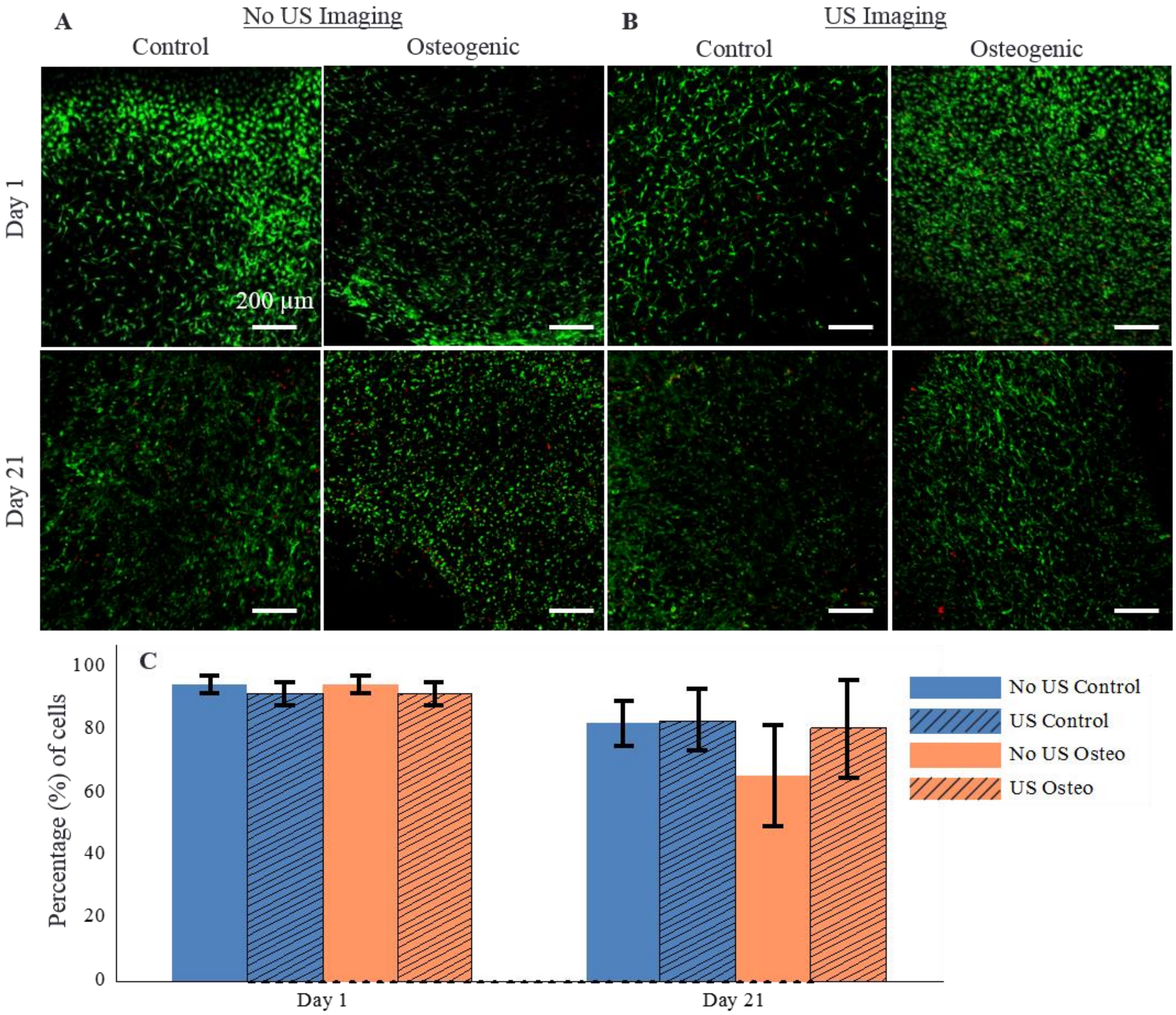

Figure 4.4 Cell viability assay on day 1 and 21 of MC3t3 constructs in control and osteogenic media. Constructs on the left half were not imaged using ultrasound in contrast to the right half. Bottom bar plot shows the percentage of cell viability calculated from the images.

constructs in both control and osteogenic media. The most significant change is the acoustic attenuation, which increased almost linearly over development time with no significant difference between constructs in control and osteogenic media. Since the acoustic attenuation is typically an indicator of increased acoustic impedance and/or scatterer concentration, this increase may indicate cell proliferation and mineral deposits.

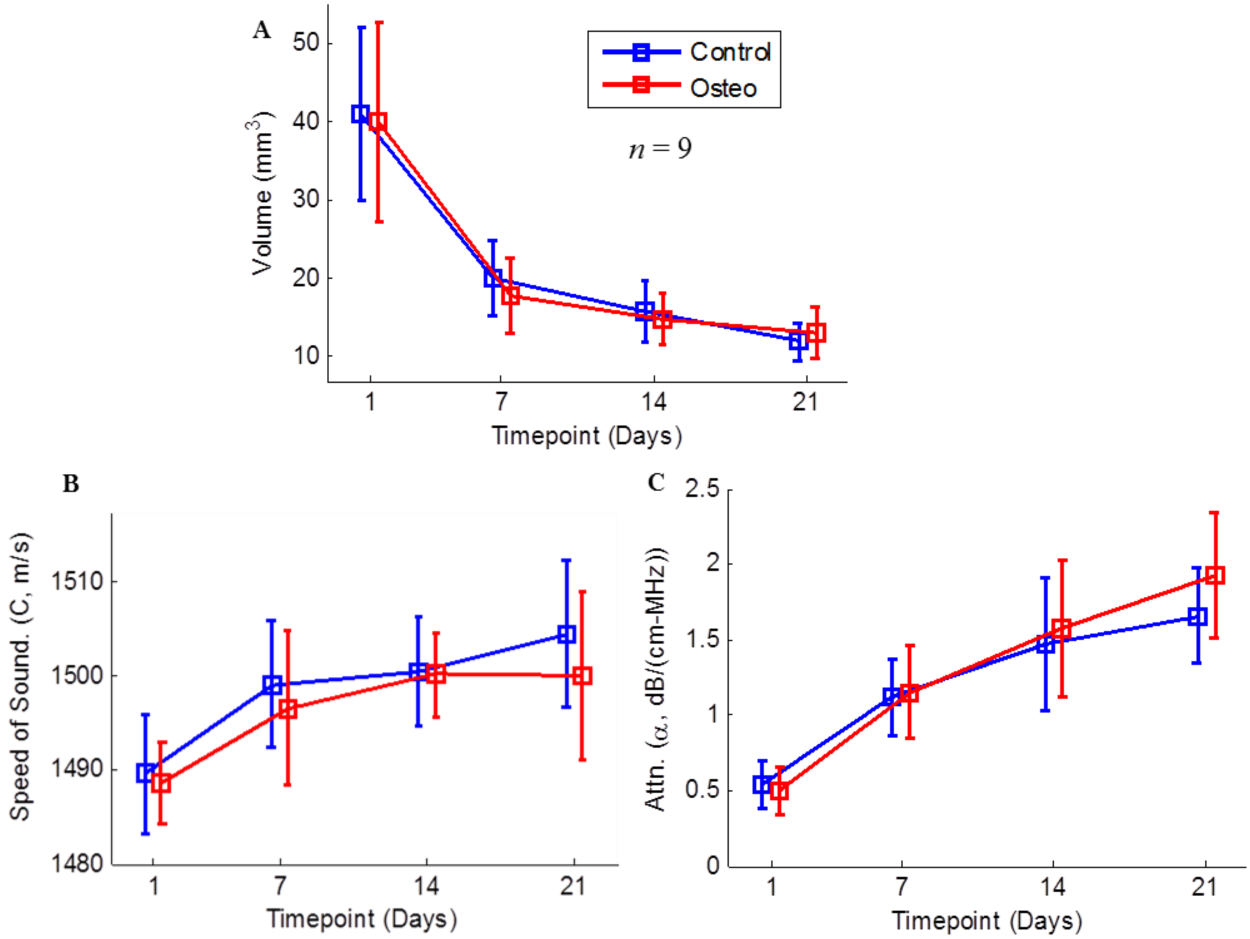

Figure 4.5 (A) Volume (B) Speed of Sound and (C) Attenuation of the MC3t3 constructs in control and osteogenic media at various time-points.

These results of construct volume, speed of sound, and acoustic attenuation were used in further analysis of the constructs including estimation of spectral parameters and calcium deposits by the differentiated cell constructs in osteogenic media.

4.3.5 Diameter

Figure 4.6A-4.6D shows the seeded MC3T3 cells in the collagen hydrogels with the F-actin filaments stained in green and cell nuclei stained in blue at 40x microscopic view. From these images, diameters of the cell nuclei were estimated using a customized MATLAB script to be 6 ± 1 µm (*n* = 4) on day 1 and 7.6 ± 1.9 µm (*n* = 4) on day 21 and found the difference to be

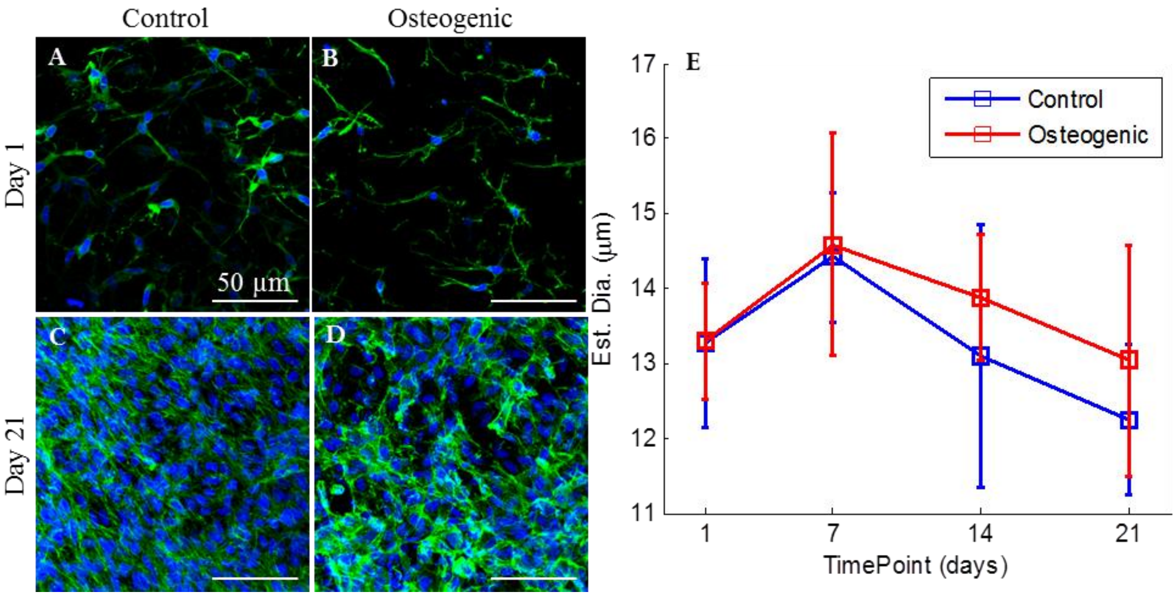

Figure 4.6 (A)-(D) Immunofluorescence staining of MC3t3 constructs in control and osteogenic media on day 1 and day 21. (E) Estimated diameter of the cell from SUSI analysis during the development time.

statistically insignificant. The effective sizes of the cells over the three week period were also estimated using the slope parameter obtained from SUSI analysis (Figure 4.6E). The average diameter for the cells, 14 ± 1.5 µm (*n* = 9) remained essentially unchanged during the three week period for constructs in both control and osteogenic media, suggesting that the cells were involved in the scattering of ultrasound, not merely cell nucleus.

4.3.6 Acoustic Concentration and Calcium Deposit in Constructs

The total amount of DNAs in a construct was measured and converted to the total number of cells by calibrating with the amount of DNAs in the construct on day 0 when the number of cells was known (0.5×10^6/construct). As shown in Figure 4.7A, the number of cells decreased by about 60% from day 1 to day 7 in constructs in both the control and osteogenic groups, indicating cell death during this period, although the number of cells remained constant from days 7 to 21 with no significant differences in either media groups. These numbers of cells correlated well with the equivalent number of acoustic scatterers, which is the acoustic concentration (CQ^2) estimated by SUSI analysis multiplied by the construct volume, except that on day 21 in the osteogenic group (Figure 4.7B). The acoustic concentration from SUSI depends on both the relative acoustic impedance of the scatterers (Q) and the actual number of scatterers (C). Thus assuming the actual number of scatterers or cells remained constant, the increased equivalent number of acoustic scatterers (or increased acoustic concentration) can be attributed to an increase of the relative acoustic impedance of the scatterers during the last days of incubation of the constructs (Figure 4.7C). The significantly increased acoustic impedance on day 21 indicates the changes due to the differentiation process in the constructs. Since acoustic

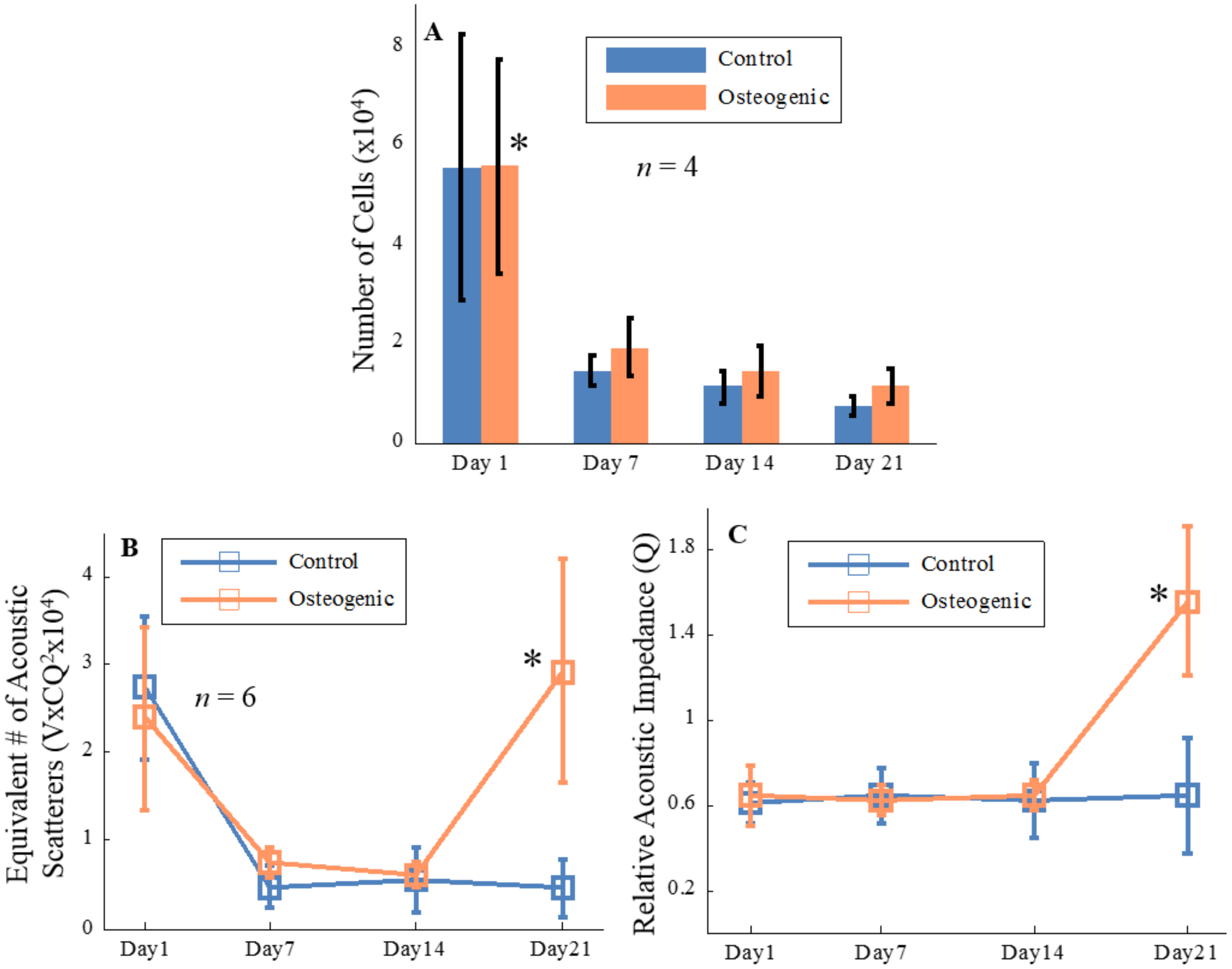

Figure 4.7 Total number of cells derived from the DNA quantification of MC3T3-seeded collagen constructs in control and osteogenic media during the development time. (B) Total number of acoustic scatterers estimate from SUSI analysis. (C) Relative acoustic impedance estimated from (A) and (B).

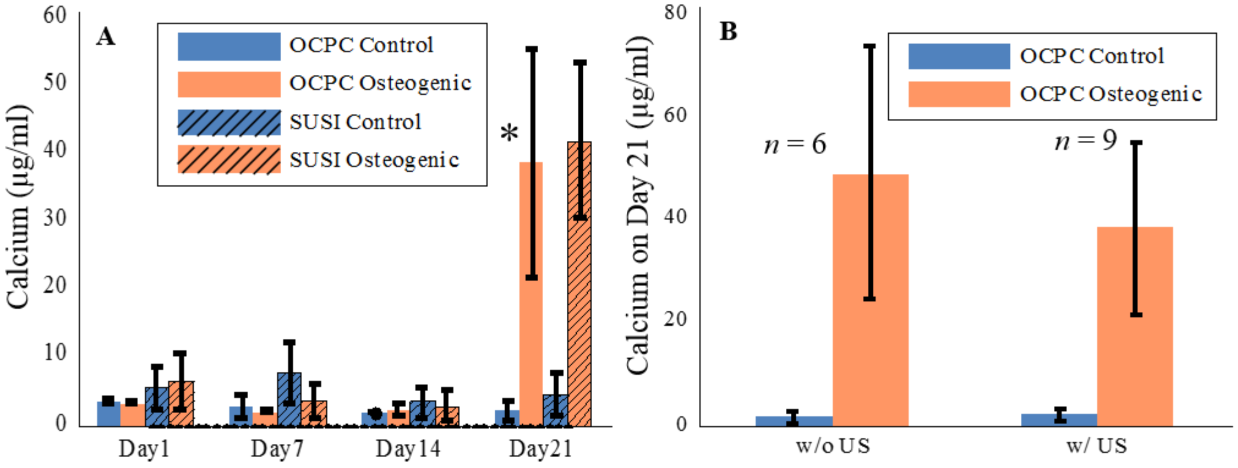

Figure 4.8 (A) Calcium content from OCPC method and SUSI estimate (B) Calcium assay on MC3T3-seeded collagen constructs in control and osteogenic media with and without exposure to ultrasound imaging.

impedance depends on mass density and speed of sound of scatterers, the increased acoustic impedance implies possibly an increase of mass density due to calcium deposits associated with the cell differentiation. As calcium is much denser than water, its presence is expected to significantly increase the relative acoustic impedance of the scatterers.

As a quantitative marker to identify the extent of osteogenic differentiation of seeded MC3T3 cells [30], we estimated the calcium content using standard assays (OCPC method) and SUSI. The estimated calcium concentration from SUSI on day 21 was 41.7 ± 11.4 µg/ml (*n* = 9) and was comparable with the measured values of 38.7 ± 16.7 µg/ml (*n* = 10) from OCPC method. No statistically significant difference in the calcium deposition at day 21 was detected in constructs subjected to ultrasound imaging and those without ultrasound imaging performed (Figure 4.8B).

4.3.7 Parametric Images

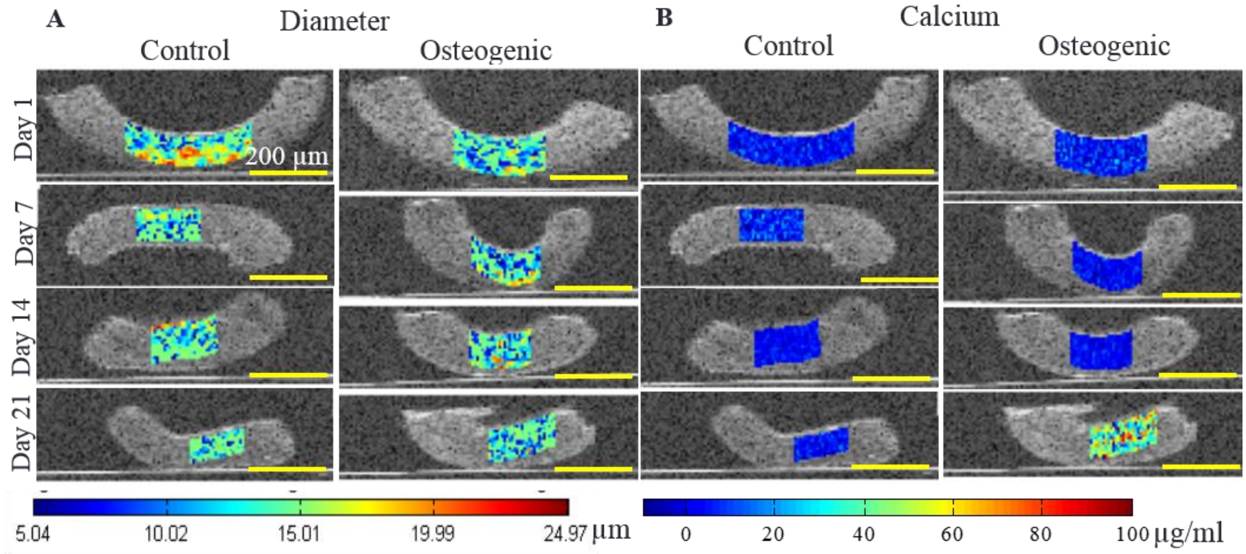

Figure 4.9 Scatterer feature estimates, diameter (left half) and calcium concentration (right half) of MC3t3 constructs in control and osteogenic media.

The estimated microstructural properties (acoustic scatterer size and secreted calcium concentration) from SUSI analysis were used to form parametric images or color coded images overlaid on B-mode images to assess the spatiotemporal evolution of constructs during development. As an example, Figure 4.9 shows the estimated microstructural parameters in a representative region of interest for constructs in control and osterogenic groups throughout the development duration. The scatterer diameter was uniform within the construct, and did not vary during the development process for constructs in either control or osteogenic medium (Figure 4.9A). The estimated calcium concentration was fairly constant at low values at all time-points, except for the constructs in osteogentic medium on day 21 that exhibited a significantly higher value, indicating the result of osteogenic differentiation of MC3T3 cells in the constructs.

4.4 Discussion

In this study, we demonstrated that high resolution ultrasound imaging provided non-destructive monitoring of the MC3T3-seeded collagen constructs over 3 weeks. Physical parameters including the volume of each individual construct, speed of sound and acoustic attenuation in the constructs were obtained from simple analysis of the ultrasound imaging signals. Notably, beyond analyses that based on conventional ultrasound images, SUSI analysis provided estimation and assessment of the microstructural characteristics of the constructs, including the cell size, acoustic concentration, changes in number of cells and mineral secretion. Since system factors are removed from SUSI analysis by calibration, the SUSI parameters provide objective and instrument-independent analysis which can be more broadly applicable and appropriate for inter-study comparisons. These features make ultrasound imaging and particularly SUSI a very attractive tool for biomaterials and tissue engineering research, as a potential means for use in quality assurance as engineered tissues approach the market. Below we discuss implications of our results and limitation of this study.

4.4.1 Morphological Changes in Tissue Constructs

Cells such as fibroblasts, smooth muscle cells, cardio myocytes or osteoblasts placed within a collagen matrix remodel the matrix by exerting substantial contractile forces [31]. These forces are significantly higher than the forces required to propel cell locomotion and it has been proposed that their main function is morphing the structure of the construct rather than to drive cell migration [32, 33]. Assessment of tissue construct morphology in 3D in a non-invasive method is important to study these changes. In this study, we showed that high resolution 3D ultrasound imaging readily identified the morphological behaviors of tissue constructs longitudinally, revealing the significant compaction of the MC3T3 constructs from day 1 to day 7 since the constructs were unconstrained in the culture plate.

4.4.2 SUSI Quantification of Microstructural Changes in Tissue Constructs

We showed that ultrasound imaging provides non-destructive monitoring without affecting the nature of the constructs. In this study, SUSI analysis revealed that the total number of cells in the unconstrained MC3T3-seeded collagen constructs decreased by approximately 80% throughout the 21 day time period. It is possible that the decrease in cell number was due to the decrease in construct volume. A similar cell death pattern was observed in a previous study of unconstrained constructs seeded with undifferentiated mesenchymal stem cells (MSC) [34].

The acoustic concentration, or CQ^2, where C is the number concentration of the scatterers and Q the acoustic impedance of the scatterers, depends on the scatterer physical and acoustic properties such as the mass density and speed of sound. Thus assessment of the total number of acoustic scatterers (CQ^2 multiplied by construct volume) can provide information regarding the changes associated with MC3T3 cells differentiation towards the osteogenic lineage. As the cells secrete mineral into the surrounding ECM [30] to modify the properties of the acoustic scatterers, most likely by increasing the mass density of the scatterers and thus its relative acoustic impedance. Hence, relative acoustic impedance can be used as an indicator of changes in cellular state during osteogenic differentiation. In the current study, we not only qualitatively identified the differentiation process via changes in the relative acoustic impedance, but also obtained quantitative values of the mass of calcium based on the relative acoustic impedance values with minor assumptions in the model. To our knowledge, this is the first study to propose an ultrasound imaging-based method to estimate the mass of calcium mineral in collagen constructs as MC3T3 cells differentiate in osteogenic medium.

4.4.3 Limitations

The current study demonstrated the advantages of high frequency ultrasound imaging for monitoring of tissue construct development. The higher frequency used here ensured high spatial resolution, which might not be fully translatable to clinical settings where lower frequency (e.g. 10 MHz) imaging is typically used for deep tissue penetration as higher frequency ultrasound suffers from higher attenuation in tissue.

Our estimation of the relative acoustic impedance in this study required knowledge of the number of cells, which may not be readily available non-destructively. Otherwise, a composite parameter, the acoustic concentration (CQ^2), which is obtained directly from SUSI analysis, can be used to assess the changes in the constructs. However, this would prevent quantitative estimation of mass of calcium in the constructs specifically. In addition, we assumed that calcium deposited by the cells was not separated from the cells to be regarded as different scatterers from the cells. Future investigation on different cell types/conditions will provide additional validation of the proposed technique.

4.5 Conclusions

In this study, high resolution spectral ultrasound imaging (SUSI) was used to identify the differentiation process of MC3T3 pre-osteoblasts and quantify the calcium mineral deposition in the construct by the differentiated cells. Cell size and concentration were estimated from SUSI to study the construct development in maintenance and osteogenic media. Volume compaction of the constructs, cell proliferation, and cell differentiation measured by calcium secretion were identified and distinguished between constructs in both media. Estimated cell diameter was 13 µm and the variation was negligible during the development process. Cell proliferation/apoptosis and nucleus size were verified by biochemical assays. The amount of calcium secreted by differentiated cells into the construct estimated using SUSI analysis was 41.7±18.1 µg/ml, matching closely with OCPC method for calcium values of 38.7±16.7 µg/ml. These data demonstrate that cell differentiation process can be quantitatively identified using non-invasive SUSI and that these techniques will assist the development of orthopedic engineered tissues.

4.6 References

[1] J. W. Han, T. P. Breckon, D. A. Randell, and G. Landini, "The application of support vector machine classification to detect cell nuclei for automated microscopy," *Machine Vision and Applications,* vol. 23, pp. 15-24, Jan 2012.

[2] K. Y. Ho, H. C. H. Hu, J. H. Keyak, P. M. Colletti, and C. M. Powers, "Measuring bone mineral density with fat-water MRI: comparison with computed tomography," *Journal of Magnetic Resonance Imaging,* vol. 37, pp. 237-242, Jan 2013.

[3] A. Nazarian, B. D. Snyder, D. Zurakowski, and R. Muller, "Quantitative micro-computed tomography: A non-invasive method to assess equivalent bone mineral density," *Bone,* vol. 43, pp. 302-311, Aug 2008.

[4] A. C. Jones, B. Milthorpe, H. Averdunk, A. Limaye, T. J. Senden, A. Sakellariou, *et al.*, "Analysis of 3D bone ingrowth into polymer scaffolds via micro-computed tomography imaging," *Biomaterials,* vol. 25, pp. 4947-4954, Sep 2004.

[5] K. Oe, M. Miwa, K. Nagamune, Y. Sakai, S. Y. Lee, T. Niikura, *et al.*, "Nondestructive evaluation of cell numbers in bone marrow stromal cell/beta-tricalcium phosphate composites using ultrasound," *Tissue Engineering Part C-Methods,* vol. 16, pp. 347-353, Jun 2010.

[6] B. Z. Fite, M. Decaris, Y. H. Sun, Y. Sun, A. Lam, C. K. L. Ho, *et al.*, "Noninvasive multimodal evaluation of bioengineered cartilage constructs combining time-resolved fluorescence and ultrasound imaging," *Tissue Engineering Part C-Methods,* vol. 17, pp. 495-504, Apr 2011.

[7] S. Kreitz, G. Dohmen, S. Hasken, T. Schmitz-Rode, P. Mela, and S. Jockenhoevel, "Nondestructive method to evaluate the collagen content of fibrin-based tissue engineered

structures via ultrasound," *Tissue Engineering Part C-Methods,* vol. 17, pp. 1021-1026, Oct 2011.

[8] J. M. Walker, A. M. Myers, M. D. Schluchter, V. M. Goldberg, A. I. Caplan, J. A. Berilla, *et al.*, "Nondestructive evaluation of hydrogel mechanical properties using ultrasound," *Annals of Biomedical Engineering,* vol. 39, pp. 2521-2530, Oct 2011.

[9] A. S. Tunis, G. J. Czarnota, A. Giles, M. D. Sherar, J. W. Hunt, and M. C. Kolios, "Monitoring structural changes in cells with high-frequency ultrasound signal statistics," *Ultrasound in Medicine and Biology,* vol. 31, pp. 1041-1049, Aug 2005.

[10] F. L. Lizzi, M. Ostromogilsky, E. J. Feleppa, M. C. Rorke, and M. M. Yaremko, "Relationship of ultrasonic spectral parameters to features of tissue microstructure," *Ieee Transactions on Ultrasonics Ferroelectrics and Frequency Control,* vol. 34, pp. 319-329, May 1987.

[11] F. L. Lizzi, M. Astor, T. Liu, C. Deng, D. J. Coleman, and R. H. Silverman, "Ultrasonic spectrum analysis for tissue assays and therapy evaluation," *International Journal of Imaging Systems and Technology,* vol. 8, pp. 3-10, 1997.

[12] A. Nair, B. D. Kuban, E. M. Tuzcu, P. Schoenhagen, S. E. Nissen, and D. G. Vince, "Coronary plaque classification with intravascular ultrasound radiofrequency data analysis," *Circulation,* vol. 106, pp. 2200-2206, Oct 22 2002.

[13] J. Qian, A. Maehara, G. S. Mintz, M. P. Margolis, A. Lerman, J. Rogers*, et al.*, "Impact of Gender and Age on In Vivo Virtual Histology-Intravascular Ultrasound Imaging Plaque Characterization (from the global Virtual Histology Intravascular Ultrasound [VH-IVUS] Registry)," *American Journal of Cardiology,* vol. 103, pp. 1210-1214, May 1 2009.

[14] M. S. R. Gudur, R. E. Kumon, Y. Zhou, and C. X. Deng, "High-Frequency Rapid B-Mode Ultrasound Imaging for Real-Time Monitoring of Lesion Formation and Gas Body Activity During High-Intensity Focused Ultrasound Ablation," *Ieee Transactions on Ultrasonics Ferroelectrics and Frequency Control,* vol. 59, pp. 1687-1699, Aug 2012.

[15] R. E. Kumon, M. S. R. Gudur, Y. Zhou, and C. X. Deng, "High-Frequency Ultrasound M-Mode Imaging for Identifying Lesion and Bubble Activity during High-Intensity Focused Ultrasound Ablation," *Ultrasound in Medicine and Biology,* vol. 38, pp. 626-641, Apr 2012.

[16] S. Siebers, M. Schwabe, U. Scheipers, C. Welp, J. Werner, and H. Ermert, "Evaluation of ultrasonic texture and spectral parameters for coagulated tissue characterization," *2004 IEEE Ultrasonics Symposium, Vols 1-3,* pp. 1804-1807, 2004.

[17] E. J. Feleppa, "Ultrasonic tissue-type imaging of the prostate: Implications for biopsy and treatment guidance," *Cancer Biomarkers,* vol. 4, pp. 201-212, 2008.

[18] M. L. Oelze, W. D. O'Brien, J. P. Blue, and J. F. Zachary, "Differentiation and characterization of rat mammary fibroadenomas and 4T1 mouse carcinomas using quantitative ultrasound imaging," *Ieee Transactions on Medical Imaging,* vol. 23, pp. 764-771, Jun 2004.

[19] R. M. Vlad, N. M. Alajez, A. Giles, M. C. Kolios, and G. J. Czarnota, "Quantitative Ultrasound Characterization of Cancer Radiotherapy Effects in Vitro," *International Journal of Radiation Oncology Biology Physics,* vol. 72, pp. 1236-1243, Nov 15 2008.

[20] F. L. Lizzi, "Ultrasonic scatterer property images of the eye and prostate," *1997 Ieee Ultrasonics Symposium Proceedings, Vols 1 & 2,* pp. 1109-1117, 1997.

[21] F. L. Lizzi, E. J. Feleppa, S. K. Alam, and C. X. Deng, "Ultrasonic spectrum analysis for tissue evaluation," *Pattern Recognition Letters,* vol. 24, pp. 637-658, Feb 2003.

[22] R. E. Kumon, A. Repaka, M. Atkinson, A. L. Faulx, R. C. K. Wong, G. A. Isenberg, *et al.*, "Characterization of the pancreas in vivo using EUS spectrum analysis with electronic array echoendoscopes," *Gastrointestinal Endoscopy,* vol. 75, pp. 1175-1183, Jun 2012.

[23] R. E. Kumon, C. X. Deng, and X. D. Wang, "Frequency-Domain Analysis of Photoacoustic Imaging Data from Prostate Adenocarcinoma Tumors in a Murine Model," *Ultrasound in Medicine and Biology,* vol. 37, pp. 834-839, May 2011.

[24] M. F. Insana, R. F. Wagner, D. G. Brown, and T. J. Hall, "Describing Small-Scale Structure in Random-Media Using Pulse-Echo Ultrasound," *Journal of the Acoustical Society of America,* vol. 87, pp. 179-192, Jan 1990.

[25] M. C. Kolios, G. J. Czarnota, M. Lee, J. W. Hunt, and M. D. Sherar, "Ultrasonic spectral parameter characterization of apoptosis," *Ultrasound in Medicine and Biology,* vol. 28, pp. 589-597, May 2002.

[26] G. J. Czarnota, M. C. Kolios, J. Abraham, M. Portnoy, F. P. Ottensmeyer, J. W. Hunt, *et al.*, "Ultrasound imaging of apoptosis: high-resolution non-invasive monitoring of programmed cell death in vitro, in situ and in vivo," *British Journal of Cancer,* vol. 81, pp. 520-527, Oct 1999.

[27] M. Gudur, R. R. Rao, Y. S. Hsiao, A. W. Peterson, C. X. Deng, and J. P. Stegemann, "Noninvasive, Quantitative, Spatiotemporal Characterization of Mineralization in Three-Dimensional Collagen Hydrogels Using High-Resolution Spectral Ultrasound Imaging," *Tissue Engineering Part C-Methods,* vol. 18, pp. 935-946, Dec 2012.

[28] E. M. Czekanska, M. J. Stoddart, R. G. Richards, and J. S. Hayes, "In Search of an Osteoblast Cell Model for in Vitro Research," *European Cells & Materials,* vol. 24, pp. 1-17, Jul-Dec 2012.

[29] A. A. Al-Munajjed, N. A. Plunkett, J. P. Gleeson, T. Weber, C. Jungreuthmayer, T. Levingstone, *et al.*, "Development of a Biomimetic Collagen-Hydroxyapatite Scaffold for Bone Tissue Engineering Using a SBF Immersion Technique," *Journal of Biomedical Materials Research Part B-Applied Biomaterials,* vol. 90B, pp. 584-591, Aug 2009.

[30] H. A. Declerq, R. M. H. Verbeeck, L. I. F. J. M. De Ridder, E. H. Schacht, and M. J. Cornelissen, "Calcification as an indicator of osteoinductive capacity of biomaterials in osteoblastic cell cultures," *Biomaterials,* vol. 26, pp. 4964-4974, Aug 2005.

[31] T. Wakatsuki and E. L. Elson, "Reciprocal interactions between cells and extracellular matrix during remodeling of tissue constructs," *Biophysical Chemistry,* vol. 100, pp. 593-605, 2003.

[32] M. Dembo and Y. L. Wang, "Stresses at the cell-to-substrate interface during locomotion of fibroblasts," *Biophysical Journal*, vol. 76, pp. 2307-2316, Apr 1999.

[33] C. G. Galbraith and M. P. Sheetz, "A micromachined device provides a new bend on fibroblast traction forces," *Proceedings of the National Academy of Sciences of the United States of America*, vol. 94, pp. 9114-9118, Aug 19 1997.

[34] M. Zscharnack, P. Hepp, R. Richter, T. Aigner, R. Schulz, J. Somerson, *et al.*, "Repair of Chronic Osteochondral Defects Using Predifferentiated Mesenchymal Stem Cells in an Ovine Model," *American Journal of Sports Medicine*, vol. 38, pp. 1857-1869, Sep 2010.

CHAPTER 5

Characterization of HIFU Ablation Process

High intensity focused ultrasound (HIFU) technology holds potential for clinical ablation therapy [1-3] due to its ability to noninvasively generate necrosis in targeted tissue volumes with minimal effects on surrounding and intervening tissue. The formation and extent of HIFU-induced tissue necrosis, or thermal lesion, is determined by the spatiotemporal distribution of temperature-increase induced by HIFU exposure [4, 5].To achieve better control of the ablation process, robust and effective imaging methods are needed for real-time monitoring of tissue changes such as lesion formation during HIFU application. Magnetic resonance imaging (MRI) has been valuable in guiding and monitoring HIFU ablations [6-8] in real-time with spatial and temporal control on temperature rise in the tissue induced by HIFU. While magnetic resonance imaging (MRI) [6] and x-ray computed tomography (CT) [9] have been used as effective image guidance during ablation, monitoring with diagnostic ultrasound imaging has the advantage of relatively lower cost, higher portability, and high spatiotemporal resolution. Although a variety of methods have been proposed to improve ultrasound imaging of HIFU ablation and lesion formation, ultrasound imaging has not yet been established as a robust and consistent technique.

5.1 Introduction

The tissue changes generated by HIFU application include changes in the acoustical properties such as sound speed, attenuation, and ultrasound backscatter due to protein denaturation, coagulation, gas-body formation, and other effects. While a variety of methods like temperature changes by tracking echo shifts [10], changes in ultrasound backscatter [11-13], elastographic imaging [14-17], attenuation changes [18-20], spectral analysis [21], echo decorrelation [22] have been proposed to improve ultrasound imaging of HIFU ablation and lesion formation based on these changes, ultrasound imaging has not yet been established as a robust and consistent technique.

Occurrence of gas bodies is another event that often forms during HIFU ablation due to cavitation, tissue degassing, and/or boiling [23]. These gas bodies strongly scatter ultrasound and distort the HIFU beam, resulting in inefficient ablation of distal tissue segment [24] and altered lesion location, shape and size from the original treatment plan. The presence of gas bodies can also result in enhanced heating beyond thermoviscous absorption [25]. In some cases, due to the combined effect of high acoustic pressure and rapid heating, macroscopic cavities may be generated in tissue during ablation. The stochastic nature of these events causes variation in outcomes that are not well controlled. Thus it is important to detect these events and develop strategies to prevent them. To detect these gas bodies, various passive [26-29] and active cavitation detection strategies [28, 30-32] have been proposed including methods for spatial cavitation mapping [33-35] to locate these gas bodies, but no clear strategies have been developed to predict the capability of gas bodies in creating macroscopic cavity in the tissue.

In this study, we focus on developing methods of high frequency, high frame rate B-mode ultrasound imaging to monitor formation of lesion and gas bodies during HIFU ablation using *ex vivo* cardiac tissue specimens, aiming to improvise the monitoring method in HIFU treatment of atrial fibrillation. B-mode RF data were acquired and are analyzed using grayscale, integrated backscatter, calibrated spectral parameters, echo decorrelation to obtain time-evolving HIFU-monitoring parameters. By comparing against gross images, the best method(s) for lesion identification are assessed via receiver-operating characteristic (ROC) curves [36]. For gas-body identification, a frame-to-frame echo decorrelation method [22] is proposed to evaluate the dynamic local motion and the expansion rate of the gas bodies and to predict the formation of cavities during ablation. The results from this study were submitted to IEEE Transactions on UFFC, volume 59, issue 8, 2012 with the title, "High-frequency rapid B-mode ultrasound imaging for real-time monitoring of lesion formation and gas body activity during high-intensity focused ultrasound ablation" [37].

5.2 Methods

The experimental setup, shown in Figure 5.1(a) [37], consists of a HIFU system and a high frequency ultrasound imaging system (Vevo 770, VisualSonics, Toronto, Canada). In a water tank, the HIFU transducer and a Vevo imaging probe (RMV 708, nominal 55 MHz center freq., 20-75 MHz bandwidth [−6 dB], 4.5 mm focal distance, 1.5 mm depth of focus [−6 dB]) were perpendicularly and confocally aligned with the common focus placed within *ex vivo* porcine cardiac tissue. The HIFU system consisted of a signal generator, power amplifier, and spherically focused HIFU transducer (4.33 MHz center frequency, 40 mm diameter, 42 mm focal distance) and was used to generate pulsed exposures with 2600 W/cm^2 focal intensity and various PRF's (77 Hz, 103 Hz, 130 Hz), duty cycles (25%, 50%) and exposure times (0.2 s, 0.6 s, 1 s). The STBM imaging was synchronized with the HIFU pulses to image during the off-duration of the HIFU pulses to avoid interference (Figure 5.1(b)), thus the frame rate of STBM imaging was the PRF of the pulsed HIFU exposure.

To achieve a high frame rate of imaging, short-time B-mode (STBM) imaging (B-mode imaging with a reduced window size of dimensions 0.8 mm x 11 mm) was employed. Backscattered RF data of STBM imaging were acquired before, during and after HIFU application. After the experiment, the tissue was cut transversely through the lesion and photographs of the lesion cross-section were taken.

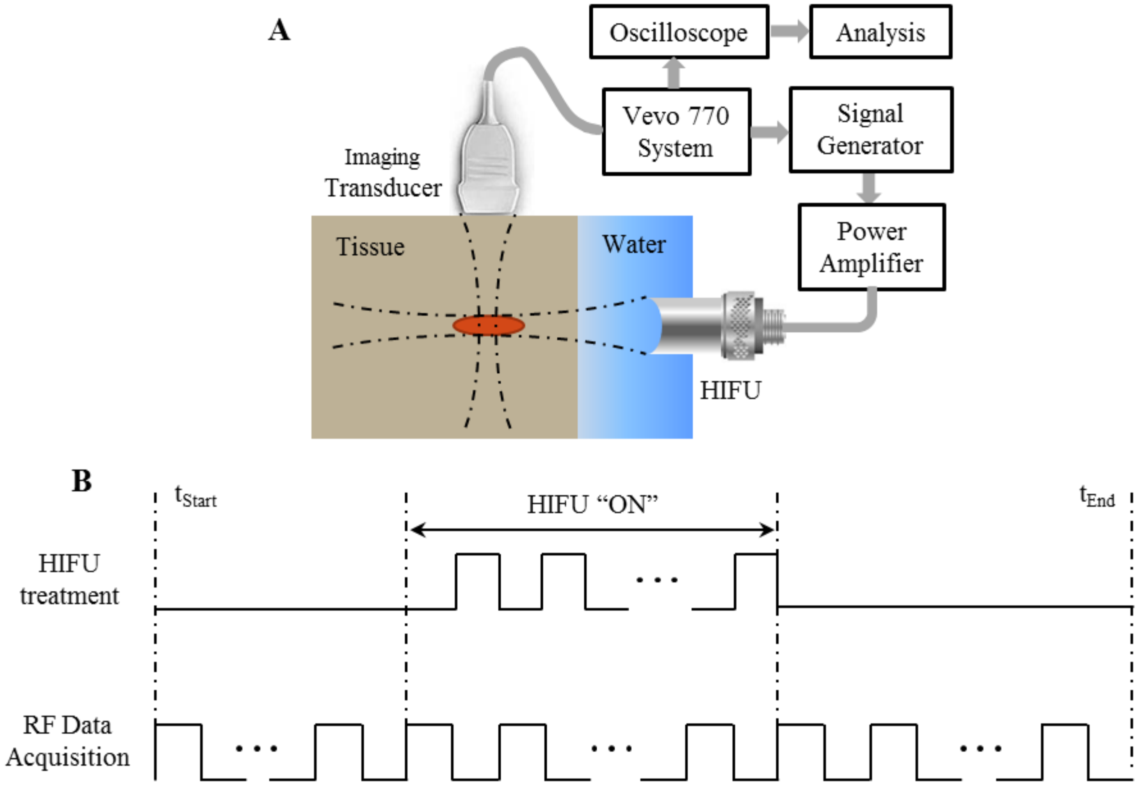

Figure 5.1 (A) Experimental setup of image-guided HIFU system (not to scale) (B) Sequence of HIFU and RF synchronized pulses.

5.2.1 Feature Estimation Parameters: The following estimation parameters were computed from the acquired RF data:

5.2.1.1 Grayscale (GS): The A-line signal acquired in STBM data was Hilbert transformed to obtain the complex analytic signal $p(y,z,t)$. The grayscale parameter in decibels (dB) of a spatially smoothed frame at time t is calculated as

$$GS(y,z,t) = \log_{10}\left(\left\langle \left| p(y,z,t) \right| \right\rangle\right), \tag{5.1}$$

where the spatial smoothing with window $w(y,z)$ was defined by

$$\begin{aligned} \left\langle f(y,z) \right\rangle &= \iint w(y-y_0, z-z_0)\, f(y_0,z_0)\, dy_0 dz_0 \\ &= w(y,z) \otimes f(y,z) \end{aligned} . \tag{5.2}$$

An isotropic Gaussian window

$$w(y,z) = e^{-\left(y^2+z^2\right)/2\gamma^2} \tag{5.3}$$

was used as the smoothing window represented in Eq. (2) with the length scale γ as 14 µm.

5.2.1.2 Integrated Backscatter (IBS): The auto-correlation function of a frame at time t is $R_0(y,z,t) = \left\langle \left| p(y,z,t) \right|^2 \right\rangle$. The position-dependent change in echo energy by integrated backscatter relative to the initial state, measured in decibels, is defined as [22]

$$IBS(y,z,t) = 10\log_{10}\left(\frac{R_0(y,z,t)}{R_0(y,z,0)}\right), \tag{5.4}$$

where $R_0(y,z,0)$ is the temporal average of autocorrelation of the frames before HIFU ablation treatment.

5.2.1.3 Frame-to-Frame Decorrelation: A spatiotemporal correlation function between two successive frames with a time delay τ [22] is $R(y,z,t,\tau) = \left\langle p(y,z,t)\, p^*(y,z,t+\tau) \right\rangle$. The normalized frame-to-frame decorrelation parameter similar to the variance of the spectrum in “flow turbulence” denoted by Kasai et al. [38], is then defined as

$$\sigma_{FF}(y,z,t,\tau) = \left| \frac{2\left(R_0(y,z,t) - \left|R(y,z,t,\tau)\right|\right)}{R_0(y,z,t) + \overline{R_0}(t)} \right| , \tag{5.5}$$

where $\overline{R_0}(t)$ is the spatial mean of $R_0(y,z,t)$ for the frame obtained at time t.

5.2.1.4 Initial Frame Decorrelation: The initial frame decorrelation is defined as the decorrelation between any frame at time *t* and a frame at *t* = 0 (initial frame):

$$\sigma_{IF}\left(y,z,t\right)=\left|\frac{2\left(R_0\left(y,z,0\right)-\left|R\left(y,z,0,t\right)\right|\right)}{R_0\left(y,z,0\right)+\overline{R}_0\left(0\right)}\right|, \tag{5.6}$$

5.2.1.5 Spectral Parameters: The power spectrum of the STBM data was calculated for the signals of each RF A-scan within the ROI by taking the Fast Fourier Transform (FFT) of the data gated by a series of sliding Hamming windows of 0.2 μs, each offset by 0.1 μs. The calibrated power spectra were characterized by linear regression to find the spectral parameters, i.e. the midband-fit $M\left(y,z,t\right)$, which is the value of the linear function evaluated at the midpoint of the −15 dB bandwidth, the slope $m\left(y,z,t\right)$, and the intercept $I\left(y,z,t\right)$. The relative change in the spectral parameters were computed to minimize the effects of variability in the initial state of the specimens, e.g., for midband fit, $\Delta M\left(y,z,t\right)=M\left(y,z,t\right)-M_0\left(y,z\right)$, where $M_0\left(y,z\right)$ is the temporal average value of the spectral parameter in the frames prior to application of HIFU.

5.2.2 Lesion mask and lesion identification: To construct ROC curves between the post-HIFU frame of STBM data and the gross image, a binary mask for the lesion in gross image at the STBM window location was identified. The proposed parameters defined in *A.1*-*A.5* are evaluated on each frame of STBM data. For any given parameter $X(y, z, t)$ defined in *A.1*-*A.5*, the temporal maximum of the parameter was also computed according to

$$X_{\max}\left(y,z,t_0\right)=\max_t\left(X\left(y,z,0\le t\le t_0\right)\right). \tag{5.7}$$

This functional form captures the overall time history of the parameter in an effort to account for the irreversible nature of the HIFU ablation process. By thresholding $X_{\max}\left(y,z,t_0\right)$ on the last frame of STBM data, when the entire lesion has formed, a binary mask was generated and compared with the mask from the gross lesion on a pixel-by-pixel basis. By varying the threshold, receiver operating characteristic (ROC) curve and the accuracy curves were constructed. The pixel-by-pixel classification was applied on 24 datasets and overall ROC and accuracy curves were generated. The "optimal" threshold is chosen to be the parameter threshold value at maximum accuracy.

5.2.3 Identification of gas bodies: The frame-to-frame echo decorrelation parameter σ_{FF} can be used to capture rapid changes in successive frames, and hence this parameter is proposed to identify any newly-formed or actively moving gas bodies, including any active process involving the expansion of the tissue. Because no gas bodies are likely to exist within the tissue prior to the initiation of HIFU treatment, any parameter used for classification of gas-body activity should, at minimum, not identify gas bodies during the pre-HIFU period. For any given parametric image $\sigma_{FF}(y,z,t)$, the threshold σ_{FF}^{0} for gas-body identification was chosen to be minimum value of σ_{FF} such that $\sigma_{FF}(y,z,t) < \sigma_{FF}^{0}$ for all y and z at all $t < t_{\mathrm{ON}}$, where t_{ON} is the time of HIFU initiation. After gas bodies were identified, the amount of the displacement of their top most pixel from the focal spot was tracked in each frame to evaluate the rate at which the cavity is expanding, defined as dynamic expansion rate (ER) of the cavity. A moving-average filter of duration 0.08 s was applied to the displacement of gas bodies to remove the artifacts due to tissue movements that may have occurred during HIFU. After classifying each lesion as "cavity-forming" or "non-cavity-forming" based on the existence of macroscopic cavities in gross lesions, the expansion rate for each specimen was computed and then a threshold to segregate the two types of lesion was determined.

5.3 Results

5.3.1 High Frequency Rapid B-mode Imaging during HIFU ablation

Figure 5.2 [37] shows an example for HIFU ablation (4.33 MHz center freq., 2600 W/cm^2, 77 Hz PRF, 50% duty cycle and 1 s exposure time) illustrating the complex dynamic changes in tissue during HIFU exposure involving tissue necrosis and formation of gas bodies. With the HIFU beam incident from the left side of the image, the B-mode image after HIFU (Figure 5.2B) clearly shows the lesion compared with the image before HIFU (Figure 5.2A), and matches very well with the gross image of the lesion (Figure 5.2C). The dashed vertical lines indicate the lateral boundaries of the short time, B-mode (STBM) window. While the spatiotemporal evolution of the lesion can be more readily appreciated in the video playback of the STBM frames, the horizontally stacked images are included in Fig. 5.2D for convenient representation. Selected frames from Figure 5.2D are enlarged to better show the dynamics of HIFU lesion and gas body evolution in detail in Frames 5.2F_1–F_{11}. After the HIFU is turned on at t =0.02 s, a bright hyperechoic region appeared near the focus after a time delay at t = 0.16 s, most likely representing gas-body activity generated by acoustic cavitation and thermally induced water vaporization at the 2600 W/cm^2 intensity [28] and the relatively high frequency of the HIFU transducer used in this study. The initiation of gas-body activity is clearly shown starting from the left side in Frame 5.2F_2 (closer to the HIFU transducer) and then growing in subsequent Frames 5.2F_3–F_4 before filling the entire width of the window by Frame 5.2F_6. The hyperechoic region appears to grow and expand laterally with respect to the HIFU beam axis (Frame 5.2F_7). This lateral expansion of the hyperechoic region could be due to the combined effects of apparent echo strain resulting from variation in speed of sound at elevated temperatures and thermal expansion of the tissue. After the HIFU is turned off, the bright regions

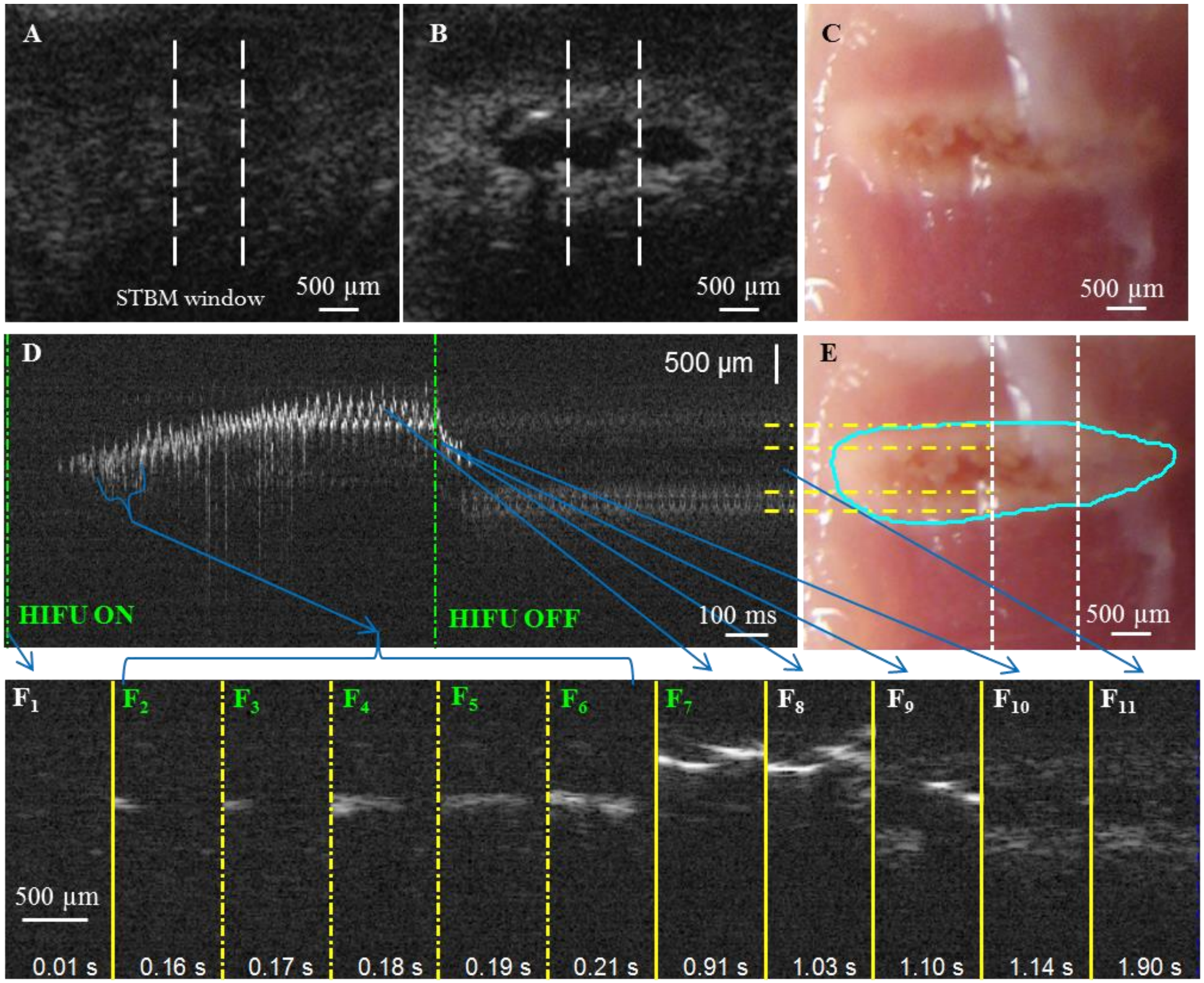

Figure 5.2 (A) Grayscale B-mode images (A) before and (B) after HIFU with dash-dotted lines showing the location of the Short-Time B-Mode (STBM) window that was used for imaging during HIFU at a frame rate of 77 Hz, intensity of 2600 W/cm^2, 50% duty cycle, and 1 s exposure time. The direction of HIFU beam was from left to right. (C) Post-HIFU photograph of lesion and cavity in gross tissue specimen. (D) Horizontally-stacked STBM grayscale frames showing the spatiotemporal evolution of the lesion in the STBM window. Vertical green dash-dotted lines indicate the times when the HIFU was turned on and off. (E) Photograph of lesion and cavity in gross tissue specimen, rescaled to have the same spatial scale as Fig. D. The contour on the outer edge of the lesion has been marked (cyan), and the location of STBM window lines is shown by the white dashed lines. The dashed yellow lines show correspondence between features in ultrasound and optical images. (F) Selected individual STBM grayscale frames before (F_1), during (F_2–F_7), and after (F_8–F_{11}) application of HIFU.

move downward (away from the imaging transducer), indicating contraction and maybe dissipation of the gas bodies (Frames 5.2F_8 and 5.2F_9) and two weakly echogenic regions become visible, separated by a hypoechoic region in between (Figure 5.2D and Frames 5.2F_8 and 5.2F_9). These hyperechoic and hypoechoic regions from STBM (indicated by the white vertical dashed lines) correspond well with the tissue necrosis and cavity regions of the gross tissue image (Figure 5.2E) (same as Figure 5.2C). Figure 5.2E also highlights the contour (cyan line) manually drawn along the outer edge of the lesion to indicate the area of necrosis.

5.3.2 Lesion Identification

To construct ROC curves between the post-HIFU frame of STBM data and the gross image, we identified a binary mask for the lesion in gross image at the STBM window location. As shown by the general block diagram for the procedure (Figure 5.3A [37]), first the area of necrosis was indicated manually by the outer edge of the lesion (e.g., cyan contour in Figure 5.3B) on the gross image of the tissue specimen. Then, to represent the STBM window location on gross image, the post-HIFU B-mode image that was registered with the STBM window location (white dashed lines in Figure 5.3C) was overlaid on top of gross image to register common structural features such as lesion, cavity (if exists), and boundaries of the tissue. After registering the STBM window in the gross image (Figure 5.3D), the lesion area was used to create a binary mask (Figure 5.3E) for representing the necrosed area (i.e., 1 is necrosed tissue

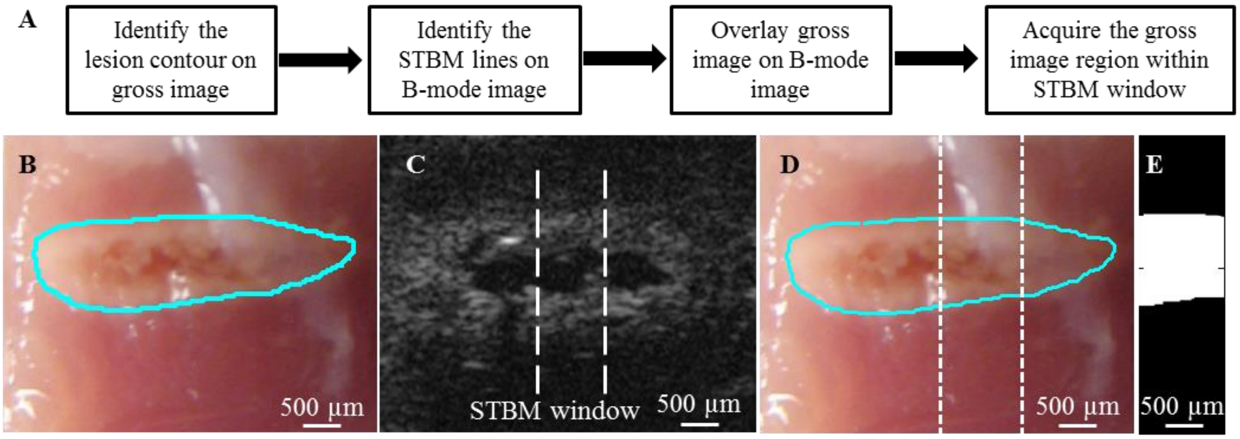

Figure 5.3 (A) Block diagram of procedure for obtaining the binary mask of lesion in gross image. (B) Manually drawn outer edge of the lesion (cyan) in gross image. (C) Registration of STBM window location (white dashed lines) in B-mode image. (D) Spotted STBM window location on gross image after overlaying Fig. 2C on Fig. 2B. (E) The binary mask of lesion obtained from gross image in Fig. 2D.

and 0 is non-necrosed). The proposed parameters defined in Eq. **Error! Reference source not found.** to **Error! Reference source not found.** along with spectral parameters are evaluated on each frame of STBM data. For any given parameter $X(y, z, t)$ defined in Eqs. **Error! Reference source not found.** to **Error! Reference source not found.**, the temporal maximum of the parameter was also computed according to

$$X_{\max}(y,z,t_0) = \max_t \left(X\left(y,z,0 \le t \le t_0\right)\right). \tag{1}$$

This functional form captures the overall time history of the parameter in an effort to account for the irreversible nature of the HIFU ablation process. By applying a threshold to the final frame of $X_{\max}(y,z,t_0)$, when the entire lesion has formed, accuracy of the parameter for lesion identification at that threshold was determined. By applying this procedure to all the data sets, an overall ROC curve was generated for each parameter (Figure 5.4 [37]). The ROC area under the curve (AUC), maximum accuracy, optimal threshold at maximum accuracy, sensitivity, and specificity from pixel-by-pixel classification for each parameter is shown in Table 1. $IBS_{\max}$ and $\Delta M_{\max}$ have highest areas under the ROC curve (ROC AUC ~ 0.96). We chose to compute $IBS_{\max}$ for subsequent analysis as it had the highest AUC. The maximum accuracy in detecting the lesion was obtained at an $IBS_{\max}$ of +12 dB.

An abrupt increase in IBS was observed when gas bodies were identified by the echo decorrelation method and agrees well with a study [20] where cavitation detection showed largest changes in IBS associated with cavitation activity. In a study on *ex vivo* bovine liver [39], the AUC ROC for intercept and midband fit in characterizing the lesion reported were 0.71 and 0.69, respectively, which are comparable to values found in the current work (ΔI : 0.737, ΔM : 0.745), but the values for the corresponding temporal extrema ($\Delta I_{\max}$: 0.903, $\Delta M_{\max}$: 0.947) in Table 5.1 were much better. The improved ROC performance of $\Delta M_{\max}$ and $\Delta I_{\max}$ suggest that

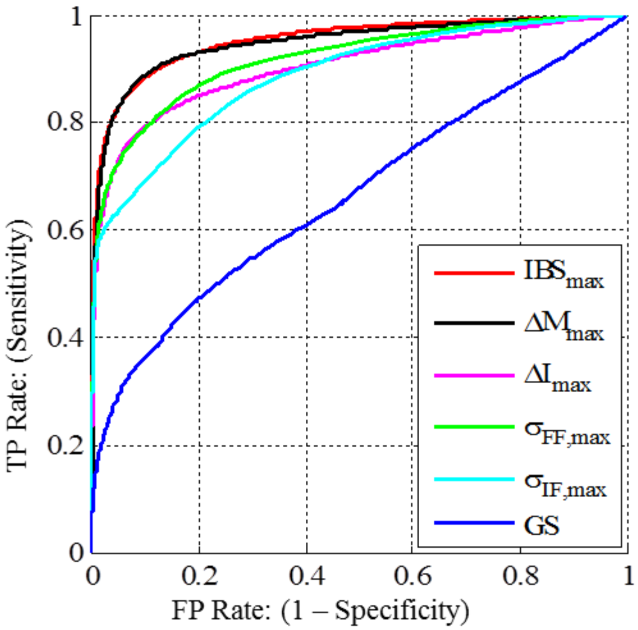

Figure 5.4 Comparison of overall ROC curves for several methods in detecting the lesion for all specimens (IBS$_{max}$: temporal maximum (t.m.) of integrated backscatter, ΔM_{max}: t.m. of relative change in mid-band fit, ΔI_{max} : t.m. of relative change in intercept, $\sigma_{FF,\max}$: t.m. of frame-to-frame decorrelation, $\sigma_{IF,\max}$: t.m. of initial frame decorrelation, and GS: Grayscale)

the usage of ablation time history via the temporal maximum method can increase the performance of these parameters for lesion identification.

Table 5.1. Results from pixel-by-pixel lesion classification for different parameters.

Parameter	AUC	Threshold	Accuracy	Sensitivity	Specificity
IBS_{max} (dB)	0.96	12.0	0.94	0.76	0.98
ΔM_{max} (dB)	0.95	15.8	0.93	0.79	0.97
ΔI_{max} (dB)	0.91	25.5	0.91	0.68	0.97
$\sigma_{FF,\ max}$	0.93	1.28	0.92	0.66	0.98
$\sigma_{IF,\ max}$	0.91	1.48	0.91	0.57	0.99
Grayscale (dB)	0.68	0.75	0.84	0.20	0.98
Δm_{max} (dB/MHz)	0.52	0.49	0.79	0.8	0.97

To check the importance of high imaging frame rate on the performance of $IBS_{\max}$ in identifying the lesion, the frame rate of each dataset was manually decimated to half the original frame rate. Upon generating the $IBS_{\max}$ ROC curves of these decimated frame rate datasets, a drop in the ROC AUC (area under curve) by 20%, accuracy by 2%, and the sensitivity by 20% was observed. The drop is more prominent in the case when frame rate was reduced from 130 Hz to 65 Hz than in the case of 77 Hz to 39 Hz indicating that higher frame rate indeed improves the lesion identification by capturing faster events.

5.3.3 Identification and Tracking of Gas Bodies

As an example, Figure 5.3 shows a series of stacked short time B-mode frames with gas-body activity marked in green, as identified by frame-to-frame echo decorrelation method. The top-most pixel in each frame that is identified as gas-body activity (if there exists one) is represented by red dot to track its location in time. Cases where pronounced movement/expansion of the tracked gas bodies occurred (Figure 5.5A [37], 2600 W/cm^2, 77 Hz PRF, 50% duty cycle and 1 s exposure time) were well correlated with the existence of macroscopic cavity formation during HIFU as shown in gross image (Figure 5.5B), in contrast with minimal movement of gas bodies for cases where no observable macroscopic cavity was generated (Figure 5.5C and 5.5D) (2600 W/cm^2, 77 Hz PRF, 50% duty cycle and 0.2 s exposure time). The displacements from the center line were tracked and the corresponding expansion rate (ER) of the top-most gas-body location was computed. Figure 5.6 [37] shows that the non-cavity datasets have a significantly lower ER (0.51 ± 0.21 mm/s, $n = 5$) compared to the cavity datasets (1.37 ± 0.39 mm/s, $n = 19$) based on a T-test ($p < 10^{-4}$). As a result, a threshold of 0.8 mm/s was chosen to classify those gas bodies associated with cavity formation based on the maximum ER value among the non-cavity data sets.

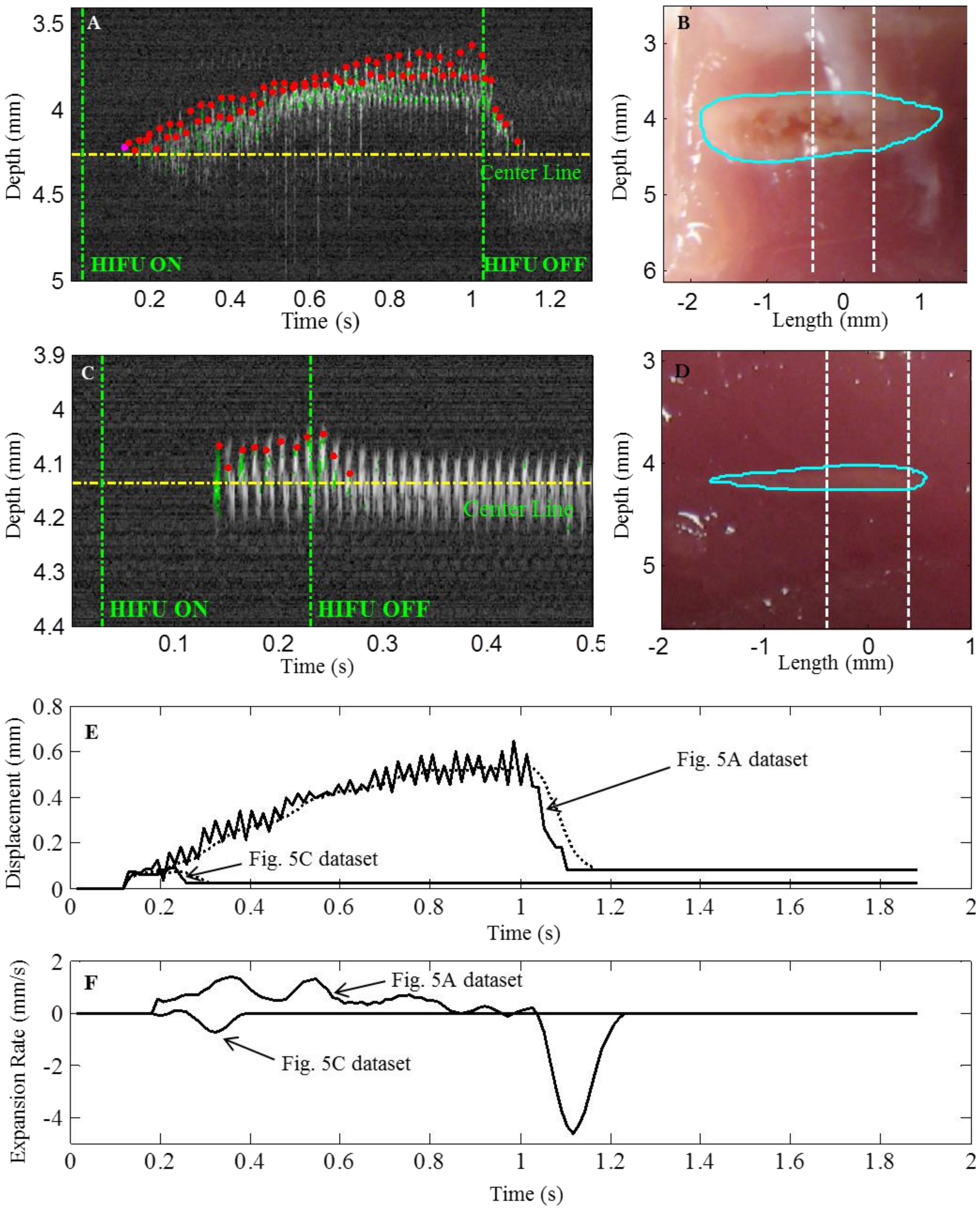

Figure 5.5. (A) Stacked short-time B-mode (STBM) grayscale frames with marked regions of gas-body activity (green pixels) of dataset with macroscopic cavity (data in Figs. 5.2). The top most green pixel in each frame is marked by a red dot. Vertical dash-dotted lines indicate the times when the HIFU was turned on and off. (B) Gross image of dataset in (A) with lesion contour (cyan) and location of STBM

window lines (vertical white dashed lines) (C) STBM grayscale frames with marked regions of gas-body activity of dataset without macroscopic cavity (D) its gross image. (E) Position of uppermost gas-body activity in the cavity dataset (Fig. 5.5A), non-cavity dataset (Fig. 5.5C) and their corresponding moving average (dashed lines) based on a averaging window of 0.08 s. (F) Expansion rate of gas-body activity from numerical derivatives of curves in Fig. 5.5A.

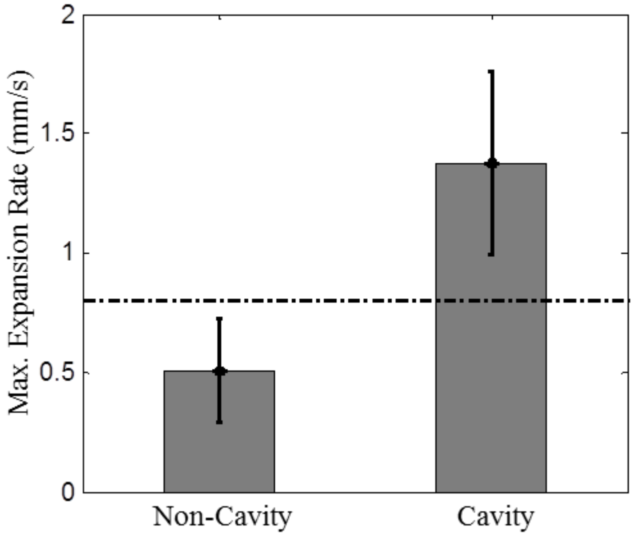

Figure 5.6 Expansion rate of non-cavity (*n* = 5) and cavity (*n* = 19) datasets with error bars. The selected expansion rate threshold (0.8 mm/s) is shown by the dot-dashed horizontal line.

Using the criteria for identification of lesion and gas bodies, parametrically-labeled images were generated retrospectively to demonstrate the feasibility of tracking lesion and gas-body formation during HIFU exposure.

5.3.4 Parametric Imaging for Lesion and Gas Body Marking during HIFU Ablation

For the data of Figure 5.2, Figure 5.7 [37] shows selected grayscale image frames with markings for the lesion, gas-body activity, and cavity-formation superimposed (See **Media-Movie 5.1** for the corresponding video). Consecutive frames are separated by white dashed vertical lines and others by blue dashed lines. Frame 5.7A_1 shows the last frame prior to HIFU application, with the early evolution of the lesion (red) after the initiation of gas-body activity shown in Frames 5.7A_2–A_5. The ER of the gas bodies is below the threshold until Frame 5.7A_5, and these gas bodies are represented in green. At 0.299 s (Frame 5.7A_6), the ER crosses the

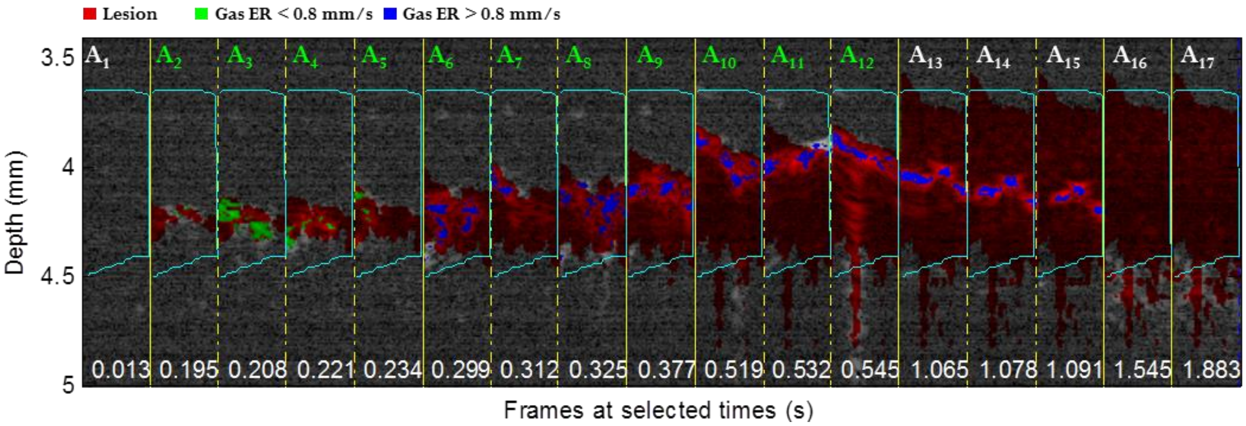

Figure 5.7 Example of lesion with gas-body activity and cavity formation (2600 W/cm^2, 77 Hz PRF, 50% duty cycle and 1 s exposure time). The time evolution of ablation process is shown at selected times. The green frame labels indicate the frames during HIFU exposure. The area of tissue necrosis evaluated using the optimal IBS_{max} threshold of 12 dB is represented in red, gas bodies expanding at less than expansion rate threshold (<0.8 mm/s) in green, and gas bodies which crossed expansion rate threshold in blue (≥0.8 mm/s). The lesion contour in each frame is shown in cyan.

threshold, indicating the capability of the gas bodies to create a cavity, and reaches a maximum ER of 1.36 mm/s at 0.377 s (Frame 5.7A$_9$). The gas bodies in Frames 5.7A$_6$–A$_{17}$ are then color coded in blue. The gas body expands, and the lesion grows until Frame 5.7A$_{13}$ when the HIFU is turned off. Frames 5.7A$_{14}$–A$_{16}$ show a downward movement, representing shrinking and dissipation of the gas-body activity. The lesion- marking algorithm covers most of the area of lesion contour (cyan curve) determined from the gross lesion, although lesion extent is over-estimated in the region below the lesion. This overestimation is likely due to reverberation artifacts of the backscattered ultrasound from the HIFU-induced gas body, as seen in Frames 5.7A$_{10}$ and 5.7A$_{12}$.

5.3.4.1 Effect of PRF

Figure 5.8 [37] shows an example of a case with HIFU ablation at higher PRF than in that for the case in Figure 5.7 (130 Hz vs. 77 Hz) with all other conditions equal. A cavity apparent in the B-mode image after HIFU treatment (Figure 5.8A) is confirmed in the gross image

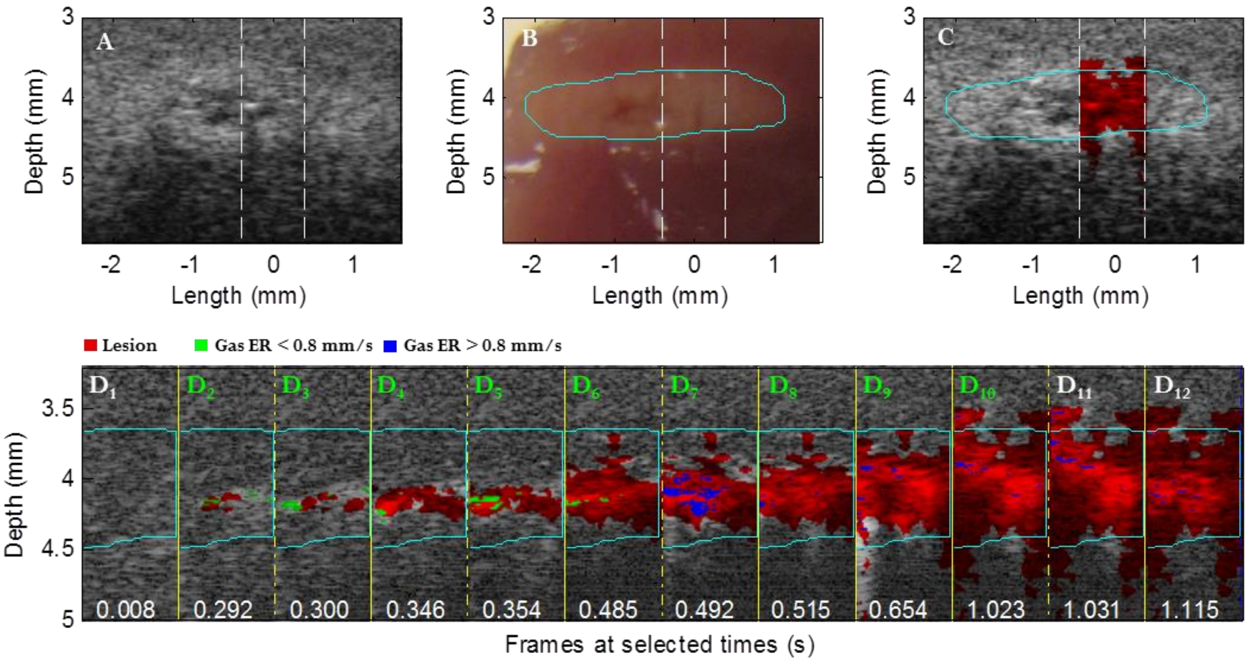

Figure 5.8 Example of lesion with gas-body activity and cavity formation (2600 W/cm^2, 130 Hz PRF, 50% duty cycle and 1 s exposure time). (A) B-mode image after HIFU treatment with location of STBM window shown by the dashed vertical lines (white). (B) Image of gross tissue with lesion, manually estimated lesion contour (cyan), and location of STBM window (vertical dashed green lines). (C) B-mode image with an overlay of predicted lesion (red) using $IBS_{\max}$ in STBM window and manually estimated lesion contour (cyan) from gross image. (D) Time evolution of ablation process is shown at selected times (see Fig. 5.7 caption for description of colors).

(Figure 5.8B). The extent of lesion area (red) predicted from STBM data using $IBS_{\max}$ with +12 dB threshold is overlaid on STBM window of the post-HIFU B-mode image (Figure 5.8C). As shown in Figure 5.8D, selected frames from the time evolution of the ablation, higher PRF ablation generates less area identified as gas and a smaller cavity size in the gross tissue as compared to Figure 5.7. The ER crossed the cavity-formation threshold at 0.492 s (frame 5.8D_7), reaching a maximum ER of 1.35 mm/s at 0.515 s (frame 8D_8), and then dissipation of gas bodies occurred after the HIFU was turned off. When the cases with 77 Hz and 130 Hz PRF are compared (2600 W/cm^2, 50% duty cycle), the durations for crossing the ER threshold after HIFU was turned on were 0.324 ± 0.090 s ($n = 8$) and 0.405 ± 0.054 s ($n = 4$), respectively, although the difference was not quite statistically significant (T-test with unequal variances, $p = 0.077$).

The increased delay illustrated in Figure 5.8 as compared to Figure 5.7 suggests that higher PRF may result in slower expansion. This slower growth of gas bodies could be the reason for smaller cavity size (cavity area = 0.089 ± 0.069 mm^2, *n* = 4 for 130 Hz vs. 0.187 ± 0.064 mm^2, *n* = 4 for 77 Hz with other conditions 2600 W/cm^2, 50% duty cycle and 1 s exposure time being same) at the end of the ablation as seen in the gross image (Figure 8B).

5.3.4.2 Effect of Exposure Duration

Figure 5.9 [37] shows an example of a dataset with lower exposure duration than in Figure 5.7 (0.2 s vs. 1.0 s) with all other conditions equal. (See **Media-Movie 5.2** for the corresponding video). The B-mode image shown in Figure 5.9A does not show any hypoechoic regions without the presence of a macroscopic cavity in the lesion (Figure 5.9B). The predicted lesion area (red) from STBM data is overlaid on STBM region of post HIFU B-mode image (Figure 5.9C). Figure 5.9D shows a composite image that presents the evolution of the ablation process with time. Although sudden occurrence of gas bodies (Frame 9D$_3$) and their initial activity (Frames 5.9D$_3$–D$_5$) was observed, the short HIFU exposure duration limited the chance for the expansion/movement of these gas bodies and formation of a tissue cavity. (At Frame 5.9D$_6$ the HIFU was turned off.) Because the ER of the gas bodies did not cross the threshold, they remain colored in green. In the datasets with lower HIFU exposure times (with all other conditions equal: 2600 W/cm^2, 77 Hz PRF, 50% duty cycle), the cavity was either absent (0.2 s exposure, *n* = 5) or small (cavity area = 0.066 ± 0.039 mm^2 for 0.6 s exposure, *n* = 6) compared to Figure 5.7 (cavity area = 0.187 ± 0.064 mm^2 for 1 s exposure, *n* = 4). The non-cavity datasets (all of which were 0.2 s exposure cases and without cavity in the gross images) in Fig. 5.6 were used to determine the ER threshold in the model so that no cavity is predicted in those datasets. For the datasets with 0.6 s and 1 s exposure, the maximum ERs (1.4 ± 0.2 mm/s

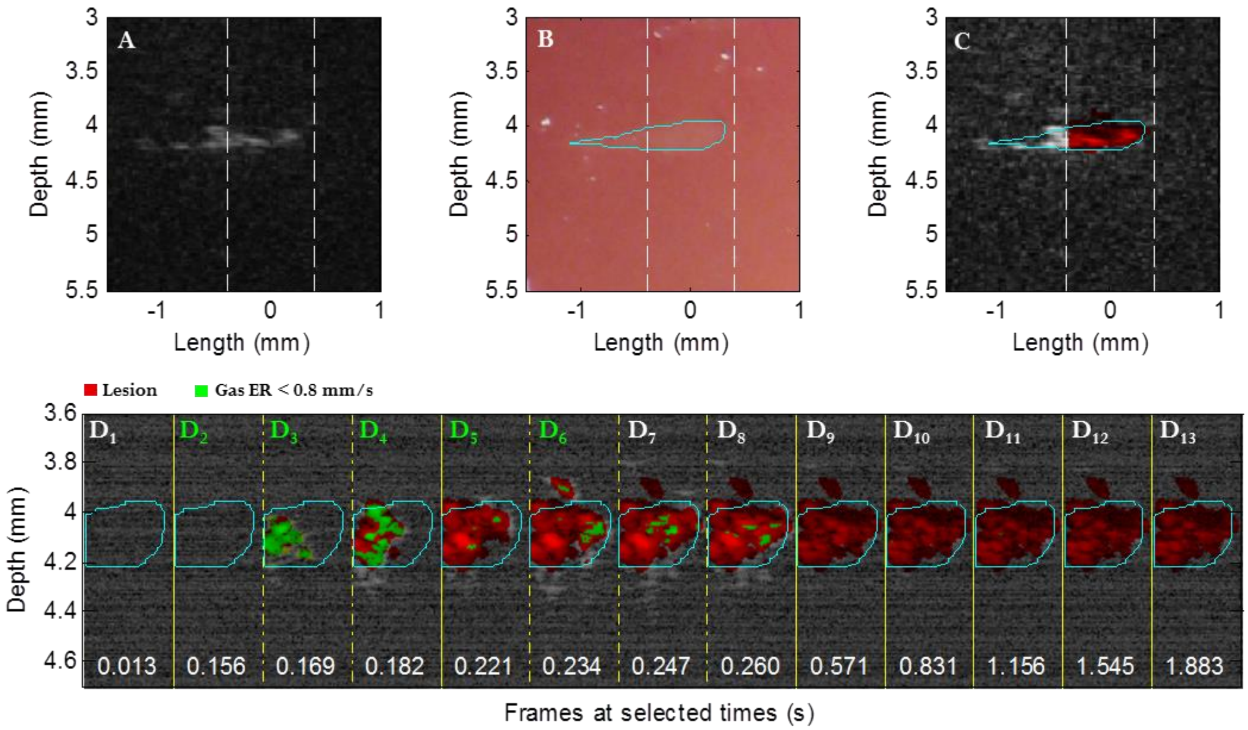

Figure 5.9 Example of lesion with gas-body activity but without macroscopic cavity formation (2600 W/cm^2, 77 Hz PRF, 50% duty cycle and 0.2 s exposure time). (A) B-mode image after HIFU treatment with location of STBM window shown by the dashed vertical lines (white). (B) Image of gross tissue with lesion, manually drawn lesion contour (cyan), and location of STBM window (vertical dashed green lines). (C) B-mode image with an overlay of predicted lesion (red) using $IBS_{\max}$ in STBM window and manually estimated lesion contour (cyan) from gross image. (D) Time evolution of ablation process is shown at selected times (see Fig. 5.7 caption for description of colors).

vs. 1.5 ± 0.3 mm/s) and their time of occurrence (0.44 ± 0.04 s vs. 0.42 ± 0.04 s) were nearly the same. However, the total expansion was higher in the cases with longer exposure, resulting in a larger cavity size.

5.4 Discussion

5.4.1 Lesion Identification

Integrated backscatter, spectral parameters, and echo decorrelation have been explored in estimating the formation of lesion area in previous work and a comparison on each parameter was made with the results observed in current paper in the following paragraphs.

The changes in integrated backscatter ($IBS_{\max}$) has been used previously to monitor HIFU lesion formation with B-mode RF data acquisition in *ex vivo* bovine liver [19, 20], although at lower imaging frequency of 7.5 MHz when compared to 55 MHz imaging frequency used in the current study. The authors observed sudden increases in the apparent width of the lesion midway through the exposure period, similar to the results observed at the longer exposure times in the current study (e.g., Figure 5.7). A subsequent study with cavitation detection showed that the largest changes in IBS were associated with the cavitation activity [20]. In the current study, we also observed an abrupt increase in IBS when gas bodies were identified by the echo decorrelation method. We showed that the temporal maximum IBS performed better than the IBS alone in identifying the extent of the lesion as compared to the final state. However, the current method does appear to be affected by reverberation artifacts when extensive gas body formation occurs (Figure 5.7, 5.8).

For the spectral parameters, the ΔM and ΔI increases observed in lesions induced by HIFU of current study are consistent with other studies [21, 40], where an increase in midband fit of 6 to 8 dB in lesion over surrounding non-ablated tissue was observed in *ex vivo* chicken breast and rabbit liver. The slope parameter Δm in the current study yielded inconsistent results from case to case and was not useful for lesion identification (see Table 5.1). Spectral parameters have also been computed to characterize lesions induced by RF ablation in *ex vivo* bovine liver [39]. The AUC ROC for intercept and midband fit were reported to be 0.71 and 0.69, respectively, which are comparable to values found in the current work (ΔI : 0.74 ± 0.13, ΔM : 0.75 ± 0.14), but worse than values for the corresponding temporal extrema ($\Delta I_{\max}$: 0.91 ± 0.06, $\Delta M_{\max}$: 0.95 ± 0.04) in Table 5.1. The improved ROC performance of $\Delta M_{\max}$ and $\Delta I_{\max}$ suggest that the usage of ablation time history via the temporal maximum method can increase the performance of these parameters for lesion identification.

In the current study, $IBS_{\max}$ showed slightly better performance in lesion identification (ROC AUC 0.96 ± 0.02) as compared to $\sigma_{FF,\max}$ (ROC AUC 0.93 ± 0.05), although the performance of $\sigma_{FF,\max}$ was comparable to the previous study [22, 41]. The difference in the performance of $IBS_{\max}$ in the current study from [22] could be due to higher bandwidth, the increased backscatter due to HIFU-induced gas body formation, and higher imaging rate (77–130 Hz vs 50 Hz), which might allow $IBS_{\max}$ to capture faster activities and events.

The temporal extrema of the parameters uses the time history of ablation via. Eq. (1) and a comparison between the performance of the parameters with and without temporal extrema shown in Table 1 shows the value added by using the time history of ablation in the lesion detection process. For all of the parameters, nearly a 20% increase in both ROC AUC and accuracy were observed when the time history of ablation was used.

To check the importance of high imaging frame rate on the performance of $IBS_{\max}$ in identifying the lesion, the frame rate of each dataset was manually decimated to half the original frame rate. Upon generating the $IBS_{\max}$ ROC curves of these decimated frame rate datasets, a drop in the ROC AUC (area under curve) by 20%, accuracy by 2%, and the sensitivity by 20% was observed. The drop is more prominent in the case when frame rate was reduced from 130 Hz to 65 Hz than in the case of 77 Hz to 39 Hz indicating that higher frame rate indeed improves the lesion identification by capturing faster events.

5.4.2 Gas Body Identification

Because of the gas-body formation significantly enhances echogenicity in the lesion region and $\sigma_{FF,\max}$ performed well in the identification of lesion extent, we proposed the use of frame-to-frame echo decorrelation σ_{FF} as a means to identify newly formed and expanding gas-body activity. (The method will not capture pre-existing static gas bodies.) Based on the identified gas bodies, expansion rate information of the gaseous region was used to predict the occurrence of the macroscopic cavity.

The effects of various HIFU exposure parameters on the expansion rate of gaseous regions and the time to reach the threshold for macroscopic cavity formation were examined in this study. As described in the Sec. D, at higher PRF (130 Hz vs. 77 Hz) with other conditions equal, slower growth rate and smaller cavity size were observed. This is likely due to the shorter duration of each pulse with the increased duty cycle. With reduced energy input in tissue during each ultrasound pulse, higher PRF reduced the likelihood of gas-body initiation and heating, thereby lowering the expansion rate. Consistent with this observation, in the data sets with lower duty cycle (25%, all other conditions equal: 2600 W/cm^2, 77 Hz PRF, 1 s exposure), a lower value of the maximum ER of 0.93 ± 0.02 mm/s ($n = 2$) was observed, compared to 1.5 ± 0.3 mm/s ($n = 4$) in the cases with 50% duty cycle. There was also a longer delay (0.68 ± 0.25 s) in reaching the maximum ER compared to that in the cases with 50% duty cycle (0.36 ± 0.12 s). The lower duty cycle exposure also resulted in smaller cavity sizes (cavity area = 0.013 ± 0.0014 mm^2 at 25% duty cycle vs. cavity area = 0.187 ± 0.064 mm^2 at 50% duty cycle) in the gross images at the end of ablation. These observations indicate that pulsed HIFU exposure parameters may be optimized to control gas-body activity in HIFU ablation.

Although simulating the *in-vivo* condition was not the goal of our study, the concept of our technique should be applicable for *in-vivo* application and the technique can be translated after appropriate modification of the experimental setup to improve the speed of signal processing and instrument configuration. For example, integrating the imaging probe with the HIFU transducer collinearly would be a feasible approach. Second, gating strategies can be implemented to account for the cardiac tissue movements due to the beating heart and breathing. To implement the proposed method of lesion estimation for *in-vivo* applications, the threshold for IBS parameter needs to be predetermined since the effect of blood perfusion on lesion estimation using IBS was not studied in this paper. By taking a similar approach to construct "training data sets," non-invasive methods like MRI can be used to obtain lesion maps, which then can be used with IBS maps to construct ROC curves to determine the threshold. Although obtaining histology sections can provide the gold standard, it is invasive and may not be a viable way in general to obtain lesion map. Alternatively, in vitro results may be used as the first order of approximation, but experimental validation must be performed. Other challenges include the possibility that the threshold for lesion detection might be patient-dependent and tissue specific as different tissue types might have different tissue properties (ex: attenuation, thermal diffusivity) and will have different echogenic properties. Because the generation of macroscopic cavities in bulk tissue volumes may not be desired in achieving controlled HIFU ablation of cardiac tissue, identification of the precursors of such events along with the estimated extent of the lesion can be used as a feedback control to adjust HIFU exposure parameters during treatment.

In contrast to our M-mode study [42], which probed rapidly (1 kHz PRF) at a single line in space, the STBM method allows for a better study of the spatiotemporal development of lesion, gas body generation and its movement in 2D, albeit at a slower rate (77-130 Hz frame rate). Because acoustic radiation force from the HIFU transducer can cause a small amount of motion in the direction of the HIFU beam, interpretation of the acquired M-mode data can be complicated due to the spatial shifting of the tissue and lesion. With the larger STBM spatial window, this factor is much less important. In addition, the current study uses 2D spatial functions to compute the IBS and echo decorrelation parameters as opposed to 1D spatial functions in M-mode study, and that difference may have improved the lesion detection accuracy (area under curve of ROC: 0.96 vs. 0.91). Both the STBM and M-mode studies independently obtained same optimal IBS_{max} threshold (12 dB) for identifying the lesion extent even with differences in exposure conditions. However, the current study has been able to use the acquired 2D spatiotemporal information for prediction of macroscopic cavity formation and been able to investigate the effect of more HIFU ablation parameters (duty cycle, PRF, exposure duration) on ablation outcomes such as lesion width, time of occurrence of the gas bodies and their maximum expansion rate (ER), and the presence of macroscopic cavities and their size.

5.4.3 Limitations

In this study, lesion classification relied on matching the plane of B-mode imaging with the sectioning plane of the tissue lesion. Hence, small errors due to this mismatch in B-mode and gross tissue planes might occur in the estimation of lesion formation. Fixation and embedding of the tissue (which will be used in future study) could allow for more precise sectioning but this process also introduces potential spatial distortion due to the tissue preparation process. The threshold of IBS_{max} in estimating the lesion extent will probably be affected by flow perfusion and hence may be different for future study from the threshold obtained in preliminary results. This dependence on the perfusion can be accounted by determining its own threshold. The acoustic radiation force can cause some tissue motion at the focal spot of HIFU probe during the treatment process; however, this effect will be minimized by physically securing the tissue in place during ablation.

5.5 Conclusion

In this study, we compared the performance of several RF-based techniques using high-frequency, short-time B-mode imaging. We established a threshold to identify lesion area based on the time history of integrated backscatter and evaluated the performance of these methods using ROC curves. The temporal maximum of the integrated backscatter $IBS_{\max}$ at 12 dB threshold was determined to best map lesion induced by HIFU ablation with good accuracy. In addition, we demonstrated the use of frame-to-frame echo decorrelation to identify the rapidly-changing hyperechoic regions observed in the B-mode frames during ablation that are likely to be HIFU-induced gas-body activities. We evaluated the cavity expansion rate to develop a criterion for predicting the occurrence of a macroscopic cavity during ablation. The use of high imaging frame rate and high spatial resolution allowed for the detailed tracking of the time history of ablation in lesion detection and cavity formation.

5.6 References

[1] J. E. Kennedy, "High-intensity focused ultrasound in the treatment of solid tumours," *Nat. Rev. Cancer,* vol. 5, pp. 321-7, Apr 2005.

[2] M. A. Groh, O. A. Binns, H. G. Burton, 3rd, S. W. Ely, and A. M. Johnson, "Ultrasonic cardiac ablation for atrial fibrillation during concomitant cardiac surgery: long-term clinical outcomes," *Ann. Thoracic Surg.,* vol. 84, pp. 1978-83, Dec 2007.

[3] G. ter Haar, "Harnessing the interaction of ultrasound with tissue for therapeutic benefit: High-intensity focused ultrasound," *Ultrasound in Obstetrics and Gynecology,* vol. 32, pp. 601-4, Oct 2008.

[4] C. Damianou and K. Hynynen, "The effect of various physical parameters on the size and shape of necrosed tissue volume during ultrasound surgery," *J. Acoust. Soc. Am.*, vol. 95, pp. 1641-9, Mar 1994.

[5] S. J. Graham, L. Chen, M. Leitch, R. D. Peters, M. J. Bronskill, F. S. Foster, *et al.*, "Quantifying tissue damage due to focused ultrasound heating observed by MRI," *Magn. Reson. Med.*, vol. 41, pp. 321-328, Feb 1999.

[6] K. Hynynen, A. Darkazanli, E. Unger, and J. F. Schenck, "MRI-guided noninvasive ultrasound surgery," *Med. Phys.*, vol. 20, pp. 107-115, Jan-Feb 1993.

[7] A. B. Holbrook, J. M. Santos, E. Kaye, V. Rieke, and K. B. Pauly, "Real-Time MR Thermometry for Monitoring HIFU Ablations of the Liver," *Magnetic Resonance in Medicine*, vol. 63, pp. 365-373, Feb 2010.

[8] C. Mougenot, B. Quesson, B. D. de Senneville, P. L. de Oliveira, S. Sprinkhuizen, J. Palussiere, *et al.*, "Three-Dimensional Spatial and Temporal Temperature Control With MR Thermometry-Guided Focused Ultrasound (MRgHIFU)," *Magnetic Resonance in Medicine*, vol. 61, pp. 603-614, Mar 2009.

[9] R. Yang, K. K. Kopecky, F. J. Rescorla, C. A. Galliani, E. X. Wu, and J. L. Grosfeld, "Sonographic and computed tomography characteristics of liver ablation lesions induced by high-intensity focussed ultrasound," *Investigative Radiol.*, vol. 28, pp. 796-801, Sep 1993.

[10] C. Simon, P. Vanbaren, and E. S. Ebbini, "Two-dimensional temperature estimation using diagnostic ultrasound," *IEEE Trans. Ultrason. Ferroelectr. Freq. Control*, vol. 45, pp. 1088-99, 1998.

[11] A. N. Amini, E. S. Ebbini, and T. T. Georgiou, "Noninvasive estimation of tissue temperature via high-resolution spectral analysis techniques," *IEEE Trans. Biomed. Eng.*, vol. 52, pp. 221-8, Feb 2005.

[12] D. Liu and E. S. Ebbini, "Real-time 2-D temperature imaging using ultrasound," *IEEE Trans. Biomed. Eng.*, vol. 57, pp. 12-6, Jan 2010.

[13] R. M. Arthur, D. Basu, Y. Z. Guo, J. W. Trobaugh, and E. G. Moros, "3-D in vitro estimation of temperature using the change in backscattered ultrasonic energy," *IEEE Trans. Ultrason. Ferroelectr. Freq. Control*, vol. 57, pp. 1724-1733, Aug 2010.

[14] F. L. Lizzi, R. Muratore, C. X. Deng, J. A. Ketterling, S. K. Alam, S. Mikaelian, *et al.*, "Radiation-force technique to monitor lesions during ultrasonic therapy," *Ultrasound Med. Biol.,* vol. 29, pp. 1593-605, Nov 2003.

[15] R. Souchon, G. Bouchoux, E. Maciejko, C. Lafon, D. Cathignol, M. Bertrand, *et al.*, "Monitoring the formation of thermal lesions with heat-induced echo-strain imaging: A feasibility study," *Ultrasound Med. Biol.*, vol. 31, pp. 251-259, Feb 2005.

[16] C. Maleke and E. E. Konofagou, "Harmonic motion imaging for focused ultrasound (HMIFU): a fully integrated technique for sonication and monitoring of thermal ablation in tissues," *Phys. Med. Biol.*, vol. 53, pp. 1773-1793, Mar 2008.

[17] S. A. Eyerly, S. J. Hsu, S. H. Agashe, G. E. Trahey, Y. Li, and P. D. Wolf, "An in vitro assessment of acoustic radiation force impulse imaging for visualizing cardiac radiofrequency ablation lesions," *J. Cardiovasc. Electrophysiol.*, vol. 21, pp. 557-563, May 2010.

[18] M. Ribault, J. Y. Chapelon, D. Cathignol, and A. Gelet, "Differential attenuation imaging for the characterization of high intensity focused ultrasound lesions," *Ultrason. Imaging*, vol. 20, pp. 160-177, Jul 1998.

[19] H. Zhong, M. X. Wan, Y. F. Jiang, and S. P. Wang, "Monitoring imaging of lesions induced by high intensity focused ultrasound based on differential ultrasonic attenuation and integrated backscatter estimation," *Ultrasound Med. Biol.*, vol. 33, pp. 82-94, Jan 2007.

[20] S. Y. Zhang, M. X. Wan, H. Zhong, C. Xu, Z. H. Liao, H. Q. Liu*, et al.*, "Dynamic changes of integrated backscatter, attenuation coefficient and bubble activities during high-intensity focused ultrasound (HIFU) treatment," *Ultrasound Med. Biol.*, vol. 35, pp. 1828-1844, 2009.

[21] F. L. Lizzi, M. Astor, T. Liu, C. Deng, D. J. Coleman, and R. H. Silverman, "Ultrasonic spectrum analysis for tissue assays and therapy evaluation," *Int. J. Imag. Sys. Tech.,* vol. 8, pp. 3-10, 1997.

[22] T. D. Mast, D. P. Pucke, S. E. Subramanian, W. J. Bowus, S. M. Rudich, and J. F. Buell, "Ultrasound monitoring of in vitro radio frequency ablation by echo decorrelation imaging," *J. Ultrasound Med.,* vol. 27, pp. 1685-1697, Dec 2008.

[23] C. C. Coussios, C. H. Farny, G. Ter Haar, and R. A. Roy, "Role of acoustic cavitation in the delivery and monitoring of cancer treatment by high-intensity focused ultrasound (HIFU)," *Int. J. of Hyperthermia,* vol. 23, pp. 105-120, Mar 2007.

[24] F. L. Lizzi, "High-precision thermotherapy for small lesions," *Eur. Urol.,* vol. 23 Suppl 1, pp. 23-8, 1993.

[25] C. H. Farny, R. G. Holt, and R. A. Roy, "The correlation between bubble-enhanced HIFU heating and cavitation power," *IEEE Trans. Biomed. Eng.,* vol. 57, pp. 175-184, Jan 2010.

[26] B. A. Rabkin, V. Zderic, and S. Vaezy, "Hyperecho in ultrasound images of HIFU therapy: Involvement of cavitation," *Ultrasound Med. Biol.,* vol. 31, pp. 947-956, Jul 2005.

[27] T. D. Mast, V. A. Salgaonkar, C. Karunakaran, J. A. Besse, S. Datta, and C. K. Holland, "Acoustic emissions during 3.1 MHz ultrasound bulk ablation in vitro," *Ultrasound Med. Biol.,* vol. 34, pp. 1434-1448, Sep 2008.

[28] J. McLaughlan, I. Rivens, T. Leighton, and G. ter Haar, "A study of bubble activity generated in ex vivo tissue by high intensity focused ultrasound," *Ultrasound Med. Biol.,* vol. 36, pp. 1327-1344, Aug 2010.

[29] M. S. Canney, V. A. Khokhlova, O. V. Bessonova, M. R. Bailey, and L. A. Crum, "Shock-induced heating and millisecond boiling in gels and tissue due to high intensity focused ultrasound," *Ultrasound Med. Biol.,* vol. 36, pp. 250-267, Feb 2010.

[30] R. A. Roy, S. I. Madanshetty, and R. E. Apfel, "An acoustic backscattering technique for the detection of transient cavitation produced by microsecond pulses of ultrasound," *J. Acoust. Soc. Am.,* vol. 87, pp. 2451-2458, Jun 1990.

[31] D. Melodelima, J. Y. Chapelon, Y. Theillere, and D. Cathignol, "Combination of thermal and cavitation effects to generate deep lesions with an endocavitary applicator using a plane transducer: Ex vivo studies," *Ultrasound Med. Biol.*, vol. 30, pp. 103-111, Jan 2004.

[32] J. McLaughlan, I. Rivens, and G. ter Haar, "Cavitation detection in ex vivo bovine liver tissue exposed to high intensity focused ultrasound (HIFU)," presented at the 2007 IEEE Int. Symp. Biomed. Imaging: Macro to Nano Proc., Arlington, VA, USA, 2007.

[33] C. H. Farny, R. G. Holt, and R. A. Roy, "Temporal and spatial detection of HIFU-induced inertial and hot-vapor cavitation with a diagnostic ultrasound system," *Ultrasound Med. Biol.,* vol. 35, pp. 603-615, Apr 2009.

[34] V. A. Salgaonkar, S. Datta, C. K. Holland, and T. D. Mast, "Passive cavitation imaging with ultrasound arrays," *J. Acoust. Soc. Am.,* vol. 126, pp. 3071-3083, Dec 2009.

[35] M. Gyöngy and C. C. Coussios, "Passive cavitation mapping for localization and tracking of bubble dynamics," *J. Acoust. Soc. Am.*, vol. 128, pp. E175-E180, Oct 2010.

[36] T. Fawcett. ROC Graphs: Notes and practical considerations for researchers. *Machine Learning, 2004 - Citeseer*.

[37] M. S. R. Gudur, R. E. Kumon, Y. Zhou, and C. X. Deng, "High-Frequency Rapid B-Mode Ultrasound Imaging for Real-Time Monitoring of Lesion Formation and Gas Body Activity During High-Intensity Focused Ultrasound Ablation," *Ieee Transactions on Ultrasonics Ferroelectrics and Frequency Control,* vol. 59, pp. 1687-1699, Aug 2012.

[38] C. Kasai, K. Namekawa, A. Koyano, and R. Omoto, "Real-time two-dimensional blood-flow imaging using an auto-correlation technique," *IEEE Transactions on Sonics and Ultrasonics,* vol. 32, pp. 458-464, 1985.

[39] S. Siebers, M. Schwabe, U. Scheipers, C. Welp, J. Werner, and H. Ermert, "Evaluation of ultrasonic texture and spectral parameters for coagulated tissue characterization," in *2004 IEEE Int. Ultrason. Symp. Proc.*, 2004, pp. 1804-1807.

[40] R. H. Silverman, R. Muratore, J. A. Ketterling, J. Mamou, D. J. Coleman, and E. J. Feleppa, "Improved visualization of high-intensity focused ultrasound lesions," *Ultrasound Med. Biol.*, vol. 32, pp. 1743-1751, Nov 2006.

[41] T. D. Mast and S. Subramanian, "Analytic and numerical modeling of ultrasonic B-scan and echo decorrelation imaging," *Proc. Meetings Acoust.*, vol. 9, p. 020003, 2010.

[42] R. E. Kumon, M. S. R. Gudur, Y. Zhou, and C. X. Deng, "High-Frequency Ultrasound M-Mode Imaging for Identifying Lesion and Bubble Activity during High-Intensity Focused Ultrasound Ablation," *Ultrasound in Medicine and Biology*, vol. 38, pp. 626-641, Apr 2012.

CHAPTER 6

Conclusions and Future Work

In this thesis, high resolution ultrasound was used as an imaging modality for tissues and tissue engineered constructs to monitor the 2D/3D structural changes and to characterize the tissue changes either induced by HIFU ablation or by cell differentiation. A working application of spectral ultrasound imaging (SUSI) technique was developed and verified with polybead phantoms (Chapter 2). The technique is then used to assess the amount of mineral content in acellular constructs (Chapter 3). The development changes of MC3t3-cell constructs which include net cell proliferation/apoptosis, matrix and mineral production was studied in Chapter 4. High frequency and high frame rate B-mode imaging was used to assess the HIFU ablation process to characterize the lesion extent and the gas body activities in Chapter 5.

In general, this assessment technique will be helpful in non-destructive characterization and monitoring of the tissue samples in lab and for *in-vivo* applications in small animals. But due to the shallow imaging regions owing to higher attenuation at high imaging frequencies, this technique might be limited to fewer specific applications such as dermatology in humans. Some of the very specific research that can be investigated to realize the proposed SUSI technique in aforementioned applications are discussed below.

6.1 Spectral ultrasound Imaging

In the current approach, 1D fourier spectrum of the high frequency ultrasound signal from tissues and tissue engineered constructs were investigated to estimate the scatterer properties. Very close estimations were obtained for scatterer diameter of 6-25 µm including their concentration estimations.

Similar approaches as that of SUSI were employed to quantitatively characterize freshly dissected lymph nodes of cancer patients [1]. In their quantitative ultrasound method, backscattered signals were processed using 3D cylindrical regions of interest to yield parameter estimates associated with tissue microstructure. The estimated intercept and slope were used to differentiate a metastatic node from a non-metastatic lymph node by setting a size threshold using the Gaussian form factor. These results indicate that quantitative ultrasound methods were able to classify the nodes that either are completely metastatic or are completely free of metastatic tissue.

One of the advantage of the study in the current thesis over the above study is in its ability to resolve the smaller scatterer sizes (6-25 µm) as opposed to > 20 µm due to the high frequency ultrasound imaging employed in the current thesis (55 MHz as opposed to 25.6 MHz). With 55 MHz ultrasound imaging system can be used to employ similar technique on a 3D segment of the tissue by taking the 3D fourier transform on the backscattered 3D RF data, which might have even improved estimations.

6.2 Cell Cytoskeleton Study

The contribution of the cell organelles towards the spectrum of the ultrasound signal can be investigated for detailed understanding of SUSI. The contribution from actin filaments, microtubules and nuclei [2, 3] in the ultrasound spectrum and on the corresponding spectral parameters can be used to assess different cell types, their longitudinal growth and their differentiation processes. Each cell organelle investigation should be verified with biochemical assays to conclude the observations.

6.3 Differentiation Study

MC3t3 cell net proliferation/apoptosis and their differentiation processes in an *in-vitro* petri-dish were studied in the current thesis. Cell size, concentration and calcium mineral estimates were estimated with good accuracy using spectral ultrasound imaging. The effectiveness of the spectral ultrasound imaging in identifying the differentiation process can be investigated when the constructs are implanted in an *in-vivo* animal model. The non-destructive and non-invasive evaluation of the implanted scaffolds would benefit from the ability to monitor the cellular changes during the differentiation process at the implant site without the need for periodic animal sacrifice and explant analysis. This technique may allow the tissue engineers to sequentially evaluate the progress of tissue construct development process *in-vivo*.

6.4 HIFU Ablation Monitoring

RF data acquired from high-frequency, short-time B-mode imaging, a threshold to identify lesion area was established based on the time history of integrated backscatter. In addition, frame-to-frame echo decorrelation was proposed to identify the rapidly-changing hyperechoic regions observed in the B-mode frames during ablation that are likely to be HIFU-induced gas-body activities. Based on this approach, cavity expansion rate was evaluated to develop a criterion for predicting the occurrence of a macroscopic cavity at the end of ablation. This criterion could be useful in situations where monitoring is needed to prevent macroscopic cavity formation in the HIFU treatment process.

To adapt the method into practical application, it can be implemented in HIFU treatment of atrial fibrillation in *ex-vivo* rabbit heart for real-time monitoring and feedback control in order to achieve the desired ablation outcome as future study. For a given PRF of HIFU ablation, the RF data of each frame can be acquired during off period of HIFU and its processing to produce the parametric image representing the lesion extent, any occurrence of the gas bodies and their expansion rate can be done during the on period of HIFU. Based on the desired ablation outcome, if either the lesion extent estimated by IBS_{max} in this frame is the desired area or if the generated gas bodies are expanding at a rate which is capable of forming a macroscopic cavity then a feedback control will be activated to either end the ablation or to reduce the intensity of the HIFU exposure for desired ablation outcome.

The extent of the lesion created during the ablation can be monitored using IBS_{max} and can be verified with histological sections. The performance of IBS_{max} is expected to match with AUC, accuracy, sensitivity and specificity values in Table 6.1. Also, the evolution of the estimated lesion extent as it forms can be studied with online changes in electrophysiological properties of lesion and normal tissue obtained from fluorescence optical imaging camera. Any occurrence of the bubbles, as detected by frame-to-frame echo decorrelation can be expected to match with bubble detection using passive cavitation method and at the end of the ablation, no macroscopic cavities can be expected in the tissue when the feedback control is implemented to avoid the cavity formation based on expansion rate of the bubbles.

6.5 Acoustic Radiation Force Imaging

In its noninvasive applications, elastography has been typically used to determine local tissue strain through the use of externally applied mechanical compression [4, 5]. Focused ultrasound can be used to apply localized radiation force to small volumes of tissue for short durations (less than 1 ms) and the resulting tissue displacements can be mapped using ultrasonic correlation-based methods [6-8]. The tissue displacements are inversely proportional to the stiffness of the tissue and thus, a stiffer region of tissue exhibits smaller displacements than a more compliant region. Due to the short duration of the force application, this method provides information about the mechanical impulse response of the tissue, which reflects variations in tissue viscoelastic characteristics. With known strain maps of the tissue from the correlation-based methods and known input radiation force, elastic modulus of the specimen can be estimated, which needs to be validated with mechanical compressive testing.

Thus acoustic radiation force imaging can be used as a non-destructive and non-invasive tool to estimate the elastic properties of the tissues and tissue constructs in real-time. Due to its non-invasive nature, tissue scaffolds can be implanted in an *in-vivo* animal and their remodeling over time can be studied by studying the elastic properties of the implant site. Also, ARFI imaging has many potential clinical applications, including detecting and characterizing a wide variety of soft tissue lesions, and identifying and characterizing atherosclerosis, plaque and thromboses.

6.6 References

[1] J. Mamou, A. Coron, M. Hata, J. Machi, E. Yanagihara, P. Laugier, *et al.*, "Three-Dimensional High-Frequency Characterization of Cancerous Lymph Nodes," *Ultrasound in Medicine and Biology,* vol. 36, pp. 361-375, Mar 2010.

[2] M. C. Kolios, G. J. Czarnota, M. Lee, J. W. Hunt, and M. D. Sherar, "Ultrasonic spectral parameter characterization of apoptosis," *Ultrasound in Medicine and Biology,* vol. 28, pp. 589-597, May 2002.

[3] R. E. Baddour, M. D. Sherar, J. W. Hunt, G. J. Czarnota, and M. C. Kolios, "High-frequency ultrasound scattering from microspheres and single cells," *Journal of the Acoustical Society of America,* vol. 117, pp. 934-943, Feb 2005.

[4] I. Cespedes, J. Ophir, H. Ponnekanti, and N. Maklad, "Elastography - Elasticity Imaging Using Ultrasound with Application to Muscle and Breast in-Vivo," *Ultrasonic Imaging*, vol. 15, pp. 73-88, Apr 1993.

[5] T. A. Krouskop, T. M. Wheeler, F. Kallel, B. S. Garra, and T. Hall, "Elastic moduli of breast and prostate tissues under compression," *Ultrasonic Imaging*, vol. 20, pp. 260-274, Oct 1998.

[6] K. R. Nightingale, M. L. Palmeri, R. W. Nightingale, and G. E. Trahey, "On the feasibility of remote palpation using acoustic radiation force," *J Acoust Soc Am*, vol. 110, pp. 625-34, Jul 2001.

[7] K. Nightingale, M. S. Soo, R. Nightingale, and G. Trahey, "Acoustic radiation force impulse imaging: In vivo demonstration of clinical feasibility," *Ultrasound in Medicine and Biology*, vol. 28, pp. 227-235, Feb 2002.

[8] M. L. Palmeri, M. H. Wang, N. C. Rouze, M. F. Abdelmalek, C. D. Guy, B. Moser, *et al.*, "Noninvasive evaluation of hepatic fibrosis using acoustic radiation force-based shear stiffness in patients with nonalcoholic fatty liver disease," *Journal of Hepatology*, vol. 55, pp. 666-672, Sep 2011.